Studies on the Effects of Radicals on Growth and Passivation in Gallium Nitride

Shang Chen

Studies on the Effects of Radicals on Growth and Passivation in Gallium Nitride

Shang Chen

2012
Nagoya University
Graduate School of Engineering
Department of Electrical Engineering and Computer Science

Content

Chapter 1

Introduction

The idea of technology for semiconductors can be traced back to a paper by Gordon Moore in 1965, in which he stated that the number of components that could be incorporated per integrated circuit would increase exponentially over time [1]. From then on, the number of transistor per chip has almost doubled every 2 years, known as “Moore’s Law” shown in Fig.1.1.

Nowadays, this trend for increased performances will continue, while performances can always be traded against power depending on the individual application, sustained by the incorporation into devices of new materials, and the application of new transistor concepts. This direction for further progress is labeled “More Moore” [2].

The other trend is characterized by functional diversification of semiconductor-based devices. These non-digital functionalities do contribute to the miniaturization of electronic systems, although they do not necessarily scale at the same rate as the one that describes the development of digital functionality. Consequently, in view of added functionality, this trend may be designated “More-than-Moore” [2]. This combined need for digital and non-digital functionalities in a product is depicted in Fig.1.2.

Since the last five decades, silicon has been the mainstay of the electronics. With the “More Moore” and “More-than-Moore” trajectory pushing silicon to its

limits, industry has begun positioning several candidate materials for next generation semiconductors application.

As an example, here I list important key challenges for the realization of the "More-than-Moore" strategies [4]

- CMOS scaling based on non-Si materials (III/V, oxides, etc)
- Epitaxial growth of Germanium and compound semiconductors on Silicon
- Atomic Layer Deposition (ALD) of oxides and nitrides
- Piezoelectric films and nanostructures
- Characterization and metrology of very thin oxide layers

Obviously, the compound semiconductor and its related process are very important.

The compound semiconductor consisted by two or more elements have widely ranging physical properties. Since the physical properties such as band gaps, carrier mobility, optical properties, and thermal conductivity could be varied, they have therefore many possible applications to change our future life. As one of the most important compound semiconductor, the III–V nitrides are introduced and attracted many attentions in electronics applications since last decade.

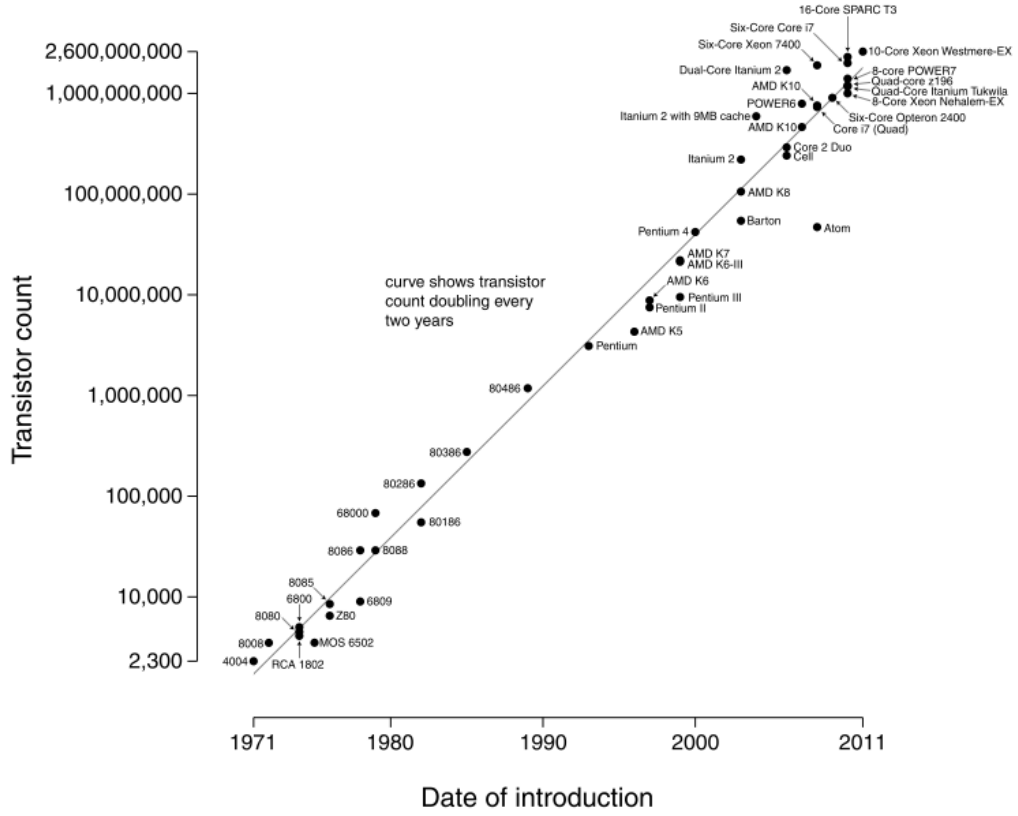

Figure 1.1 Microprocessor transistor counts from 1971 to 2011 and Moore's Law [3].

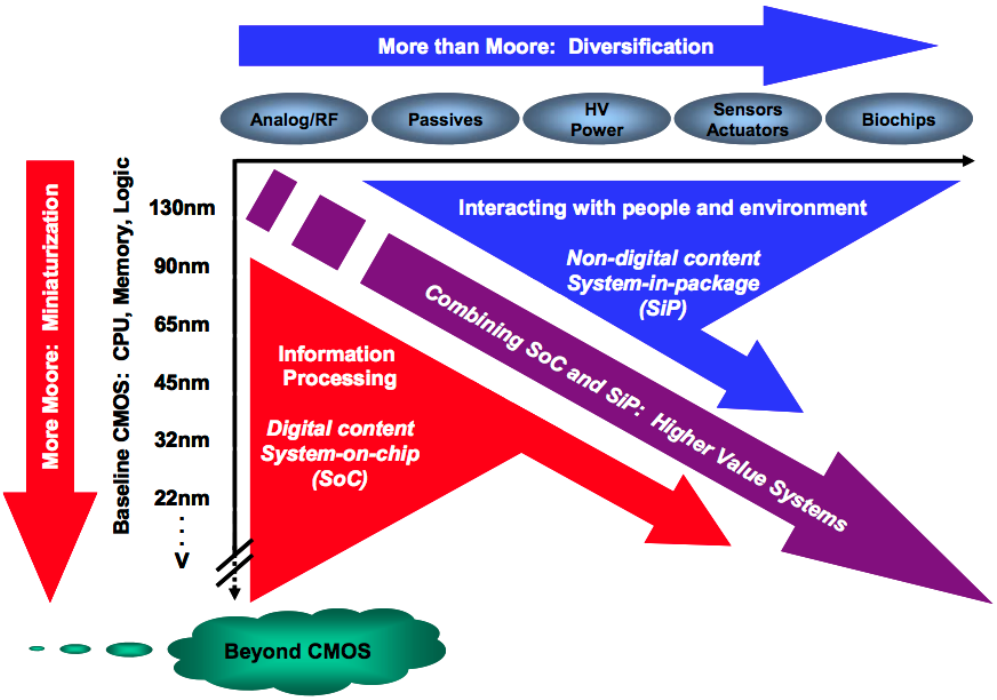

Figure 1.2 Miniaturization of the digital functions ("More Moore") and functional diversification ("More-than-Moore") [2].

1.1 Emerging development on III–V nitride materials

The III–V nitrides have emerged as the leading material for the production of blue light emitting diodes (LEDs), blue laser diodes and high-power, high-temperature electronics, and due to its several remarkable physical properties (wide energy band gap, high carrier mobility, and high thermal conductivity et.al.), that make them particularly attractive for reliable solid state device applications [4].

In particular, aluminum nitride (AlN), gallium nitride (GaN) and indium nitride (InN), are the basic materials for opto-electrical applications, because they form a continuous alloy system (InGaN, InAlN, and AlGaN) whose direct energy band gaps for the hexagonal wurtzite phase (α-) range from 0.8 eV for α-InN, 3.4 eV for α-GaN, and 6.2 eV for α-AlN as shown in Fig. 1.3 [5-9]. They have fairly high bond strengths and very high melting temperatures. The large bond strengths possibly inhibit dislocation motion and improve reliability in comparison to other III-V materials. In addition, the nitrides are resistant to chemical etching and allow GaN-based devices to be operated in harsh environments. These properties lead to devices with superior reliability [4].

Among the ternary compounds of III-nitride materials, recently, InGaN has drawn a great deal of attention. GaN and Ga-rich InGaN have been considered as the most important and indispensable materials used for the fabrication of light emitters which are active in entire visible and part of the near UV spectral regions. Especially, understanding the emission mechanism in InGaN multiple quantum well (MQW) structures is a key issue for further developing such optoelectronics devices [10-12].

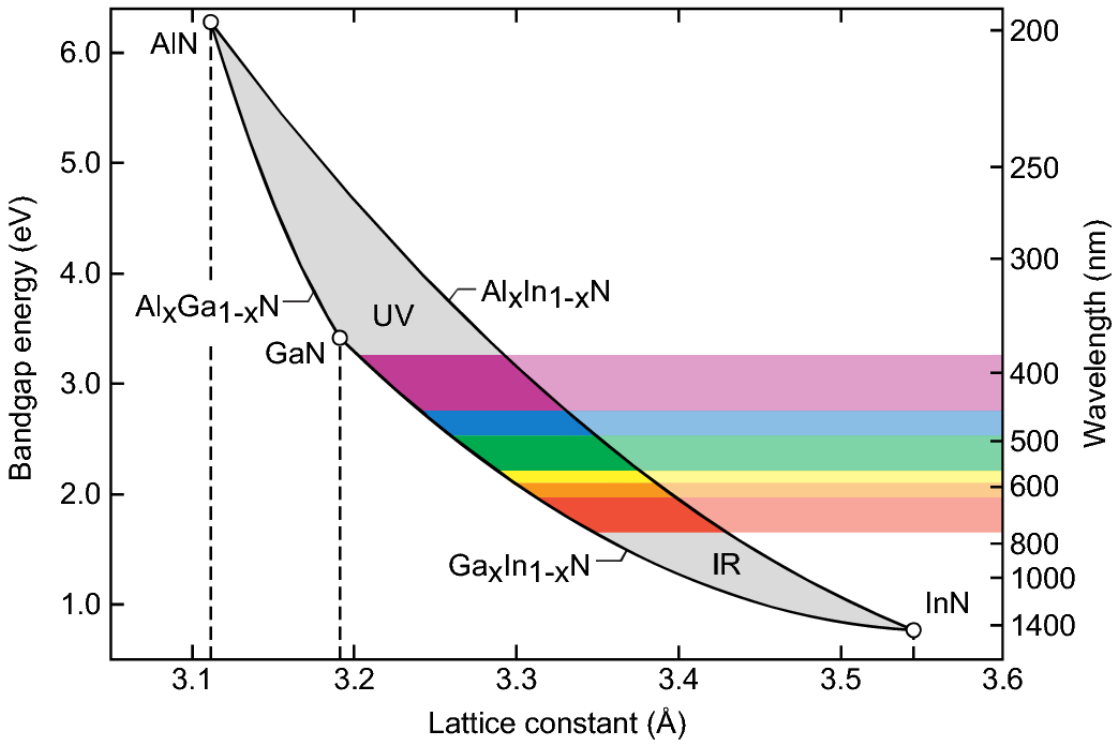

Figure 1.3 Experimental results of band gaps of hexagonal Group III-nitrides versus lattice constant c_0 at room temperature [13].

1.2 Advantages of gallium nitride (GaN)

As the most famous III–V nitride materials, GaN has attract much attention due to its contribution to applications of ultraviolet light emitting diodes (LEDs) [14, 15], high electron mobility transistor (HEMT) [16, 17], and high-k gate insulating films in FETs which require low gate leakage current and high switching speeds [18-21]. The physical properties of GaN (compare to other materials listed in Table 1.1), which include electrical breakdown characteristics ten times higher than that of Si, carrier mobility as good or better than that of Si, and an energy band gap three times or more that of Si. All those superior properties offer GaN devices for five key characteristics: high dielectric strength, high operating temperature, high current density, high-speed switching and low on-resistance (Fig 1.4) [22]. Notably, GaN offers useful characteristics, but it is not the only candidate to succeed Si devices in power supply, motor drive and other circuits. SiC devices offer an on-resistance on a par with that of GaN devices, and also can operate above 200^{o}C. The on-resistances of prototypes are about the same for both GaN and SiC devices (Fig. 1.5), but a comparison on theoretical transistor on-resistance shows that GaN is about a third that of SiC, it also has a higher switching speed [22].

Table 1.1 Comparison of physical properties of Si, GaAs, SiC and GaN materials. [22]

Comparison item	Si	GaAs	SiC (4H-SiC)	GaN
Bandgap	1.12eV	1.43eV	3.26eV	3.45eV
Dielectric breakdown strength	0.3MV/cm	0.4MV/cm	2.2MV/cm	4MV/cm
High frequency/high-output application index (Si indexed to 1)	1	7.1	180	760
Carrier mobility (with two-dimensional electron gas)	1,200cm²/V/s	6,500cm²/V/s	600cm²/V/s	900cm²/V/s (greater than 1500cm²/V/s)
Field saturation speed	1 x 10^7cm/s	1.3 x 10^7cm/s	2 x 10^7cm/s	2.7 x 10^7cm/s
Thermal conductivity	1.5W/cm/K	0.5W/cm/K	4.9W/cm/K	1.5W/cm/K

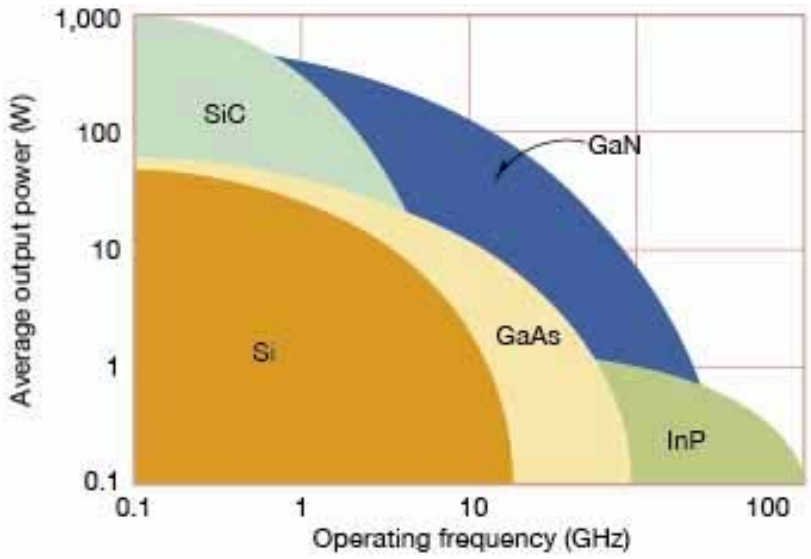

Figure 1.4 Comparison of semiconductor materials such as Si, GaAs, SiC, InP, and GaN that offer a high average output power to operating frequency [22].

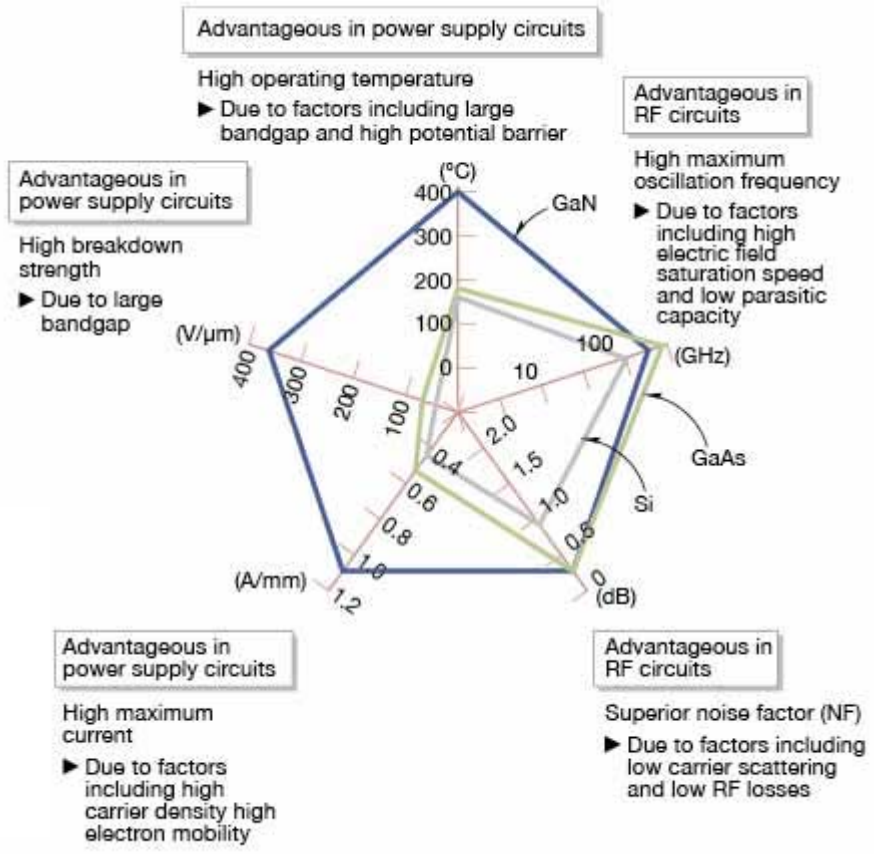

Figure1.5 GaN devices are superior to transistors using Si, GaAs or other materials in operating temperature, maximum current and breakdown strength, when it comes to operating temperature, maximum oscillation frequency, noise factor, maximum current and break down strength [22].

1.3 Key technical barriers in manufacturing of GaN based devices

Inexpensive wafer (like silicon), low mismatch substrate (sapphire was mainly used even the mismatch of crystal constant is as much as 17%), normally-off, and recently low damage process and high precious patterning process (i.e. plasma etching) have been proposed. However, there is still variety of technical barriers existing for manufacturing the GaN based devices. This section mainly focused on growth and process technologies for GaN.

1.3.1 Expensive GaN wafer

For the most of GaN applications, inexpensive GaN substrate was demanded. However, wafer with GaN film costs high because of the high consumption of resource (i.e. ammonia gas), small wafer size (4 inch), and low growth rate and so on.

Growth technologies of GaN films are metal organic chemical vapor deposition (MOCVD) [23], hydride vapor phase epitaxy (HVPE) [24], and molecular beam epitaxy (MBE) [25].

MOCVD is a main technology for mass fabrication of GaN films, because it can grow films with larger grain sizes, which is desirable and exploited by industry. It is a non-equilibrium growth technique that relies on vapor transport of the precursors and subsequent reactions of Group III alkyls and Group V hydrides (i.e. ammonia) in a heated zone. Designing of MOCVD reactor is very important to overcome problems presented by high growth temperatures, pre-reactions, and film non-uniformity. Typically in GaN growth, very high temperatures are required because of the high bond-strength of the N−H bond in ammonia precursors. Compounding this fact is the thermodynamic tendency of ammonia to pre-react with Group III metal organic

compounds to form non-volatile adducts. These factors contribute to the difficulties currently facing researchers in the design and scale-up of III-V nitride deposition systems [26].

HVPE is also a thermodynamic driven technology. Chemical reaction is between metallic sources of (Ga, Al, and In), HCl and ammonia at temperatures of 1000−1100°C, but at atmospheric pressure. It provides a simple and cost effective way to grow Group III nitrides. However, the high growth temperature limited densities of dopant to be incorporated into the devices, since high density of contamination would be induced to GaN films. That is main reason that researcher want to decrease the growth temperature.

MBE is a particular process, which supplying atomic source of nitrogen by radio frequency (rf) plasma. In these rf plasma MBE systems, the plasma source is used to dissociate the molecular nitrogen. The plasma is a complex mixture of atomic, molecular, and ionic N radicals. In typical MBE, the flux of the low energy reactive N species is very low that only low growth rates of 0.5μm/h can be achieved. At higher rf powers, higher growth rates can be achieved, but ion damage leading to deep levels and semi-insulating electrical properties occurs. A major advantage of MBE for nitride growth is the low growth temperature that can be achieved because of the atomic nitrogen source. This is in contrast to MOCVD and HVPE, which employ high growth temperatures (>1000°C) to crack the ammonia molecules. The lower growth temperatures should result in lower thermal stress upon cooling, less diffusion, and reduced alloy segregation. This lower growth temperature is especially important in AlGaN alloys that have a large mismatch in their thermal expansion coefficients [27]. Moreover, with the exception of the recent demonstration of a blue-violet emitting

GaN homojunction, there have not yet been comparable devices reported for MBE-grown nitrides [28-30].

Because the MBE could offer to decrease in growth temperature, it enabled to suppress volatilization of an element such as indium from the InGaN [31]. However, the InGaN growth with the MBE was suffered in high mosaicity and low growth rate (typical growth rate is around 0.5 μm/h). In the typical MBE system, metallic species such as gallium are supplied by thermal evaporation. Simultaneously atomic nitrogen species (so-called N radical) are supplied conventionally by plasma sources, which are utilized radio-frequency (rf) generated plasmas. Komaki *et al*. have been found that the molar fraction of InN was increased with increasing of flow rate of nitrogen. At low flow rate of nitrogen, the formation of phase separation due to dissociation of InN and condensation of indium on the growing surface were observed [32]. This was interpreted by correlation of the flux of N radical to substrate with the flow rate of nitrogen. Thus, they pointed out that the flux of N radical was pivotal in nitride growth [32]. Kushi *et al*. have reported results with high growth rates of 1.2 – 1.4 μm/h by improvement of production of N radical. They speculated that the large supply of N radical brought the high rates for growth of nitride [33]. Overall, the above results indicated that higher flux of N radical to substrate may improve both the mosaicity and the growth rate of nitride films.

1.3.2 Plasma etching induced damage

Plasma etching is an essential step for fabrication of GaN-based devices due to the high bond energy (8.92 eV/atom) of GaN. However, it is known that the process of plasma etching induced a large amount of defects [34, 35]. So far plasma etching induced damage (defects) is one of the most essential factors in degrading of device performance [36-38]. The defects induced by ion bombardment [39] or plasma emission [40] play a role as deep level recombination center. Therefore, a novel etching technology, which could avoid such kind of defect formation, is strongly demanded.

To achieve the ideal surface state, the complex interaction of surface-plasma and gaseous reaction in plasma should be concerning, which will be a task in a while. Hence, the damage free process should be achieved by low damage plasma etching and post-etching process, which aim to recover the damage induced by etching plasma.

So far, the post-etching processes to eliminate such defects were accomplished by some groups [41-43]. The stoichiometry is a crucial issue, which affects performance of devices that usually will be degraded in thermal annealing. Wet chemical treatment was not suitable for line fabrication. Hence, thermal annealing and wet chemical treatment do not meet the requirement of future scope. The new post-process to recover such kind of etching plasma induced defects at low temperature should be useful for industry.

1.4 Plasma technologies for GaN

Plasma has been the most widely used in the microelectronic industry for deposition and etching (Fig.1.5). The main properties of plasma process are given by

- Thermal non-equilibrium (room temperature available)
- High efficiency on production of active species at relatively low temperature
- High chemical reactivity

In some applications, such as plasma etching processes can achieve chemically selective reaction, anisotropic etch profile, high etch rate. Based on above advantages, plasma can widely contribute to manufacturing technologies of GaN. The examples of plasma affect in manufacturing of GaN based devices are given below.

In growth of GaN films, plasma can offers a low growth temperature compare to thermal process and low cost on resource due to its high production efficient for active species. As I introduced in last section, MBE was considered as the most convenient way to combined with plasma technology. Therefore, the MBE equipped with a nitrogen plasma source offers a platform to address low temperature and solutions for the issues. However, so far, MBE was suffered in low growth rate around 0.5 μm/h. The insufficient active nitrogen species generated conventionally with weakly ionized plasma was considered as the reason for limited growth rate of GaN in MBE. As one of the solutions to improve the low growth rate, high density of nitrogen radical was proposed.

In fabrication of electronic devices, etching of GaN over sapphire substrate is needed for defining contact regions in devices and also for providing device isolation in the fabrication of GaN based devices. High-quality GaN is chemically stable and

there has been no reliable wet etch process [44]. Therefore, plasma etching becomes the only viable approach for the pattern transfer in device fabrication process. A great deal of interest has been generated in low-damage etch processes based on high-density electron cyclotron resonance (ECR) plasmas and inductively coupled plasmas (ICP). Due to the magnetic confinement of electrons in the microwave source, high-density ECR plasmas are formed at low pressures with low plasma potentials and ion energies. Therefore, less damage than that produced by reactive ion etching (RIE) plasmas has been observed during ECR etching of III-V materials. ECR etching of GaN has been performed using Cl/H, and Cl/H/CH -based plasmas with etch rates ranging from a few hundred nm/min to several thousand nm/min [45-48]. High-density ICP plasmas are formed in a dielectric vessel encircled by an inductive coil into which rf power is applied. A strong magnetic field is induced in the center of the chamber which generates high density plasma due to the circular region of the electric field that exists concentric to the coil. For both ECR and ICP etch systems, anisotropic profiles can be obtained by superimposing an rf-bias on the sample to independently control ion energy.

In the post-etching process, the plasma offers low temperature process to avoid surface decomposition compare to thermal annealing and also should be promising tool for future of industry.

In general, plasma usually contains molecules, electrons, ions and radicals (atoms). Especially, the radical, which was considered as reactive species in growth of GaN by MBE, plasma etching, and recovery process for point defect, should be quantitatively analyzed by advance plasma diagnosis technology. This will help us to reveal the mechanism of plasma-surface interaction in growth and process of GaN.

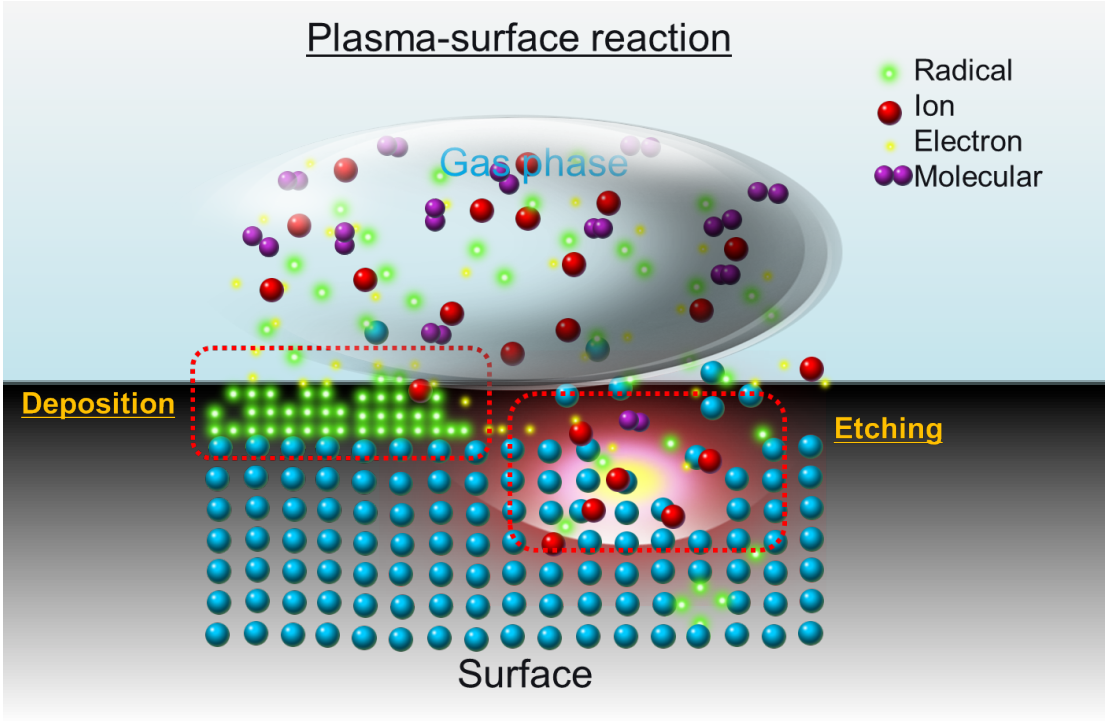

Figure 1.5 Schematic view of plasma-surface reaction, which result in a surface modification as the deposition and etching processes.

1.5 Scope of this thesis

This thesis describes a research towards understanding the effect of atomic radical on epitaxial growth of gallium nitride (GaN) and passivation of etching plasma damaged GaN.

In chapter 2, the principal of plasma diagnostics and film analysis will be presented. Vacuum ultraviolet absorption spectroscopy, optical emission spectroscopy, and quadruple mass spectrometer are used to diagnosis of plasma. The atomic force spectroscopy is carried out to check the surface morphology. X-ray diffraction (XRD) is used to investigate the composition and mosaicity of nitride films. The photoluminescence is applied to investigating the optical property of GaN films. X-ray photoelectron spectroscopy (XPS) is used to analyze the surface stoichiometric of GaN films.

In chapter 3, a novel high-density radical source (HDRS) for improving the growth rate and crystalline property of nitride films in molecular beam epitaxial (MBE) was developed by optimizing the antenna structure and applying external magnetic field. The absolute density of atomic nitrogen radicals and rotational temperature of nitrogen molecule were monitored using vacuum ultraviolet absorption spectroscopy (VUVAS) and optical emission spectroscopy (OES), respectively. By optimized source structure, at least 1 order higher density of nitrogen radical can be generated by HDRS compared with conventional source in MBE has been achieved. For an innovation of MBE growth of GaN, the measurements of absolute densities of N, H, and NH_3 at the remote region of the radical source excited by plasmas have become absolutely imperative. Moreover, we found that the N atom density was considerably affected by processing history, where the characteristic instability was observed during

the pure nitrogen plasma discharge sequentially after the hydrogen-containing plasma discharge. These results indicate the importance of establishing radical-based processes to control precisely the absolute densities of N, H, and NH_3 at the remote region of the radical source.

In chapter 4, using the new radical source that provide one order higher radical density than that of conventional source (CRS), it was examined that the growth rates were improved in the homoepitaxial growth of GaN with rates for 1.4μm/h, which is almost three times higher than that for the CRS. High growth rate of 1.4μm/h was also achieved for the heteroepilayer of InGaN grown using the HDRS. Notably, the crystalline property was greatly improved, which confirmed by X-ray rocking curve (XRC) profile for (0002) plane diffraction in the films with InN molar fraction of 3 to 18 %. The FWHM of XRC was decreased from 1400 to 600 arc sec at InN molar fraction around 17 %.

In chapter 5, as one possible solution, we propose the radical passivation, which is believed to realize a high reactive, damage free, and room temperature process. The effect of radical on passivation of damage induced by plasma etching in GaN has been investigated as well as surface stoichiometric and optical property. Higher radical density allowed us to achieve the rapid passivation of damaged semiconductor materials. We found that the PL intensities of the band-edge emission (I_{BE}), which had been drastically reduced by plasma- beam irradiation at a Cl ion dose of 5×10^{16} cm^{-2}, recovered to values close to those of as-grown samples after H exposure at a dose of 3.8×10^{17} cm^{-2}. XPS revealed the appearance of a peak at a binding energy of 18.3 eV, which is tentatively assigned to Ga−H, and confirmed the removal of Cl after H exposure. We also report that effect of the H exposure after

identical dosage with changing a ratio of fluxes for ions and atoms, where the band edge PL intensity (I_{BE}) showed a dependence on the flux-ratio. On the basis of a mechanism of passivation of the defects such as nitrogen vacancy (V_N) by the H to form electronic states related to Ga−H bonds, supported by *in-situ* X-ray photoelectron spectroscopic observation, during simultaneous irradiation of both hydrogen atoms and ions, irradiation of an energetically ionic species promotes desorption of the formed Ga−H bonds and then influences on efficiency in the recovery to gain optically- and stoichiometrically-improvements.

1.6 Reference

[1] G. E. Moore, “Cramming more Components onto Integrated Circuits”, *Electronics,* 38 (8) (April 19, 1965); reproduced in Proc. IEEE, **86** (1998) 82.

[2] W. Arden, M. Brillouët, P. Cogez, M. Graef, B. Huizing, and R. Mahnkopf, “More-than-Moore White Paper”.

[3] Wikipedia, http://en.wikipedia.org/wiki/Moore's_law.

[4] S. Keller, D. P. Steven: Current Opinion in Solid State and Materials Science, **3** Issue 1 (1998) 45.

[5] K. Osamura, S. Naka, and Y. Murakami: J. Appl. Phys. **46** (1975) 3432.

[6] D. Brunner, H. Angerer, E. Bustarret, R. Hopler, R. Dimitrov, O. Ambacher, and M. Stutzmann: J. Appl. Phys. **82** (1997) 5090.

[7] M. D. Bremse, W. G. Perry, T. Zheleva, N. V. Edwards, O. H. Nam, N. Parikh, D. E. Aspnes, and R. F. Davis: Mater. Res. Soc. Int. J. Nitr. Semi. Res. **1** (1996) 8.

[8] Y. J. Koide, H. Itoh, M. R. H. Khan, K. Hiramatu, N. Sawaki, and I. Akasaki: J. Appl. Phys. **61** (1987) 4540.

[9] T. Matsuoka, H. Okamoto, M. Nakao, H. Harima, and E. Kurimoto: Appl. Phys. Lett. **81** (2002) 1246.

[10] S. Nakamura, S. J. Pearton, and G. Fasol: The Blue Laser Diode (Springer, Berlin, 2000).

[11] S. Nakamura, M. Senoh, S. Nagahama, N. Iwasa, T. Yamada, T. Matsushita, H. Kiyoku, and Y. Sugimoto: Jpn. J. Appl. Phys. **35** (1996) L74.

[12]T. Mukai, H. Narimatsu, and S. Nakamura: Jpn. J. Appl. Phys. **37** (1998) L479.

[10] E. F. Schubert: *Light Emitting Diodes, second edition* (Cambridge University Press, Cambridge 2006).

[11] S. Nakamura, T. Mukai, M. Senoh: Appl.Phys.Lett. **64** (1994) 1687.

[12] B. Goldenberg, J. D. Zook, and R. J. Ulmer: Appl. Phys. Lett. **62** (1993) 381.

[13] Bernard Gil: *Group III Nitride Semiconductor Compounds. Physics and Applications*, (Oxford Science Publications, Clarendon, Oxford 1998).

[14] Y. F. Wu, P. B. Keller, D. Kapolnek, P. Komodo, S. P. Denbaars, and U. K. Mishra: Appl. Phys. Lett. **69** (1996) 1438.

[15] H.Morkoc: *Nitride Semiconductors and Devices, Springer Series in Material Science*, (Springer, Berlin, Heidelberg, 1999).

[16] S. Strite and H. Morkoc: J. Vac. Sci. Technol. B **10** (1992) 1237.

[17] H. Morkoc, S. Strite, G. B. Gao, M. E. Lin, B. Sverdlov, and M. Burns: J. Appl. Phys.**76** (1994) 1363.

[18] S. J. Pearton, C. B. Vartuli, J. C. Zolper, C. Yuan, and R. A. Stall: Appl. Phys. Lett. **67** (1995) 1435.

[19] S. Ookubo: Nikkei Electronics Asia, August 2006 issue.

[20] H. Amano, N. Sawaki, I. Akasaki, and Y. Toyoda: Appl. Phys. Lett. **48 (5)** (1986) 353–355.

[21] H. P. Maruska, and J. J. Tietjen: Appl. Phys. Lett. **15 (10)** (1969) 327–329.

[22] M. Mesrine, N. Grandjean, and J. Massies, Appl. Phys. Lett. **72** (1998) 350.

[23] Yoshikazu Yoshida: Rev.Sci.Instrum. **67** (3) March (1996).

[24] C. R. Abernathy, J. D. MacKenzie, and S. M. Donovan: Journal of Crystal Growth **178** (1997) 74.

[25] H. Cho, C. B. Vartuli, C. R. Abernathy, S. M. Donovan, S. J. Pearton, R. J. Shul, and J. Han, Solid State Electron. **42** (1998) 2455.

[26] H. S. Kim, G. Y. Yeom, J. W. Lee, and T. I. Kim: Thin Solid Films, **341** (1999) 180.

[27] W. V. Schoenfeld, C. H. Chen, P. M. Petroff, and E. L. Hu, Appl. Phys. Lett. **73** (1998) 2935.

[28] M. Hori, K. Kano, T. Yamaguchi, Y. Saito, T. Araki, Y. Nanishi, N. Teraguchi, and A. Suzuki: Phys. Stat. Solid. B **234** (2002) 750.

[29] H. Komaki, R. Katayama, K. Onabe, M. Ozeki, and T. Ikari: J. Cryst. Growth **305** (2007) 12.

[30] K. Kushi, H. Sasamoto, D. Sugihara, S. Nakamura, A. Kikuchi, and K. Kishino: Mater. Sci. Eng. B **59** (1999) 65.

[31] W. V. Schoenfeld, C. H. Chen, P. M. Petroff, and E. L. Hu: Appl. Phys. Lett. **73** (1998) 2935.

[32] P. Hacke, T. Detchprohm, K. Hiramatsu, and N. Sawaki: Appl. Phys. Lett. **63** (1993) 2676.

[33] J. D. Guo, M. S. Feng, R. J. Guo, F. M. Pan, and C. Y. Chang: Appl. Phys. Lett. **67** (1995) 2657.

[34] B. Rong, E. van der Drift, R. J. Reeves, W. G. Sloof, and R. Cheung: J. Vac. Sci. Technol. B **19** (2001) 2917.

[35] M. Minami, S. Tomiya, K. Ishikawa, R. Matsumoto, S. Chen, M. Fukasawa, F. Uesawa, M. Sekine, M. Hori, and T. Tatsumi: Jpn. J. Appl. Phys. **50** (2011) 08JE03.

[36] H. Cho, C. B. Vartuli, C. R. Abernathy, S. M. Donovan, S. J. Pearton, R. J. Shul, and J. Han: Solid State Electron. **42** (1998) 2455.

[37] H. S. Kim, G. Y. Yeom, J. W. Lee, and T. I. Kim: Thin Solid Films, **341** (1999) 180.

[38] X. A. Cao, H. Cho, S. J. Pearton, G. T. Dang, A. P. Zhang, F. Ren, R. J. Shul, L. Zhang, R. Hickman, and J. M. van Hove: Appl. Phys. Lett. **75** (1999) 232.

[39] J. M. Lee, K. M. Chang, S. W. Kim, C. Huh, I. H. Lee, and S. J. Park: J. Appl. Phys. **87** (2000) 7667.

[40] S. I. Na, G. Y. Ha, D. S. Han, S. S. Kim, J. Y. Kim, J. H. Lim, D. J. Kim, K. I. Min, and S. J. Park: IEEE Photo. Tech. Lett. **18** (2006) 1512.

[41] C. B. Vartuli, S. J. Pearton, C. R. Abernathy, and J. D. Mackenzie: Solid State Electron. **41** (1997) 1947.

[42] R. J. Shul, S. P. Kilcoyne, M. Hagerott Crawford, J. E. Parmeter, C. B. Vartuli, C. R. Abernathy, and S. J. Pearton, Appl. Phys. Lett. **66** (1995) 1761.

[43] R. J. Shul, A. J. Howard, S. J. Pearton, C. R. Abernathy, C. B. Vartuli, P. A. Barnes, and M. J. Bozack, J. Vac. Sci. Technol. B. **13** (1995) 2016.

[44] S. J. Pearton, C. R. Abernathy, F. Ren, J. R. Lothian, P. W. Wisk, A. Katz, and C. Constantine, Semicond. Sci. Technol. **8** (1993) 310.

[45] S. J. Pearton, C. R. Abernathy, and F. Ren, Appl. Phys. Lett. **64** (1994) 2294.

Chapter 2

Plasma Diagnostics and Film Analysis

2.1 Overview

The principal of plasma diagnostics and film analysis is presented. In chapter 3, for development of high-density radical source, we measure the absolute density of nitrogen radical using vacuum ultra-violet absorption spectroscopy (VUVAS). The optical emission spectroscopy (OES) is carried out to monitor the discharge mode and estimate the rotational temperature of nitrogen molecular. For the molecular species, we use the quadruple mass spectrometer (QMS) to determine the density. In chapter 4, the high density radical source is equipped on MBE to verify the effect of high density radical to crystal growth. The atomic force spectroscopy (AFM) was carried out to examine the surface state. To further compare the crystal quality of GaN films grown by HDRS and conventional source, the X-ray reflection XRD is carried out. In chapter 5, radical passivation of plasma damage GaN, the photoluminescence (PL) is carried out to investigate the optical property of GaN films. X-Ray Photoelectron Spectroscopy (XPS) is used to analyze the surface stoichiometric of GaN films.

2.2 Vacuum Ultraviolet Absorption Spectroscopy (VUVAS)

This technology is a convenient way to measure the absolute density of atom based on principle of absorption spectroscopy.

2.2.1 Theory of Absorption Spectroscopy

If the parallel light from a source passes through as absorption cell, such as plasma, the intensity of the transmitted light is given as follows [1],

$$I(\nu) = I_0(\nu)\exp[-k(\nu)L], \qquad (2.1)$$

where ν is the frequency, I(ν) and I_0(ν) are the intensities of the transmitting light and the incident light, respectively. L is the absorption path length, and k(ν) is the absorption coefficient as a function of frequency ν.

The broadening of the absorption coefficient, that is, the broadening of the absorption line-profile is due to the causes as follows,

(1) Natural broadening due to the finite lifetime of the exited state.

(2) Doppler effect broadening due to the motions of the atoms.

(3) Lorentz broadening due to collisions with foreign gases.

(4) Holtsmark broadening due to collisions with other absorption atoms of the same kind.

(5) Stark effect broadening due to collisions with electrons and ions.

However, in this study the Doppler broadening and Lorentz broadening should be taken into account, because the density of the electron and absorbing atoms should be low.

Here, we consider that a parallel beam of the light of frequency ν passed through a layer of atoms bounded by the planes at the length of dL. Suppose there are N_l normal atoms per cm^3 of which dN_l are capable of absorbing the frequency range between ν and $\nu+d\nu$, and N_u excited atoms of which dN_u are capable of emitting this frequency range. Neglecting the effect of spontaneous re-emission in view of the fact that it takes place in all direction, the decrease in energy of the beam is given by

$$-[I(\nu)]d\nu = dN_l dL\rho(\nu)B_{lu}h\nu - dN_u dL\rho(\nu)B_{ul}h\nu, \qquad (2.2)$$

where B_{lu} and B_{ul} are Einstein B coefficient from ground state l to excited state u and from l to u, respectively. h is Planck's constant, and $\rho(\nu)$ is the radiation energy density given by $I(\nu)=c\rho(\nu)$, (c: light velocity). Rewriting Eq. (2-2), we obtain

$$-\frac{1}{I(\nu)}\frac{d[I(\nu)]}{dL}d\nu = \frac{h\nu}{c}(B_{lu}dN_l - B_{ul}dN_u), \qquad (2.3)$$

Recognizing that the left-hand term is $k(\nu)d\nu$ as defined by Eq. (2-1), Eq. (2-3) becomes

$$k(\nu)d\nu = \frac{h\nu}{c}(B_{lu}dN_l - B_{ul}dN_u) \qquad (2.4)$$

And integrating over the whole absorption line, neglecting the slight variation in ν throughout the line,

$$\int k(\nu)d\nu = \frac{h\nu_0}{c}(B_{lu}N_l - B_{ul}N_u), \qquad (2.5)$$

where ν_0 is the frequency at the center of the line. Here we use the Einstein A coefficient.

$$\int k(\nu)d\nu = \frac{c^2}{8\pi\nu_0^2}\frac{g_u}{g_l}AN_l(1-\frac{g_lN_u}{g_uN_l})$$

$$\cong \frac{c^2}{8\pi\nu_0^2}\frac{g_u}{g_l}AN_l \qquad (N_u << N_l), \quad (2.6)$$

where g_l and g_u are the statically weights of the lower and upper level, respectively. Therefore, by measuring $I_0(\nu)$ and $I(\nu)$, $k(\nu)$ is decided and we can estimate the density N_l.

When the light source is incoherent light such as lamp, the intensity of measured light is the integrated value over the frequency

$$I_0 = \int e_0 f_0(\nu)d\nu,$$

$$I_a = \int e_0 f_0(\nu)\{1-\exp[-k_0 f_a(\nu)L]\}d\nu, \quad (2.7)$$

where I_0 and I_a are the intensities of the incident light and the absorption, respectively, $f_0(\nu)$ is the emission line-profile function for the light source, e_0 is the emission intensity of the light source at a center frequency of $f_0(\nu)$, $f_a(\nu)$ is the absorption line-profile function, and k_0 is the absorption coefficient at the center frequency of $f_a(\nu)$. The absorption intensity $A(k_0L)$ is given by the following formula.

$$A(k_0L) = 1-\frac{I_a}{I_0} = \frac{\int f_0(\nu)\{1-\exp[-k_0 f_a(\nu)L]\}d\nu}{\int f_0(\nu)d\nu}. \quad (2.8)$$

From $A(k_0L)$ obtained by measurement, k_0 is determined by assuming the line-profile function $f_0(\nu)$ and $f_a(\nu)$. Then, the number density of state l, N_l, is estimated by using Eq. (2.2-2.6) as

$$N_l = \frac{8\pi\nu_0^2}{c^2}\frac{g_l}{g_u}\frac{1}{A}k_0\int f_a(\nu)d\nu. \quad (2.9)$$

2.2.2 Measurements of Absolute Densities of Atomic H and N Radicals with Micro-Discharge Hollow Cathode Lamp (MHCL)

Our group has developed the measurement system of absolute densities of atomic H [2], N [3] and O [4] radicals in the ground state using the VUVAS with micro-discharge hollow cathode lamp (MHCL) as a light source. The typical system of VUVAS with MHCL is show in Fig.2.1. Transition lines used for measuring the absolute densities of H, N and O radicals are Lyman α at 121.6 nm, $^4P_{5/2}$-$^4S^0_{3/2}$, $^4P_{3/2}$-$^4S^0_{3/2}$ and $^4P_{1/2}$-$^4S^0_{3/2}$ at 120.0 nm and $^3S^0$-$2p^4$ $^3P_2$ at 130.217 nm, 3s $^3S^0$-$2p^4$ $^3P_1$ 130.487 nm and 3s $^3S^0$-$2p^4$ $^3P_0$ 130.604 nm, respectively. Each emission of these transition lines can be obtained by the H_2, N_2 and O_2 plasma, respectively. However, these emissions are caused by two major processes [5-7]. One is the direct excitation of ground state atomic radicals by the electron impact.

$$X + e \rightarrow X^* + e \rightarrow X + h\nu + e\,, \qquad (2.10)$$

where X is the atomic radical of interest, X^* is X atoms in the excited state. The other is the dissociative excitation of ground state of X_2 by the electron impact.

$$X_2 + e \rightarrow X^* + X + e \rightarrow X + X + h\nu + e \qquad (2.11)$$

Reaction (2.10) is responsible for the production of slow excited X^* atoms. Reaction (2.11) can produce fast excited X atoms which produce a large Doppler broadening. Therefore, the structure of the atomic radical emission line profile consists of a two-component velocity distribution arising from two different excitation processes as shown in Eqs. (2.10), and (2.11). It is difficult to estimate the emission line profile, which involves a two-component velocity distribution. In the view of problem above in the measurement of absolute atomic radical density, we have developed a high

pressure MHCL as a light source for VUVAS. The specific merits of the MHCL we expect are as follows,

(1) The emission line profile is not involve a large Doppler shift due to the fast excited atomic radical arising from dissociative excitation of molecules, since they should be thermalized before they emit light.

(2) The size of the hollow cathode is a small as 0.1 mm diameter, resulting in a high current density in the cathode, which is favorable for attaining a high dissociation degree of molecules and obtaining spectrally pure atomic radical emission.

(3) A point-source-like emission from a micro-hollow can be efficiently coupled to the entrance slit of a monochromator using an appropriate lens system.

(4) The lamp is compact and is operated with an inexpensive dc power source.

The cathode and anode consist of a plate with 0.5 mm thickness with a through-hole hollow of 0.1 mm in diameter. Helium (250 sccm) and helium gas containing a small amount of H_2, N_2 or O_2 gas (5 sccm) were used. The MHCL was operated at a total pressure of 0.1 MPa.

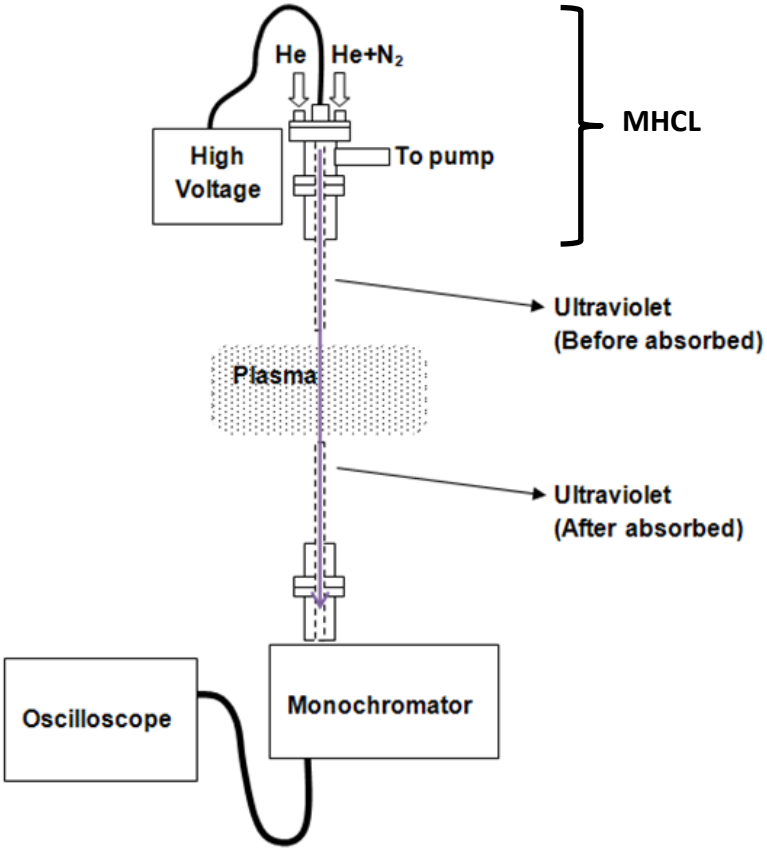

Figure 2.1 A typical setup of VUVAS system.

2.3 Optical Emission Spectroscopy (OES)

2.3.1 Principle of optical emission spectroscopy

Many optical emissions originating from excited species (e.g. atomic and molecular radicals) are generally observed in the plasma. Specific species is identified by the photon energy of the optical emission. Excited species are generated by various processes such as electron collision, dissociation, impact of other excited species, photon absorption, etc. Generally, excitation by electron impact frequently occurs in the plasma. Electron impact excitation of the ground state is given by

$$e + X \rightarrow X^* + e \,, \qquad (2.12)$$

where X is the species of interest. De-excitation is followed by the emission of a photon from the excited state as,

$$X^* \rightarrow X + h\nu \,. \qquad (2.13)$$

The intensity of the optical emission due to the transition from an excited state to the ground state is given by

$$I_x \propto n_e n_X \int \sigma_X(\varepsilon) v(\varepsilon) f_e(\varepsilon) d\varepsilon = k_{eX} n_e n_X \,, \,, \qquad (2.14)$$

where n_e is the electron density, n_X is the density of X, $\sigma X(\varepsilon)$ is the collision cross section for the electron impact excitation of X as a function of electron energy, $v(\varepsilon)$ is the electron velocity and $f_e(\varepsilon)$ is the electron energy distribution function (EEDF). k_{eX} (ε) is the excitation rate coefficient for X^* by the electron impact on X. Under the condition where k_{eX} and n_e are kept constant, the emission intensity is proportional to the density of species. However, both of them are affected by the experimental conditions and are generally so difficult to be kept constant when external parameters, such as input power, working pressure, are varied in the plasma processing. Thereby,

optical emission spectroscopy (OES) technique is widely used as a monitoring tool in various plasma processes. Moreover, in order to compare those emission intensities with the density of species, it is necessary to assume that emissions from exited states chosen are proportional to the density of the same species in the ground state. Therefore, the special technique such as actinometric optical emission spectroscopy (AOES) is frequently applied to estimate relative density of species in the ground state [8-14].

Optical emission spectra are generally measured by using a spectrometer. Usually, a monochromator with a photomultiplier tube (PMT) and multi-channel spectrometer with a charged coupled device (CCD) array are used. In a monochromator the light intensity is detected through the exit slit by PMT, as shown in Fig. 2.2 (a). On the other hand, in a multi-channel spectrometer the light intensity is detected by each pixel of CCD, as shown in Fig. 2.2 (b). The advantage of the multi-channel spectrometer is that it can measure a wide range (several ten nm) of wavelength simultaneously; however, the defect of the multi-channel spectrometer is that the resolution is restricted by the size of the pixel of CCD. The resolution of spectrometer sometimes limits the accuracy of measurements.

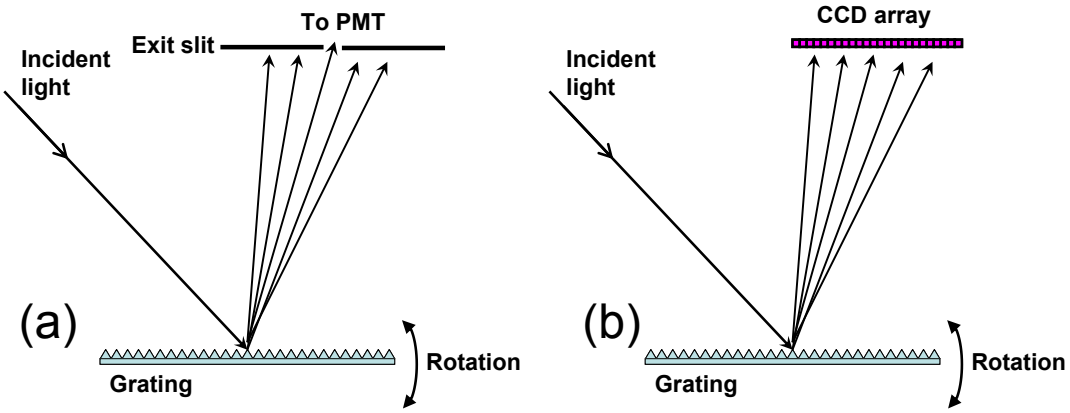

Figure 2.2 The schematic illustration of (a) monochromator and (b) multi-channel spectrometer.

A spectral line measured by a spectrometer has a certain width. The full width at half maximum (FWHM) of the spectral line is determined by various factors such as natural broadening, Doppler broadening, pressure broadening, Stark broadening, and instrumental broadening (instrumental function). The natural broadening giving a Lorentzian line shape, however, is generally very small and negligible. Doppler broadening depends on the temperature of the species of interest. Doppler broadening gives a Gaussian line shape as,

$$f_D(\nu) = \exp\left[-\left\{2\sqrt{\ln 2}\,\frac{(\nu-\nu_0)}{\Delta\nu_D}\right\}^2\right], \qquad (2.15)$$

with

$$\Delta\nu_D = \frac{2\nu_0}{c}\sqrt{\frac{2RT\ln 2}{M}}, \qquad (2.16)$$

Where $\Delta\nu_D$ is the FWHM of the Doppler broadening, ν_0 is the center frequency, c is the velocity of light, R is the gas constant, T is the gas temperature, and M is the mass number. Pressure broadening depends on pressure around the species of the interest gives a Lorentzian function as,

$$f_P(\nu) = \frac{\Delta\nu_P}{2\left\{4(\nu-\nu_0)^2 + \left(\frac{\Delta\nu_P}{2}\right)^2\right\}}, \qquad (2.17)$$

with

$$\Delta\nu_P = \frac{1}{\pi}z = \frac{1}{\pi}\cdot n\cdot\sigma\cdot\sqrt{\frac{8RT}{\pi\mu}}, \qquad (2.18)$$

where ν_P is the FWHM of the pressure broadening, z is the collision frequency, n is the density of the species, σ is the collision cross section, μ is the reduced mass. Stark broadening depends on the electric field caused by charged particles such as electrons

and ions. Therefore, the electron density can be derived from the Stark width. The instrumental broadening depends on the performance of the spectrometer used in the experiment. In order to determine the instrumental function, a light source such as a low-pressure mercury lamp is generally used, which gives enough sharp spectral lines compared to the instrumental function. The actual spectrum is determined from the convolution of the various broadening mechanisms. The convolution of Gaussian and Lorentzian functions results in a Voigt profile. The voigt function is given by

$$f_V(v) = \frac{a}{\pi}\int \frac{\exp(-y^2)}{a^2 + (\omega + y)^2} dy \,, \qquad (2.19)$$

with

$$a = \frac{\Delta\nu_L}{\Delta\nu_G}\sqrt{\ln 2} \,, \qquad (2.20)$$

and

$$\omega = \frac{2(\nu - \nu_0)\sqrt{\ln 2}}{\Delta\nu_G} \,, \qquad (2.21)$$

where $\Delta\nu_L$ is the FWHM of the Lorentz broadening, $\Delta\nu_G$ is the FWHM of the Gaussian broadening.

2.3.2 Measurement of rotational temperature of N_2 molecule

The rotational temperature of N_2 molecule can be determined by analyzing optical emission spectra of $C^2\prod_u$ - $B^3\prod_g$ electronic transitions of N_2 molecule. The electronic transitions take place from the rotational levels of various vibrational levels of one electronic state to the rotational and vibrational levels of another electronic state. One of the emission spectra of N_2 molecule is called “second positive system”, which is due to the electronic transition from $C^3\prod_u$ state to $B^3\prod_g$ state having many rotational

and vibrational levels. The emission spectrum of one vibrational band depends on the rotational temperature because the rotational levels at both $C^3\prod_u$ state to $B^3\prod_g$ state are expected to be represented in Boltzmann distributions. Therefore, the rotational temperatures of N_2 molecule can be determined by comparing results between an experimental and theoretical spectrum.

In this study, the emission spectra of the N_2 (0-2) band in about 380.4 nm were measured. Here, the 0-2 band means the vibrational band of an electronic transition where the vibrational quantum number of the upper state ($C^3\prod_u$ state) is 0, and that of the lower state ($B^3\prod_g$ state) is 2.

Because the line strength and energy levels of the electronic transition depend on molecular structures, calculations are necessary to determine the theoretical spectrum. The procedure of the calculation is as follows:

- Calculation of the energy levels for the $C^3\prod_u$ state and the $B^3\prod_g$ state.
- Calculation of the wavelengths of the transition for each branch following the selection rules.
- Calculation of the line strength using the Hönl-London factor for each transition wavelength.
- Calculation of the line shape and Boltzmann distributions as functions of line widths and the rotational temperatures.

Fitting of calculated spectra to measured spectra by least-squares approximation using parameters of the line width and the rotational temperature.

The rotational temperature tends to equilibrate with a kinetic temperature because of collisions between neutral and excited molecules. The rotational temperature of N_2 molecule can be used to determine the gas temperature.

The energy of molecule can be represented as the sum of three parts, that is, the electronic energy T_e, the vibrational energy G_v, and the rotational energy F as,

$$E = T_e + G_v + F\,. \qquad (2.22)$$

T_e and G_v of N_2 molecule in the $C^3\prod_u$ state and $B^3\prod_g$ state are given in Herzberg [15,16]. The vibrational term values of anharmonic oscillator are given by,

$$G_v = \omega_e\left(v+\frac{1}{2}\right) - \omega_e x_e\left(v+\frac{1}{2}\right)^2 + \omega_e y_e\left(v+\frac{1}{2}\right)^3 + \cdots, \qquad (2.23)$$

where the vibration quantum number v can take the values 0, 1, 2, …. The first term is the term of a harmonic oscillator. The rotational term values are given as functions of the rotational quantum number J and the rotational constant. The rotational energy levels of the $C^3\prod_u$ and $B^3\prod_g$ states are triplet states of spins, and then the rotational term values are given for the multiple rotational components. The rotational term values are given by [17],

$$F_0(J) = B_v\left[J(J+1) - Z_1^{1/2} - 2Z_2\right] - D_v\left(J-\frac{1}{2}\right)^4, \qquad (2.24\text{ a})$$

$$F_1(J) = B_v\left[J(J+1) + 4Z_2\right] - D_v\left(J+\frac{1}{2}\right)^4, \qquad (2.24\text{ b})$$

$$F_2(J) = B_v\left[J(J+1) + Z_1^{1/2} - 2Z_2\right] - D_v\left(J+\frac{3}{2}\right)^4, \qquad (2.24\text{ c})$$

with

$$Z_1 = Y(Y-4) + \frac{4}{3} + 4J(J+1), \qquad (2.25\text{ a})$$

$$Z_2 = \frac{1}{3Z_1}\left[Y(Y-1) - \frac{4}{9} - 2J(J+1)\right], \qquad (2.25\text{ b})$$

where B_v and D_v are rotational constants, and Y is a spin-axis coupling constant, which is a degree of coupling of the spin to the direction of the internuclear axis. The rotational constant was reported by Hartmann *et al*. [18].

The transition energy of the rotation-vibration lines between the upper state and the lower state can be calculated by,

$$E = \left(T_e^{'} - T_e^{''}\right) + \left(G_v^{'} - G_v^{''}\right) + \left(F^{'} - F^{''}\right). \quad (2.26)$$

Here, wave numbers of rotational transitions are obtained for a band v'-v'' according to the selection rules as.

R branches $\quad v_{\Omega;J}^{R} = F_{\Omega;J+1}^{'} - F_{\Omega;J}^{''} \quad (\Omega = 0,1,2), \quad (2.27\ a)$

Q branches $\quad v_{\Omega;J}^{Q} = F_{\Omega;J}^{'} - F_{\Omega;J}^{''} \quad (\Omega = 1,2), \quad (2.27\ b)$

P branches $\quad v_{\Omega;J}^{P} = F_{\Omega;J-1}^{'} - F_{\Omega;J}^{''} \quad (\Omega = 0,1,2). \quad (2.27\ c)$

On emissions, the rotational intensity distribution follows line strengths, which depend on the branches and rotational quantum numbers. The precise formula for the line strength was first given on the basis of the old quantum theory by Hönl and London [19], and then called "Hönl-London factors". The various formula of the Hönl-London factors are given at the different angular moment in the molecule, which consist of electron spin, electronic orbital angular momentum, and angular momentum of nuclear rotation. For the N_2 second positive system ($C^3{}_u$ - $B^3{}_g$), the intensity distributions follow Hund's case (a), in which the interaction of the nuclear rotation with the electronic motion (spin as well as orbital) is very weak, whereas the electronic motion itself is coupled very strongly to the line joining the nuclei [20]. The splitting between the multiplet rotational energy terms of $C^3\prod_u$ - $B^3\prod_g$ transitions is about 39 cm^{-1}, where the value is represented by the spin-orbit coupling constant A ($Y=A/B_v$).

The value of A is much larger than the splitting between the rotational lines. The Hönl-London factors of Hund's case (a) are that of a symmetric top with as an angular momentum K about an axis [21]. The line strengths S using the Hönl-London factors including static weights in the upper state are given by,

$$S_{\Omega}^{R}(J)=\frac{(J+\Omega)(J-\Omega)}{J}, \qquad \text{for} \quad \text{J=+1 (R branches),} \qquad (2.28\ a)$$

$$S_{\Omega}^{Q}(J)=\frac{(2J+1)\Omega^{2}}{J(J+1)}, \qquad \text{for} \quad \text{J=0 (Q branches),} \qquad (2.28\ b)$$

$$S_{\Omega}^{P}(J)=\frac{(J+1+\Omega)(J+1-\Omega)}{J+1}, \qquad \text{for} \quad \text{J=−1 (P branches).} \qquad (2.28\ c)$$

The line strengths S give the rotational population for a vibrational level of the upper state. The intensities of the rotational levels are given by thermal distributions of as follows [22].

$$I_{em}=\frac{C_{em.}}{Q_r}S_J\exp\left(-\frac{F'hc}{k_BT_r}\right), \qquad (2.29)$$

where $C_{em.}$ is a constant depending on the change of the dipole moment and the number of molecules in the upper level, F' is the rotational term value of the upper state in Eq. (2.16 a, b and c), h is the Planck constant, T_r is the rotational temperature, and Q_r is the rotational partition function. The rotational distribution for each vibrational transition with a rotational temperature is determined using Eq. (2.16) to Eq. (2.21).

The emission distribution due to the rotational structures is affected by the rotational temperature and the width of each rotational line. The finite line shape may be approximated as [22],

$$g(\Delta\lambda)=\frac{a-(2\Delta\lambda/W)^{2}}{a+(a-2)(2\Delta\lambda/W)^{2}}, \qquad (2.30)$$

where a is determines the tail of the line shape, and W is the half width at half maximum (HWHM), and $\Delta\lambda$ is a relative wavelength from the center wavelength. When the value is large, the line shape is similar to a Lorentzian line shape.

Figure 2.3 shows calculated emission spectra of the N_2 $C^3\prod_u$ - $B^3\prod_g$ transitions. The emission spectra are calculated at different rotational temperatures of 300, 400, and 500 K. The calculated emission spectra are normalized at the 2-0 band head at 380.4 nm.

The distributions of the emission intensities of one vibration band depends on the rotational temperatures, and the relative intensities in the short wavelength side of the band head at 380.4 nm were increased with increasing rotational temperature. The wiggles in the spectra are due to the band structures caused by the triplet splitting of the P, Q and R branches. The relative positions of the rotational energy levels become wider in high rotational levels J. Therefore, the wiggles can be clearly seen in the region of the short wavelength for one vibrational band.

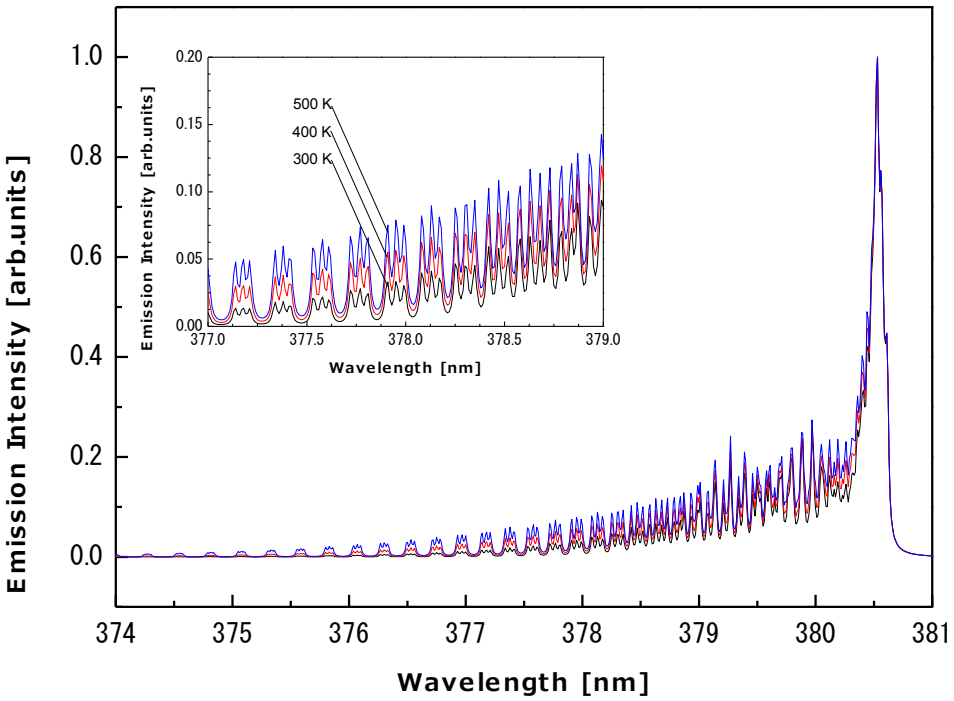

Figure 2.3 The calculated emission spectra of the N_2 $C^3\prod_u$ - $B^3\prod_g$ transition (0-2) at the rotational temperature of 300, 400 and 500 K.

2.4 Quadruple Mass Spectrometer (QMS)

Quadruple mass spectrometer (QMS) is widely used for the analysis in many fields. Mass spectrometry is the detection method for ions by ionizing the object species and selecting the ions by the ratio of the mass to the ionic charge (m/z). Figure 2.4 shows the schematic diagram of construction of QMS. The object species are ionized in the ionization chamber. Applying the voltage superposing the high frequency on the direct current voltage [± (U + Vcosωt)] to the four electrodes, the only ions of specific m/z oscillate stably in the quadrupole electrodes because those amplitude are getting large as the ions travel in the electrodes. Then, ions can be selected by m/z. Varying the high frequency voltage V with keeping U/V constant, the ions of m/z enter the detector by following equation:

$$\mathrm{m/z} = C\frac{V}{r_0^2 f^2} \qquad (2.31)$$

where C, r_0, and f are the constant, the distance from the center to the surface of the electrodes, and the frequency, respectively. Secondary electrons by the ions through the quadrupole electrodes are amplified in a secondary electron multiplier (SEM). QMS is usually used by ionizing parent molecules in the chamber by electron beam at more than several ten eV. In this case, species ionized from both parent molecules and radicals are detected. In chapter 3, the ammonia generated from high density H_2/N_2 plasma was measured by QMS. The mass spectrometer (Hiden EQP) with an orifice of 0.5 mm in a diameter was attached to the wall. The inside of the mass spectrometer was differentially pumped by a turbo molecular pump. The ionic or neutral species in the plasma introduced from the chamber into the mass spectrometer through the orifice and neutral species were ionized in the ionization chamber by and electron beam from

an oxide-coated iridium filament. The inside of the mass spectrometer was differentially pumped by 50 L/s turbo-molecular pump.

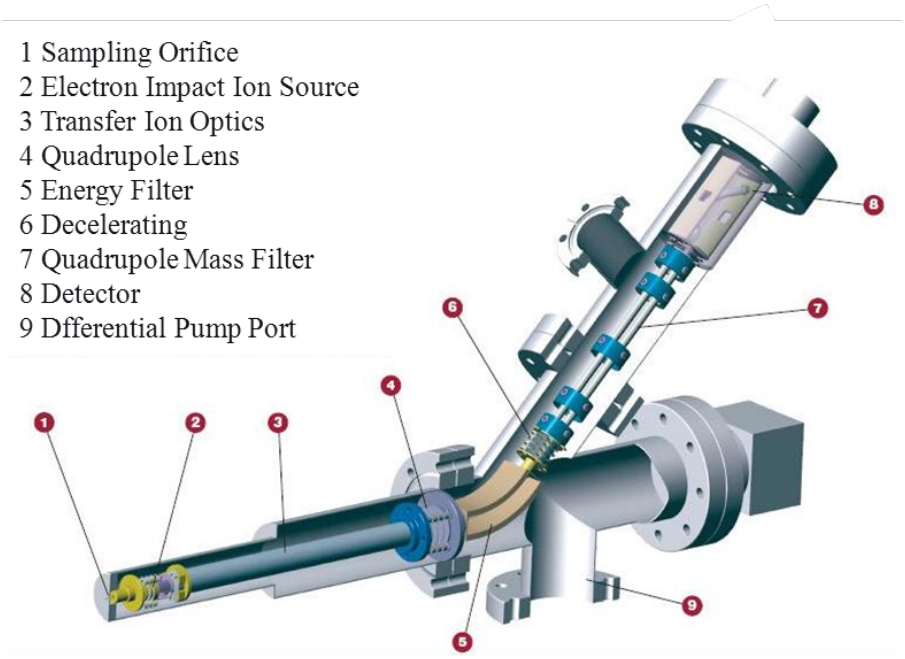

(a)

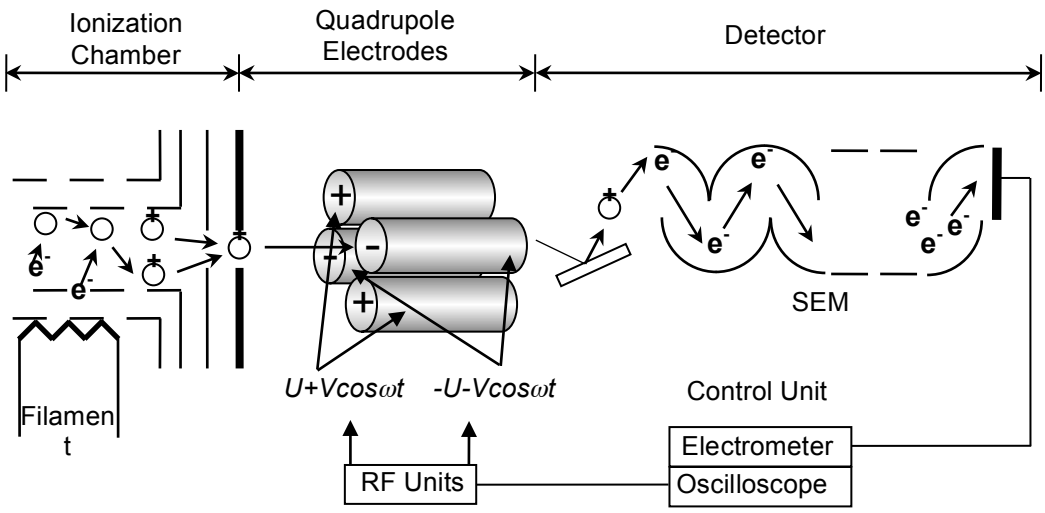

(b)

Figure 2.4 Schematic diagram of (a) the configuration and (b) the principle of QMS.

2.5 X-ray Photoelectron Spectroscopy (XPS)

X-ray photoelectron spectroscopy (XPS) is currently the most widely used surface-analytical technique, and is therefore described here in more detail than any of the other techniques. At its inception by Seigbahn and coworkers [23], it was called ESCA (electron spectroscopy for chemical analysis), but the name ESCA is now considered too general, because many surface-electron spectroscopies exist, and the name given to each one must be precise. The name ESCA is, nevertheless, still used in many places, particularly in industrial laboratories and their publications. Briefly, the reasons for the popularity of XPS are the exceptional combination of compositional and chemical information that it provides its ease of operation, and the ready availability of commercial equipment.

The surface to be analyzed in irradiated with soft X-ray photons. When a photon of energy hν interacts with an electron in a level X with the binding energy E_B (E_B is the energy E_K of the K-shell in Fig. 2.5), the entire photon energy is transferred to the electron, with the result that a photoelectron is ejected with the kinetic energy

$$E_{kin}\,(_{hv}, X) = h\nu - E_B - \Phi_s \qquad (2.32)$$

where Φ_s is a small, almost constant, work function term.

Obviously, hν must be greater than E_B. The ejected electron term can come from a core level or from the occupied portion of the valence band, but in XPS most attention is focused on electrons in core levels. Because no two elements share the same set of electronic binding energies, measurement of the photoelectron kinetic energies enables elemental analysis. In addition, Eq. (2.32) indicates that any changes

in E_B are reflected in E_{kin}, which means that changes in the chemical environment of an atom can be followed by monitoring changes in the photoelectron energies, leading to the provision of chemical information. XPS can be used for analysis of all elements in the periodic table except hydrogen and helium.

Although XPS is concerned principally with photoelectron and their kinetic energies, ejection of electron by other processes also occurs. An ejected photoelectron leaves behind a core hole in the atom. The sequence of events following the creation of the hole is shown schematically in Fig. 2.12 (right side). In the example, the hole has been created in the K-shell, giving rise to a photoelectron, the kinetic energy of which would be ($hv - E_K$), and is filled by an electronic transition from the unresolved L_{23} shell. The energy $E_K - E_{L23}$ associated with the transition can then either be dissipated as a characteristic X-ray photon or given up to an electron in the same or a higher shell, shown in this example also as the L_{23}. The second of these possibilities is called the Auger process after its discoverer [24], and the resulting ejected electron is called an Auger electron and has kinetic energy given by:

$$E_{kin}(KL_1L_{23}) = E_K - E_{L1} - E_{L23} - E_{inter}\,(L_1L_{23}) + E_R - \Phi_s \qquad (2.33)$$

Where E_{kin} (KL_1L_{23}) is the interaction energy between the holes in the L_1 and L_{23} shell and E_R is the sum of the intra-atomic relaxation energies. X-ray photon emission and Auger electron emission are obviously competing processes, but for the shallow core levels involved in XPS and AES the Auger process is for more likely.

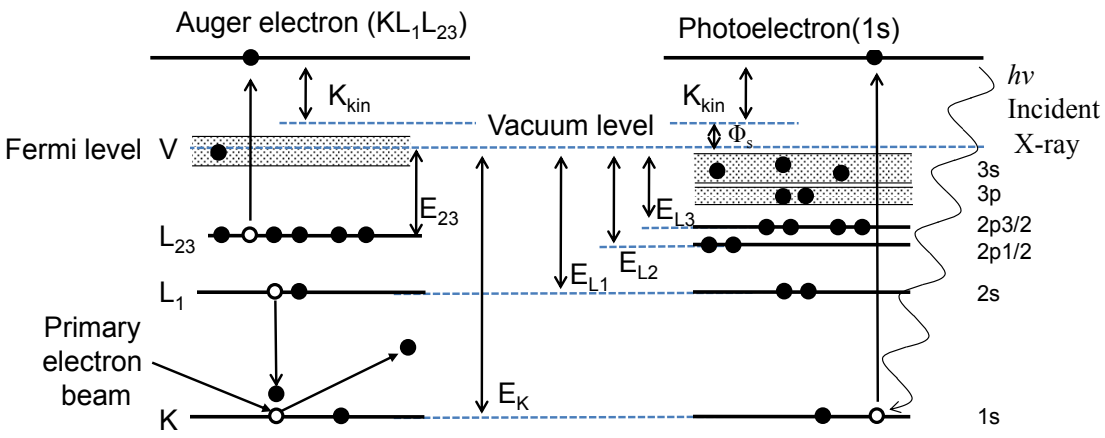

Figure 2.5 Schematic diagram of electron emission processes in solids. Left side: Auger process, right side: photoelectron process. Electrons involved in the emission processes are indicated by open circles.

2.6 X-ray Diffraction (XRD)

X-ray diffraction (XRD) is a versatile, non-destructive technique that reveals detailed information about the chemical composition and crystallographic structure of natural and manufactured materials.

A crystal lattice is a regular three-dimensional distribution (cubic, rhombic, etc.) of atoms in space. These are arranged so that they form a series of parallel planes separated from one another by a distance d, which varies according to the nature of the material. For any crystal, planes exist in a number of different orientations each with its own specific d-spacing.

2.6.1 Constructive interference

When a monochromatic X-ray beam with wavelength lambda is projected onto a crystalline material at an angle theta, diffraction occurs only when the distance traveled by the rays reflected from successive planes differs by a complete number n of wavelengths.

2.6.2 Bragg's law

By varying the angle theta, the Bragg's Law conditions are satisfied by different d-spacing in polycrystalline materials [25, 26]. Plotting the angular positions and intensities of the resultant diffracted peaks of radiation produces a pattern, which is characteristic of the sample. Where a mixture of different phases is present, the resultant diffract gram is formed by addition of the individual patterns. The diagram of Bragg diffraction was shown as Fig.2.6.

$$n\lambda = 2d\sin(\theta) \qquad (2.\ 34)$$

Based on the principle of X-ray diffraction, a wealth of structural, physical and chemical information about the material investigated can be obtained. A lot of techniques for various material classes are available, each revealing its own specific details of the sample studied.

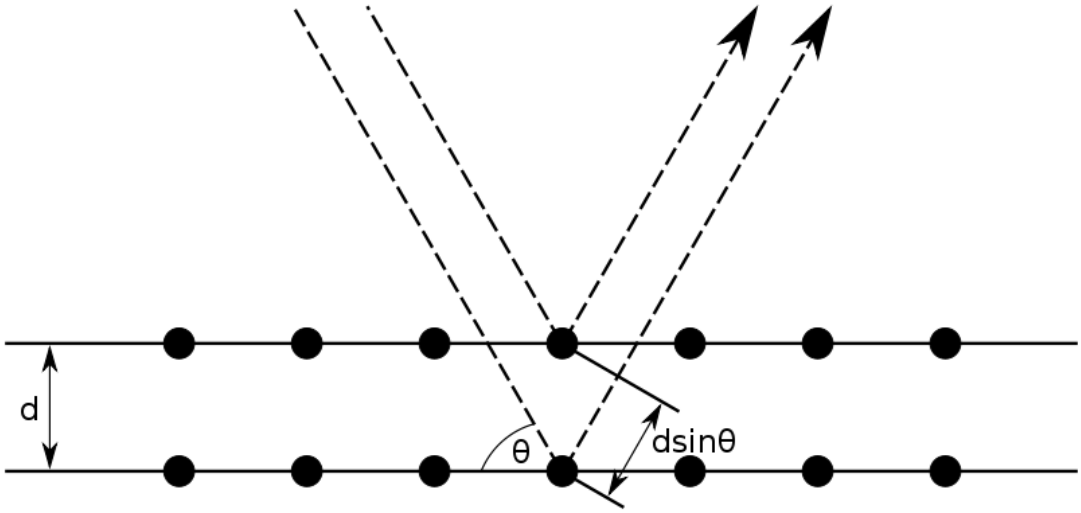

Figure 2.6 Bragg diffraction: Two beams with identical wavelength and phase approach a crystalline solid and are scattered off two different atoms within it. The lower beam traverses an extra length of 2dsinθ. Constructive interference occurs when this length is equal to an integer multiple of the wavelength of the radiation.

2.6.3 Application in materials science

X-rays are frequently used to study the internal (crystalline) structure of materials. An X-ray beam impinging on a crystal will be scattered in all directions by the atoms of the crystal. In some directions, an increased intensity is observed due to the constructive interference of the scattered waves.

Symmetric scans can give us information of the length of a period, total length of super lattice layers and quality of the material. There are two basic types of symmetric scans: theta-two theta (θ-2θ) scan and omega scan (Rocking curve). Latter one will be introduced.

From a rocking curve measurement it is possible to determine the mean spread in orientation of the different crystalline domains of a non-perfect crystal. If the crystalline particles are very small, it is also possible to determine their size by measuring a RC scan. In order to obtain a rocking curve scan, one first performs a θ-2θ scan. Note that this can be carried out in symmetric, asymmetric or skew-symmetric geometry. In the next step, the angle θ, and the detector position 2θ, is fixed at the Bragg angle of the corresponding reflection. A rocking curve scan is then acquired by varying the orientation of the sample by an angle Δω around its equilibrium position, while keeping the detector position fixed. The width of this peak will be determined by several factors. The first and most interesting contribution comes from the spread in crystalline orientation between the different domains. The second factor is based on the lateral size of the crystalline domains [28].

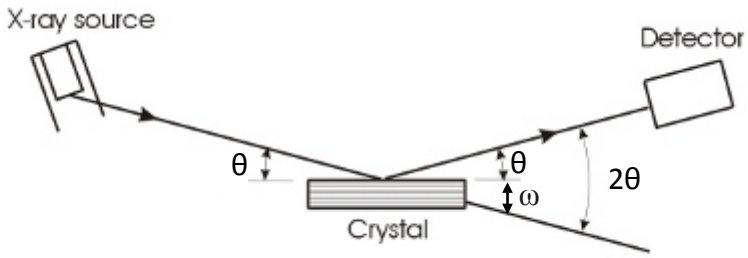

Figure 2.7 Setup of symmetric scan [27].

2.7 Photoluminescence (PL)

Photoluminescence (PL) is the spontaneous emission of light from a material following optical excitation. An electron that has been excited above the conduction band of a material will eventually fall and recombine to the hole that has been excited below the valance band after losing some energy through releasing a phonon to the lowest available non-radiative energy level. The efficiency of photoluminescence signal is determined by the nature of optical excitation, properties of material; i.e. radiative and non-radiative recontamination and defects [29].

2.7.1 Experimental technique

A laser tuned to a wavelength close to the band gap energy of the sample is directed onto the sample. This may be held in a cryostat to facilitate measurements being taken at low temperatures. A rapidly pulsing laser can be used as a quasi-constant beam laser since measurements are taken continuously. When the laser beam is incident on the sample, photoluminescence occurs and light is emitted from the sample at wavelengths dependent on the sample composition. The sample is oriented such that the reflected laser beam and the PL emission propagate in different directions. The emitted light is directed into a fiber optic cable and then into a spectrometer. A filter may be placed in front of the fiber input to remove any incident laser light. Inside the spectrometer, a diffraction grating diffracts different wavelengths in different directions towards an array of photo-detectors that measure the intensity of each wavelength component. The digital information is interpreted by the computer,

which can display a PL spectrum. The spectrum indicates the relative intensities of light of different wavelengths entering the detector. A simple diagram of PL experimental setup was shown in Fig. 2.8.

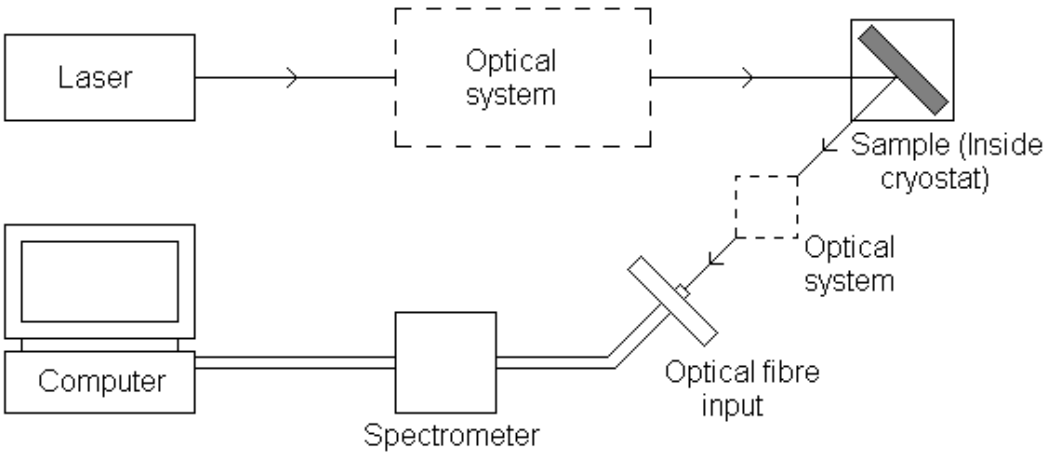

Figure 2.8 Diagram of PL experiment setup [29].

2.7.2 PL spectrum

An example of an experimentally obtained PL spectrum is shown in Fig. 2.9. The peak intensity occurs at a wavelength of 365 nm, which corresponds to photon energy of 3.4eV, the accepted energy width of the band gap of wurtzite GaN.

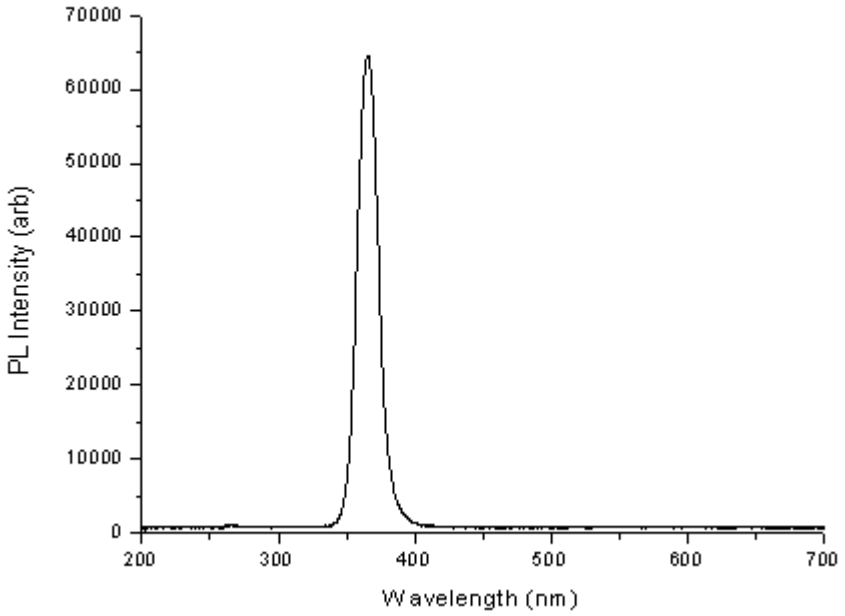

Figure 2.9 PL Spectrum for a template sample of wurtzite structure GaN excited by a 266nm laser [29].

2.7.3 PL peak position: Energy levels

In the bulk of a crystalline material, translational symmetry leads to the formation of electronic energy bands. Defects and impurities break the periodicity of the lattice and perturb the band structure locally. The perturbation usually can be characterized by a discrete energy level that lies within the band gap. Depending on the defect or impurity, the state acts as a donor or acceptor of excess electrons in the crystal. Electrons or holes are attracted to the excess or deficiency of local charge due to the impurity nucleus or defect, and Coulomb binding occurs [29].

When the temperature is sufficiently low, carriers will be trapped at these states. If these carriers recombine radiatively, the energy of the emitted light can be analyzed to determine the energy of the defect or impurity level. Shallow levels, which lie near the conduction or valence band edge, are more likely to participate in radiative recombination, but the sample temperature must be small enough to discourage thermal activation of carriers out of the traps. Deep levels tend to facilitate nonradiative recombination by providing a stop-over for electrons making their way between the conduction and valence bands by emitting phonons. Several intrinsic and impurity transitions are illustrated in Fig 2.10.

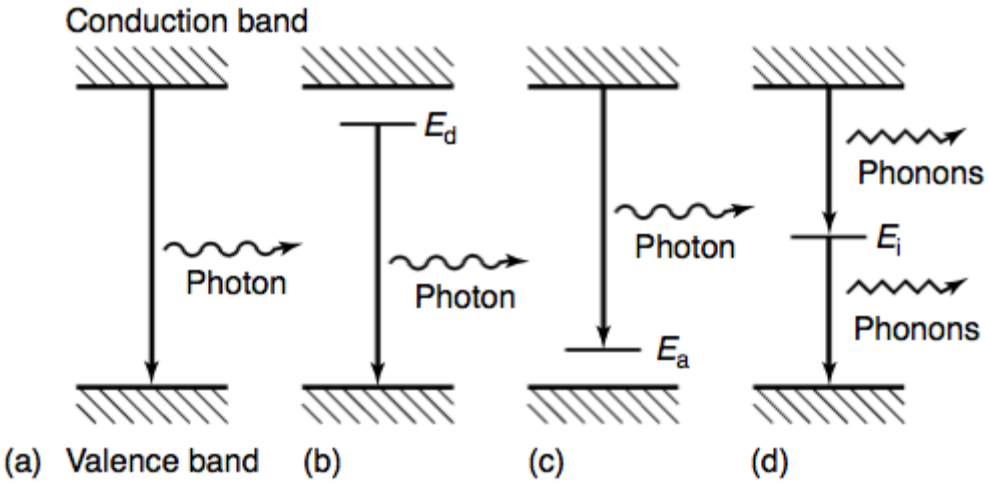

Figure 2.10 (a-c) Radiative recombination paths: (a) band-to-band; (b) donor to valence band; (c) conduction band to acceptor; (d) Nonradiative recombination via an intermediate state [29].

2.8 Reference

[1] A. C. G. Mitchell and M. W. Zemansky, Resonance Radiation and Exited Atoms (Cambridge, London 1961).

[2] S. Takashima, M. Hori, T. Goto, A. Kono, M. Ito and K. Yoneda: Appl. Phys. Lett. **75** (1999) 3929.

[3] S. Takashima, S. Arai, M, Hori, T. Goto A. Kono, M. Ito, and K. Yoneda, J. Vac. Sci. Technol. A **19** (2001) 599.

[4] H. Nagai, M. Hiramatsu, M. Hori, and T. Goto: Rev. Sci. Instrum. **74** (2003) 3453.

[5] R. S. Freund, J. A. Schiavone, and D. F. Brader: J. Chem. Phys. **64** (1976) 1122.

[6] K. Ito, N. Oda, Y, Hatano, and T. Tsuoi: Chem. Phys. **21** (1977) 203.

[7] S. Djurovic and J. R. Roberts: J. Appl. Phys. **74** (1993) 6558.

[8] J. W. Corburn and M. Chen: J. Appl. Phys. **51** (1980) 3134.

[9] Y. Kawai, K. Sasaki, and K. Kadota: Jpn. J. Appl. Phys. **36** (1997) L1261.

[10] R. E. Walkup, K. L. Saenger, and G. S. Sewyn: J. Chem. Phys. **84** (1986) 2668.

[11] H. M Katsch, A. Tewes, E. Quandt, A. Goehlich, T. Kawetzki, and H. F. Dobele: J. Appl. Phys. **88** (2000) 6232.

[12] S. F. Durrant and M. A. B. Moraes: J. Vac. Sci. Technol. A **13** (1995) 2513.

[13] S. F. Durrant and M. A. B. Moraes: J. Vac. Sci. Technol. A **16** (1998) 509.

[14] A. Gicquel, M. Chenevier, Kh. Hassouni, A. Teserepi, and M. Dubus: J. Appl. Phys. **83** (1998) 7504.

[15] G. Herzberg: *Molecular Spectra and Molecular Structure Vol. I*, (Krieger Publishing Company, Florida, 1966), p. 552.

[16] G. Herzberg: *The Spectra and Structures of Simple Free Radicals*, (Cornell University Press, 1971), Chapter 2, p. 24.

[17] G. Herzberg, *Molecular Spectra and Molecular Struct*ure *Vol. I*, (Krieger Publishing Company, Florida, 1966), Chapter 5, p.235.

[18] G. Hartmann and P. C. Johnsont: J. Phys. B: Molec. Phys. **11** (1978) 1957.

[19] H. Hönl and F. London: Z. Physik **33** (1925) 803.

[20] G. Herzberg: *Molecular Spectra and Molecular Structure Vol. I*, (Krieger Publishing Company, Florida, 1966), Chapter 5, p.219.

[21] G. Herzberg: *Molecular Spectra and Molecular Structure Vol. III*, (Krieger Publishing Company, Florida, 1966), Chapter 2, p.226.

[22] D. M. Phillips: J. Phys. D: Appl. Phys. **8** (1975) 507.

[23] K. Siegbahn, C. Nordling, A. Fahlman, R. Nordberg, K. Hamrin,J. Hedman, G. Johnsson, T. Bergmark, S.-E. Karisson, I. Lindgreen, and B. Lindberg: *ESCA: Atomic, Molecular, and Solid Sate Structure Studied by Means of Electron Spectroscopy*. (Almqvist and Wiksells, Uppsala, 1967).

[24] P. Auger: J. Phys. Radium **6** (1925) 205.

[25] Neil W. Ashcroft and N. David Mermin: Solid State Physics (Harcourt: Orlando, 1976).

[26] W. L. Bragg: *The Diffraction of Short Electromagnetic Waves by a Crystal*, Proceedings of the Cambridge Philosophical Society **17** (1913) 43.

[27] B. D. Cullity and S. R. Stock: *Elements of X-Ray Diffraction* (Addison-Wesley, 2001)

[28] Nuclear and radiation physics section, University of Leuven: http://fys.kuleuven.be/iks/nvsf/experimental-facilities/x-ray-diffraction-2013-bruker-d8-discover

[29] T. H. Gfroerer: "*Photoluminescence in Analysis of Surfaces and Interfaces*", Encyclopedia of Analytical Chemistry (John Wiley & Sons Ltd, 2006).

Chapter 3

Development of High Density Radical Source

3.1 Purpose

The growth technology of nitride films is common by means of molecular beam epitaxy (MBE) [1], metal organic chemical vapor deposition (MOCVD) [2], and hydride vapor phase epitaxy (HVPE) [3]. Because the MBE could offer to decrease in growth temperature, it enabled to suppress volatilization of an element such as indium from the InGaN [4]. However, the nitride growth with the MBE was suffered in high mosaicity and low growth rate (typical growth rate is around 0.5 μm/h). In the typical MBE system, metallic species such as gallium are supplied by thermal evaporation. Simultaneously atomic nitrogen species (so-called N radical) are supplied conventionally by plasma sources, which are utilized radio-frequency (rf) generated plasmas. Komaki *et al*. have been found that the molar fraction of InN was increased with increasing of flow rate of nitrogen. At low flow rate of nitrogen, the formation of phase separation due to dissociation of InN and condensation of indium on the growing surface were observed [5]. This was interpreted by correlation of the flux of N radical to substrate with the flow rate of nitrogen. Thus, they pointed out that the flux of N radical was pivotal in nitride growth [5]. Kushi *et al*. have reported results with high growth rates of 1.2 – 1.4 μm/h by improvement of production of N radical. They speculated that the large supply of N radical brought the high rates for growth of nitride [6]. The author, however, pointed out that the results were evidenced qualitative evaluation of the N radical on the basis of optical emission spectroscopy

(OES) measurements. Therefore, it needs to evaluate absolute density for a monitor and a control of deposited-species (molecule, ion, and atom) generated by nitrogen plasmas. Overall, the above results indicated that higher flux of N radical into substrate may improve both the mosaicity and the growth rate of nitride films.

Hence, the author aims to improve the efficiency of atomic nitrogen source with an increase of the density of N radical. For providing the radical source with high-density, increasing the plasma densities has been a strong candidate. So far, mainly two types of N radical source have been employed for the growth of nitride films: the one is electron cyclotron resonance (ECR) plasma and the other is inductively coupled plasma (ICP). Latter is commonly used to achieve the better quality of nitride films since a large fraction of N radical could be generated [7]. In the case of a fixed power and pressure, to improving the fraction of dissociation is to reduce the energy loss in plasma. There have been reports that dissociation fraction of nitrogen molecular (N_2) is lower than 1% in the typical nitrogen plasma while applying radio-frequency (rf) power (13.56 MHz) [8], because of the high dissociation energy of N_2 of 9.8 eV [9].

In the monitor for N radical, the optical emission spectroscopy (OES) was conventionally used. Hughes *et al*. reported that the ICP source provided a larger fraction of atomic nitrogen and a 1st-positive series excited molecular nitrogen in contrast that the ECR plasma source mainly produced a 2nd-positive series excited molecular nitrogen and nitrogen molecular ions when operated under the same conditions [7]. For the quantitative investigation, since the intensities of emission in the OES depended on both electron density and the electron temperature of plasmas, the dissociation fraction of N_2 might be significantly influenced when the electron

temperature was changed. Therefore, the intensity of N radical lines can't directly reflect on its density. Osaka has been reported the flux of N radical estimated by the appearance mass spectroscopy and also pointed out that the N radical was essential species in grown of nitride [10]. Besides the actinometry [11] and the NO titration [12] have been also carried out to measure the density of radical, however, the absorption spectroscopy is the suitable way to monitor the absolute density of radical *in-situ* and with no addition of tracer gas. Hence, in this study, the absolute density of nitrogen atoms was measured by vacuum ultraviolet absorption spectroscopy (VUVAS) [13, 14].

3.2 Optimizing the *in-house* radical source

3.2.1 Experimental setup

The measuring for actual radical density were carried out at another chamber (called the VUVAS chamber), which pumped down by turbo-molecular-pump to a background pressure of 5×10^{-5} Pa. The vacuum ultraviolet (VUV) light was collimated by a MgF_2 lens, passed through the plasma, focused on the entrance slit of a VUV monochromator by another MgF_2 lens, and detected by a photomultiplier tube; the two MgF_2 lenses also served as vacuum-sealed windows. The PMT output signal was converted to digital signal by recorded with a digital oscilloscope and averaged by a personal computer. By comparing of the signal intensities before and after absorption and by subtraction of those for background emissions with supply of an on-off modulated dc power (10 Hz) to the VUV lamp, then absorbance could be obtained and calculate the radical density. Moreover, the OES was carried out from the end of sources to monitor the discharge mode of plasma. Details in the radical measurement were previously described elsewhere [13-15]. Moreover, the optical emission spectroscopy was carried out from the end of the sources to monitor the discharge mode of plasma. The QMS, which used to estimate the density of molecular, will be mentioned later. The experimental set up of measurement system is shown in Fig.3.1.

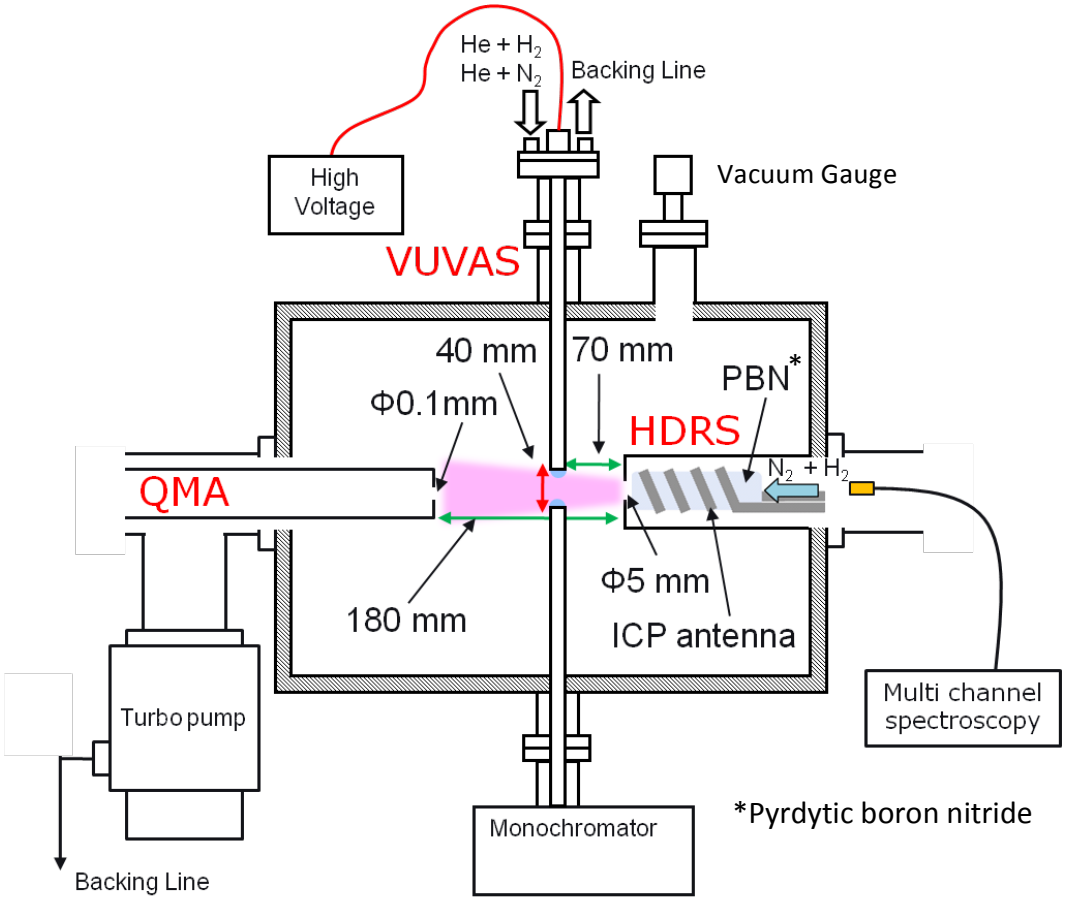

Figure 3.1 Experimental set up for VUVAS and QMS with radical source.

3.2.2 Absolute density of atomic nitrogens

In the conventional radical source (CRS) mounted VUVAS chamber, the density for N radical (n_N) was measured around 2.2×10^{11} atoms cm^{-3}. For the initial state of the high density radical source (namely *in-house* radical source), which has ICP coil antenna with 7 turns and discharge tube made of PBN, a density was measured as similar as that for the CRS's. The schematic diagram of *in-house* radical source is show in Fig.3.2. By starting this setup for the source by a copper sheet, we modified number of coil turns connect the ICP coil, that is, by changing the position of connect to coil to change the number of ICP coil turns. As described later, after optimizing the configuration of the *in-house* radical source, the density of N radical from the HDRS was measured around 2.3×10^{12} atoms cm^{-3}.

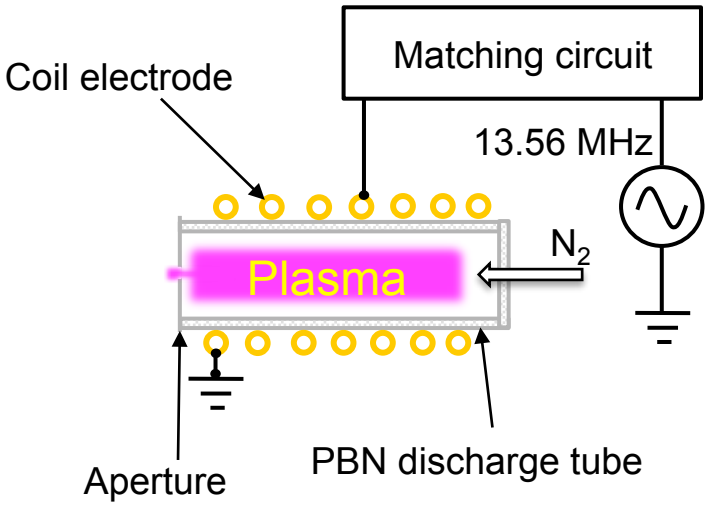

Figure 3.2. Schematic diagram of *in-house* radical source.

In detail of the optimization of *in-house* radical source, the absolute densities of N radical as a function of the number of ICP coil turns in different pressures are shown in Fig. 3.3. The highest density for N radical is obtained 3.6×10^{11} atoms cm^{-3} with 4 turns at 0.8 Pa, and N_2 flow rate of 30 sccm. As the number of ICP coil turns were reduced from 7 to 4, the density of N radical was increased from 0.5 to 3.6×10^{11} atoms cm^{-3}. As pressures increased from 0.1 to 0.8 Pa by increasing the N_2 flow rates from 5 to 30 sccm, the density of N radical also was increased from 0.5 to 3.7×10^{11} atoms cm^{-3}. On the other hand, the spacial distribution of radical density may changed when changing the work pressure. However, the spacial distribution of radical density in the remote region is also strongly dependent on the structure of aperture since the reflection occurred at the hole of aperture.

On the basis of the elementary circuit model, absorbed power coupled inductively with the plasma is in proportion to electrical currents of rf source, that is, inversely to the turns of the coil. Under the circumstance of keeping with constant power, it could be considered that the efficiency of coupling with the plasma was improved by reducing the number of coil turns [16].

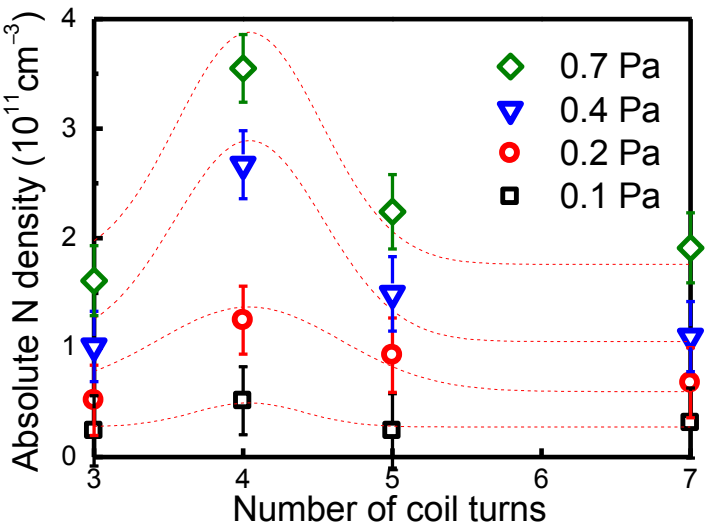

Figure 3.3 The absolute density of N radical as a function of the number of ICP coil turns at working pressures from 0.1 to 0.7 Pa.

When coil turns of rf antenna (N) were reduced, the n_N is increased on the basis of energy loss mechanism in the ICP. In a principal of uniform density cylindrical ICP discharge, the model of the source can be described as the transformer shown in Fig.3.4 [16]. Evaluating the inductance matrix for this transformer, defined through

$$\tilde{V}_{\mathrm{rf}} = j\omega L_{11}\tilde{I}_{\mathrm{rf}} + j\omega L_{12}\tilde{I}_{\mathrm{p}} \qquad (3.1)$$

$$\tilde{V}_{\mathrm{p}} = j\omega L_{21}\tilde{I}_{\mathrm{rf}} + j\omega L_{22}\tilde{I}_{\mathrm{p}} \qquad (3.2)$$

Where the tildes denote the complex amplitudes, for example, can obtain

$$L_{11} = \frac{\mu_0 \pi b^2 N^2}{l} \qquad (3.3)$$

$$L_{12} = L_{12} = \frac{\mu_0 \pi R^2 N^2}{l} \qquad (3.4)$$

Where N is the turns of coil antenna, l is the length of plasma, μ_0 is the vacuum permeability, b is the inside diameter of coil antenna, R is the diameter of plasma. From Fig.3.4, the impedance from at the coil terminals can be solve

$$Z_{\mathrm{s}} = \frac{\tilde{V}_{\mathrm{rf}}}{\tilde{I}_{\mathrm{rf}}} = j\omega L_{11} + \frac{\omega^2 L_{12}^2}{R_p + j\omega(L_{22}+L_{\mathrm{p}})} \qquad (3.5)$$

Where $R_p = \frac{\pi \mathrm{R}}{\sigma_{\mathrm{eff}} l \delta_{\mathrm{p}}}$, and $L_p = \frac{R_p}{v_{\mathrm{eff}}}$ defined though total induced rf current amplitude in the plasma skin and the plasma resistance through $P_{\mathrm{abs}} = \frac{1}{2}\tilde{I}_{\mathrm{p}}{}^2 R_{\mathrm{s}}$. Hence expanding the denominator in eqs. 3.5, R_{s} is the resistance of rf antenna given by

$$R_s \approx N^2 \frac{\pi R}{\sigma_{\mathrm{eff}} l \delta_{\mathrm{p}}} \qquad (3.6)$$

Where R is radius of plasma, which is near to the diameter of the rf antenna. Therefore, the power balance relation in the inductively coupled plasma is given by

$$P_{\mathrm{abs}} = \frac{1}{2}|\tilde{I}_{\mathrm{rf}}|^2 R_{\mathrm{s}} \qquad (3.7)$$

where P_{abs} is the absorbed power by the plasma; $\tilde{I}_{\mathrm{rf}}$ is the rf source current.

Then yields the required rf source current, and the rf voltage is determined from

$$\tilde{V}_{\mathrm{rf}} \approx \tilde{I}_{\mathrm{rf}}|Z_{\mathrm{s}}| \qquad (3.8)$$

where $Z_{\mathrm{s}} = R_{\mathrm{s}} + j\omega L_{\mathrm{s}}$, and $L_{\mathrm{s}} \propto N^2$. We can see, when the P_{abs} is fixed, we can find $\tilde{I}_{\mathrm{rf}} \propto {}^{1}/_{N}$, then gives $\tilde{V}_{\mathrm{rf}} \propto N$. The relationship between coil turns and sheath thickness S_m can be given from the modified Child law

$$S_m \propto N^3 \qquad (3.9)$$

S_m can be reduced by reducing *N*. Ion energy loss across this thinner sheath can be eliminated. Therefore, the total energy loss in the plasma could be reduced by decreasing the *N*, which lead to an increase of D_{N}. Hence, when coil-turns decreased from 7 to 4, the increase of n_{N} may suggest the energy loss of ion though sheath was decreased. As we supposed that decreasing of coil-turns can reduce the thickness of sheath resulting in decreasing of the ion energy loss across the sheath to PBN wall and increase the D_{N} [16].

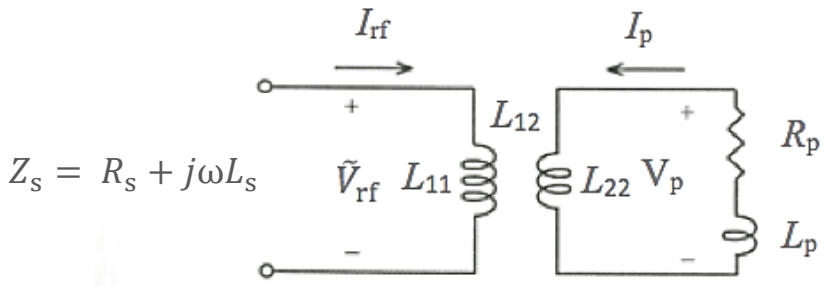

Figure 3.4 Equivalent transformer coupled circuit model of an inductive discharge [16].

Meanwhile, as the number of ICP coil turns changed, the ICP discharge region was placed at upstream side of gas flow. Pitch of the coil turns was kept as a constant, so that the volume of rf electrode was decreased when decreasing the number of coil turn. This also led to the decrease of a resident time of species in the ICP discharge region. In the case of a fixed pumping speed and gas flow rate, the velocity of species in the plasma is a constant. When the length of antenna coil decreased, it leads to the short resident time of species. The collision time between species in the plasma was decreased and then D_N decreased. This factor can be considered as one reason why the n_N decreased when coil turns decreased from 4 to 3 turns. Moreover, the n_N is seen to increase with increasing pressure. This is consistent with the power balance relation, which indicates that the density varies inversely with the effective plasma area [16]. For the rf power dependence (data not shown), no significant change of the n_N could be observed. The further investigation is needed to explain this result.

Figure 3.5 shows a result of n_N at the condition of with or without magnetic field in the radical source. A significant increase of n_N could be obtained in pressures from 0.10 to 0.75 Pa. Especially, the n_N increased from 3.7 to 8.0 × 10^{11} atoms cm^{-3} when amounts a magnetic fields to radical source at a pressure of 0.75 Pa. This phenomenon suggests primary electrons (or hot electrons) can be efficiently confined, provided there is the end confinement either with magnetic mirrors, multi-poles, or negative electrostatic potentials shown in Fig.3.6. These electrons, if created and trapped at low pressures (large mean free path compared to the discharge size) are considered to be the main ionization source for a discharge [16].

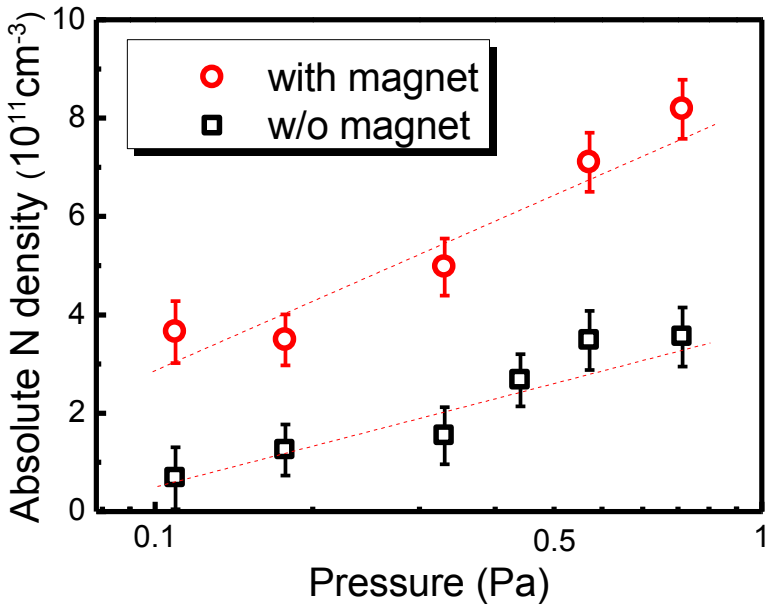

Figure 3.5 Dependence of absolute density of N radical on working pressure of with or without magnetic field.

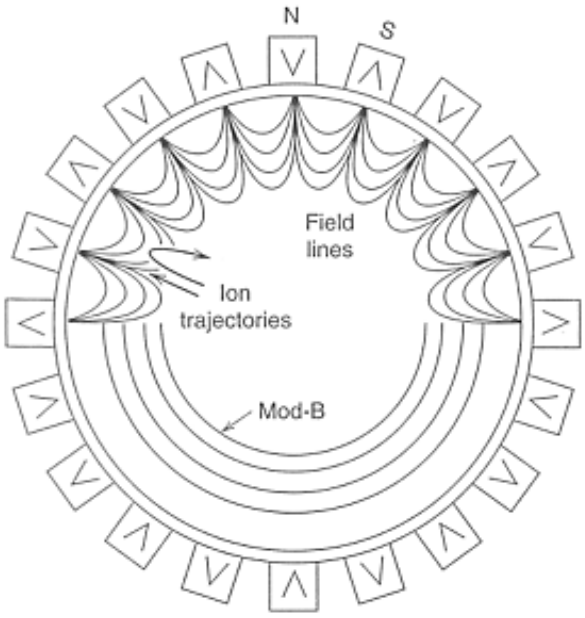

Figure 3.6 Magnetic multi-pole confinement in cylindrical geometry, illustrating the magnetic field lines and the B surfaces near the circumferential walls [16].

3.2.3 Dissociation fraction of nitrogen molecules

In order to obtain the fraction of dissociation (D_N), the N_2 molecule density calculated using the idea gas equation. The gas temperature (T_g) could be deduced from the rotational temperature (T_r) of N_2 molecules since the T_r was in equilibrium with the T_g. So the T_r can estimated by calculation fitting the measured band spectrum with a computed band spectrum of the N_2 second positive ($C^3\prod_u \rightarrow B^3\prod_g$) system [17-19]. The result of T_r as a function of pressure at ICP antenna with 4 turns is show in Fig. 3.7. The rf power was kept as a constant of 400 W. The T_r was increased from 900 to 1330 K with increasing pressures from 0.09 to 0.75 Pa. It reveals a strong dependence of T_r to the work pressure but no significant change could be observed when changing the rf power (data not shown). Hence, the T_r is supposed as a constant when changing the power density.

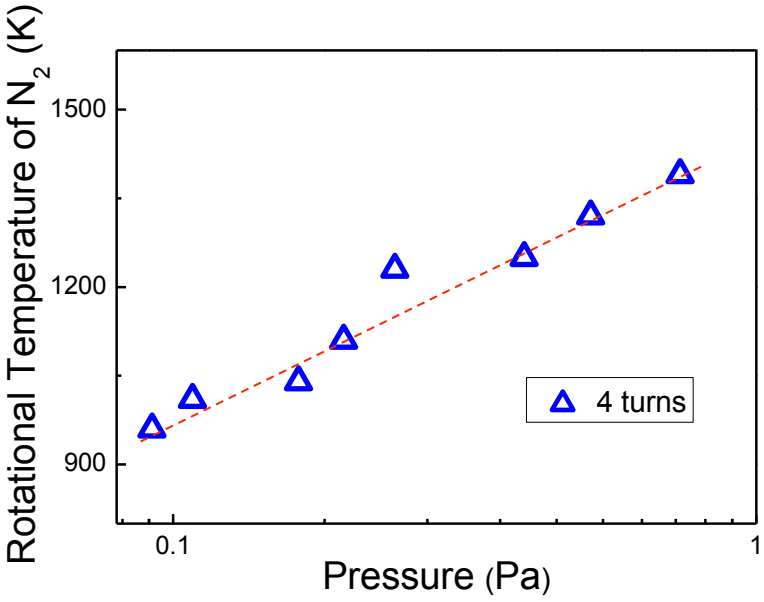

Figure 3.7 The rotational temperature of N_2 as a function of work pressure at 4 turns ICP antenna with different rf power.

Based on n_N in Fig. 3.3 and the temperatures of N_2 molecular in Fig. 3.7, the fraction of dissociation was calculated. The fraction of dissociation as a function of the number of coil turns is shown in Fig. 3.8. The highest dissociation fraction is obtained in 4 coil turns. However, it decreases when increasing pressure from 0.4 to 0.7 Pa whereas the absolute density is still increased. The difference on the trend of the pressure dependence might be explained by the balance of molecular density and its dissociation fraction. Hence, the absolute density of atomic nitrogen could be increased when increase rate of molecular density is higher than decrease rate of its dissociation fraction. This indicates that the absolute density of N radical have the highest value in 4 turn of coil electrode, and the efficiency is decreased when pressure became higher than 0.4 Pa.

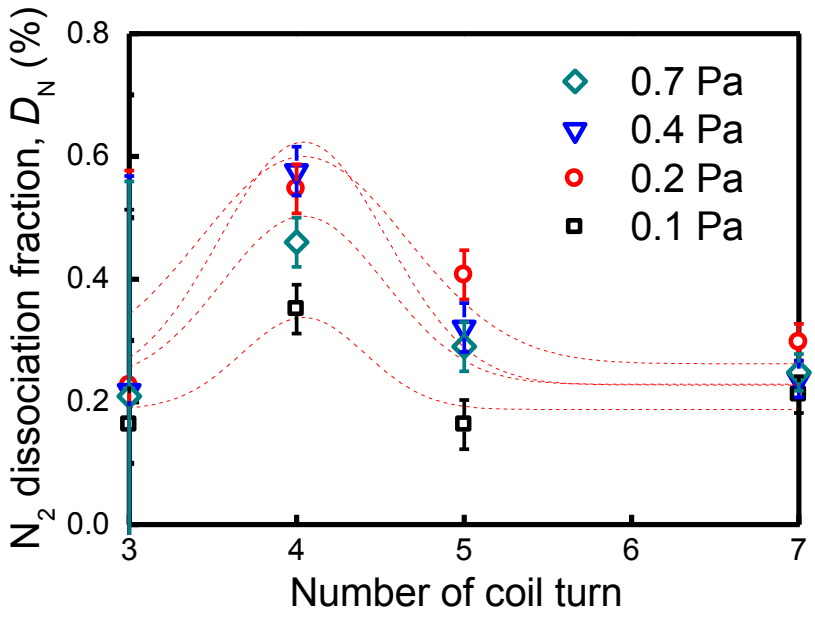

Figure 3.8 The dissociation fraction of N_2 as a function of the number of ICP coil turns at working pressure from 0.1 to 0.7 Pa.

On the other hand, the radical density should be dependent on the plasma density at the relatively low dissociation fraction, and this is a reason why introduces an external magnetic field to trap electrons for ionization [20]. The fraction of dissociation at the condition with applying a magnetic field is significant increased as shown in Fig. 3.9. According to the reflection effect of magnetic field on electrons, collisions to walls of the discharge tube should be reduced. Therefore, the electron energy was efficient to consume for the dissociation of nitrogen molecules. However, in the high pressure region, recombination of N radical might be resulted that the dissociation fraction was decreased when the pressure was increased. Consequently, the introduction of the magnetic field have significant efficient on improvement of dissociation fraction.

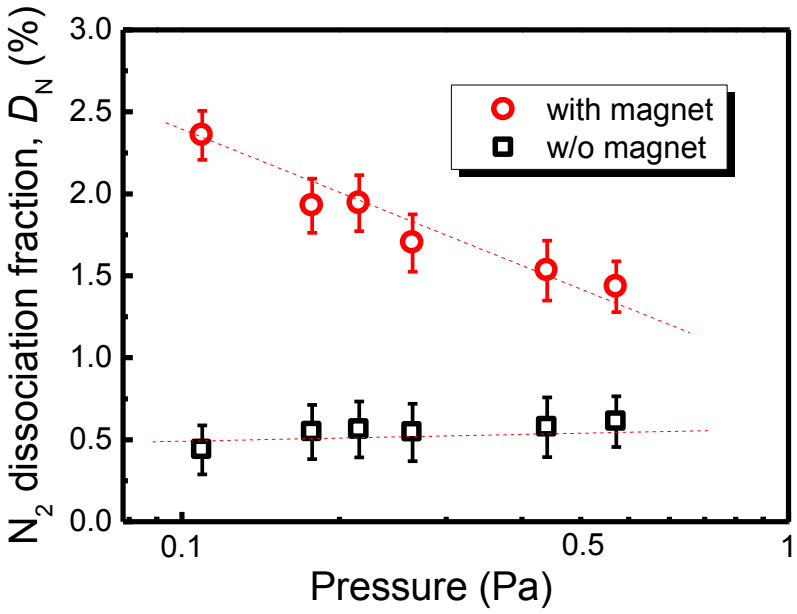

Figure 3.9 Dependence of the dissociation fraction of N_2 on working pressure of with or without magnetic field.

Based on these experimental results, the *in house* radical source is optimized to a structural configuration, which is consisted by 4 turns of coil and applying a magnetic field as shown in Fig. 3.10. The HDRS consists of an ICP coil antenna made of copper-tube and capacitively coupled plasma (CCP) electrode. The CCP electrode was set at the upstream of gas flow against the ICP was with the distance around 10 mm. Cooling-water was circulated inside the tube to maintain the temperature of the antenna and the electrode. The diameters for the ICP antenna and the CCP electrode are 26 mm for inside and 36 mm for outside. The CCP electrode is surrounded cylindrically by six permanent magnets made of Sm-Co whose N and S poles are alternately positioned. The chamber with a diameter of 25 mm and length of 90 mm is made by pyrolytic boron nitride (PBN) and is surrounded by the ICP antenna and the CCP electrodes. The photograph of HDRS was shown in Fig. 3.11.

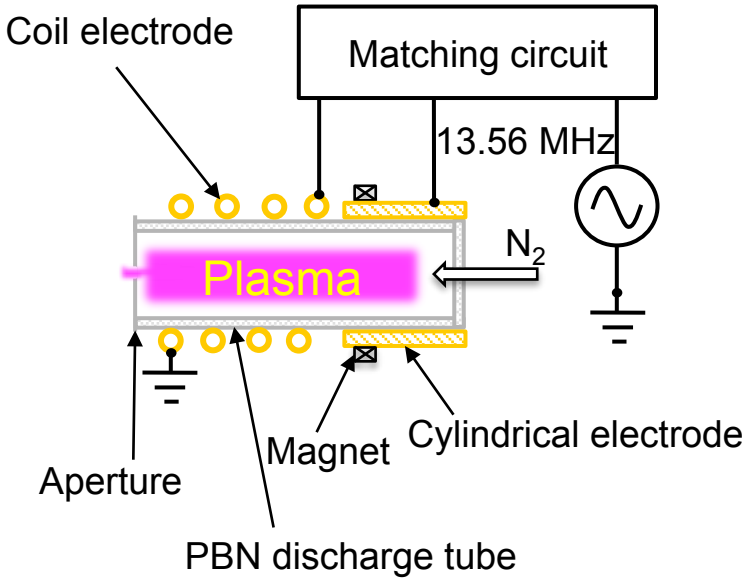

Figure 3.10 Schematic graph of optimized high density radical source.

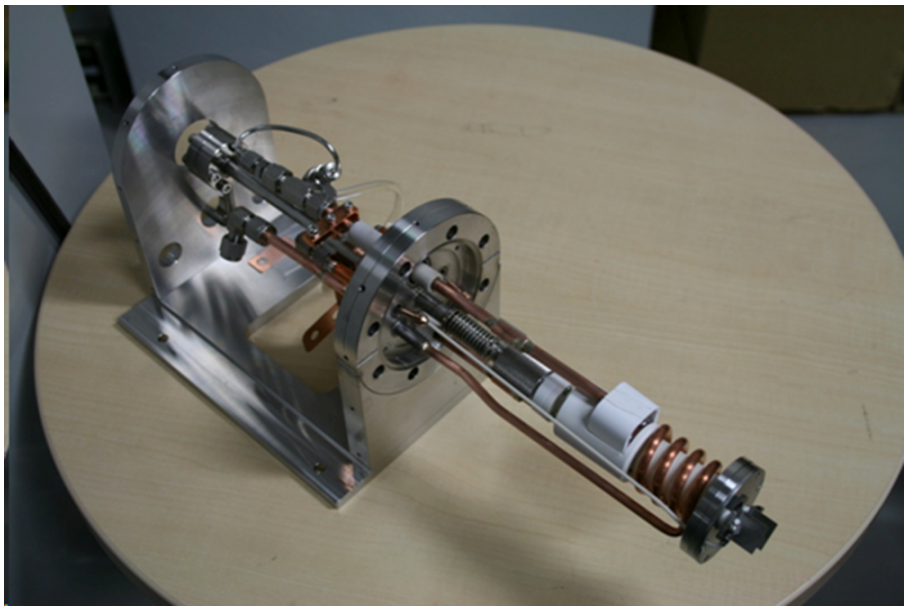

Figure 3.11 Photograph of high density radical source.

At last, a high density of N radical was obtained by optimizing the coil turns of rf antenna and introduction of magnetic field that may reduce the energy loss of plasma caused by energetic species bombardments on the discharge tube. Comparison of the density of the nitrogen radical generated by CRS and HDRS are shown in Fig. 3.12. The HDRS can generate nitrogen radical in a wide pressure range. A maximum density of 2.3 $\times 10^{12}$ atoms cm^{-3}, which corresponds to 3.2 $\times 10^{-8}$ $mol \cdot cm^{-2} \cdot s^{-1}$ was achieved. This is one order higher than the maximum value of CRS.

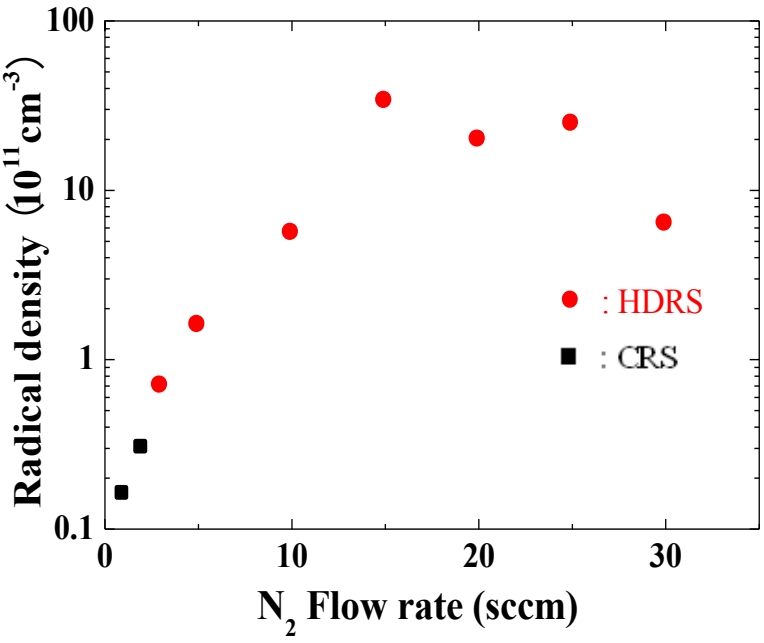

Figure 3.12 Schematic of high density radical source.

3.3 Absolute densities of N, H, and NH_3 in N_2-H_2 mixture plasmas

The plasma-assisted MBE growth of GaN film was reported by several researchers [21-23], where particularly the nitrogen (N) atom from N_2 gas dissociation excited by plasma was pointed out to be important for improving both growth rate and film quality. Furthermore, there were reports that the growth of GaN was drastically changed using ammonia gas (NH_3) plasma compared with N_2 gas plasma, owing to an effect of plasma-generated atomic hydrogen (H) [24, 25]. For the plasma-assisted MBE growth, the absolute densities of atomic H, N, and NH_3 species generated inside the plasma sources are still unclear. These species are transported to surfaces of films placed at the chamber for MBE growth under a relatively low pressure of about 1 Pa at the remote region of the radical source. Therefore, it is strongly needed to obtain information about the absolute densities of these species at the remote region of H_2 and N_2 mixture plasmas.

There are many reports about the absolute densities of the species studied in detail both experimentally [26] and theoretically [27, 28] for plasmas employing the N_2-H_2 mixture. However, there is little information about the behaviors of absolute densities at the remote region of the radical source for MBE, in which the plasma is especially kept under relatively low pressures below 2 Pa. On the other hand, some researchers pointed out that NH_3 was formed by the plasma-surface interactions [29].

In the case of MBE growth with a remote radical source, the transportation of the concerned species from the high-density plasma source to a large-volume growth chamber while maintaining a low pressure is specific and complicated. Thus, differences in density of species between the plasma reactor and the remote region of plasma sources are noticeable. Therefore, it is considerably important to know the

behaviors of absolute densities of species at the remote region that were injected from the plasma source. There has been, however, little information about the absolute densities of N, H, and NH_3 measured systematically in the remote region in MBE. The growth of GaN and related films have been developed by trial and error but the information of species incident to the surface will accelerate the development, and at the same time, the clarification of their behaviors in the complicated scheme of reactors will be very interesting from the scientific viewpoint.

This research focused on the measurement of the absolute densities of the H, N, and NH_3 at the remote region of the radical source by VUVAS and QMS, respectively. The significant phenomena of behaviors of species in the gas phase influenced by surface reactions were found. On the basis of these measured results, the behaviors of absolute densities of H, N, and NH_3 at the remote region were clarified.

The gases of N_2 and H_2 with individual controls were introduced to the radical source at a total gas flow rate of 30 sccm by mass-flow controllers, and the pressure of the MBE chamber was maintained between 0.5 and 1.4 Pa during discharges. A radio-frequency (13.56 MHz) power of 400 W was supplied to the high-density plasma source to generate the plasma.

The absolute densities of both H and the N were measured by VUVAS. A VUV light source was constructed using hollow-cathode plasmas of hydrogen- or nitrogen- diluted helium gas in atmospheric pressure. Before and after absorption measurement, light intensity was measured as reference, and then absorption was calculated.

3.3.1 Nitrogen and hydrogen radical density in N_2/H_2 mixture plasmas

Figure 3.13 shows the absolute densities of N and H radicals at the remote region with a distance of 70 mm from the radical source under about 1 Pa as a function of the ratio of N_2 and H_2 mixtures. In the case of pure N_2 plasma, the N radical density was 9×10^{12} atoms cm^{-3}. When increasing the mixture ratio for H_2 was increased, N radical density decreased steeply. On the other hand, H radical density gradually increased. For the mixture with 80% H_2 plasma, it reached 7×10^{12} atoms cm^{-3}. Thus, the high-density radical source we developed could generate potentially high H and N radical densities of the order of 10^{13} atoms cm^{-3} at the remote region even at low pressures. The VUVAS measurement accuracy in this case is approximately 30%.

Adams and Miller [30], and Amorim *et al* [31], have reported the absolute densities of atomic species in capacitively coupled plasma (CCP) reactor maintained at relatively higher pressures ranging between 200 and 700 Pa (2 – 5 Torr) by measurement using two-photon absorption laser-induced fluorescence (TALIF). They concluded that H and N radical densities was at least on the order of 10^{13} atoms cm^{-3} in the plasma region. In this study, even though the chamber was maintained at lower pressures ranging from 0.5 to 1.4 Pa, the result as shown in Fig. 3.10 indicates that the ICP radical source will supply potentially from the high-density radicals of H and N of the order of 10^{13} atoms cm^{-3} even at the remote region.

As mentioned above, the improvement in both growth rate and film quality in MBE is strongly desired, and additionally, these performances should be guaranteed precisely by the densities of species. In previous study, the spatial distribution of N radical density and the loss probability in the afterglow region was evaluated, and the loss probability of N radical at the surface of stainless steel (SS) was 0.03.

Consequently, the spatial distribution of N radical density was almost flat in the chamber [32]. So far, however, there has been little information on the H and N densities of species under the condition of film growth in the H_2/N_2 plasma-assisted MBE. It is generally believed that the densities of species during MBE will be stable temporally.

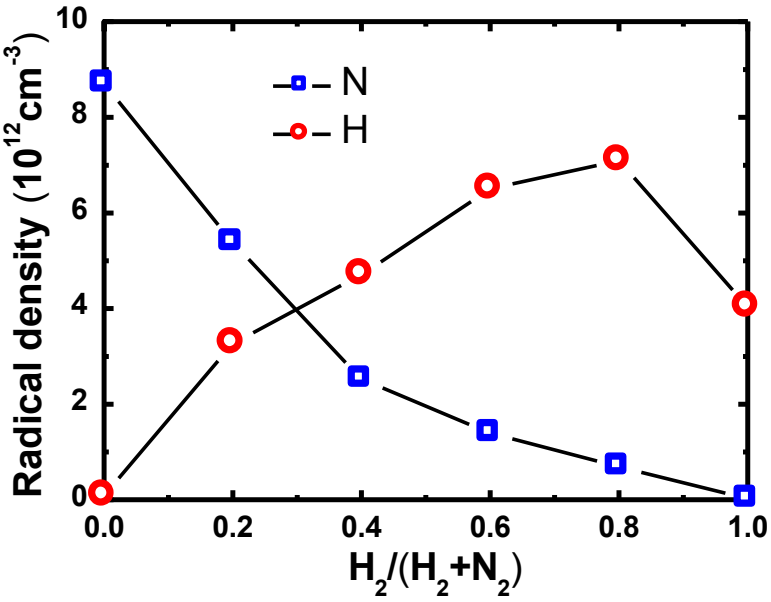

Figure 3.13 Absolute densities of N and H atoms at remote region 70 mm from the radical source as a function of the ratio of a mixture of N_2 and H_2.

3.3.2 Hydrogen memorial effect to nitrogen discharge

Figure 3.14 shows the time variation of N atom density during the sequences. Initially, when the N_2 plasma was virginally generated, the N atom density was evaluated to be about 9×10^{12} atoms cm^{-3} as long as the duration was 10 min. The N_2 gas discharge was turned off, and then the N_2 gas was completely exhausted reaching pressures of below 10^{-4} Pa. Next, the H_2 gas was introduced to the discharge tube of the radical source, and then H_2 plasma was generated for a period of 5 min. During the H_2 discharges, no N atom was detected. After the exhaust process, the N_2 plasma was generated again as described above. Just after changing the gas composition from pure H_2 to pure N_2, the N atom density was relatively low, about 5×10^{12} atoms cm^{-3}. After about 40 min, N atom density gradually increased exceeding the initial value, reached the maximum of about 2.7×10^{13} atoms cm^{-3}, and then decreased again for a while, about 10 min. The whole period of previously H_2 plasma effect to N atom density maintained around 60 min. Note that the N radical density was increased 5 times as high as that of the initial value. At this time, the OES from plasmas were measured in real time during the discharge. At the beginning of injection of N_2 gas for least 2 min, emission lines due to H atoms were observed to be weak; however, no H atom could be observed by VUVAS measurement because the H atom density was very low, which is below the detection limit of 10^9 atoms cm^{-3}.

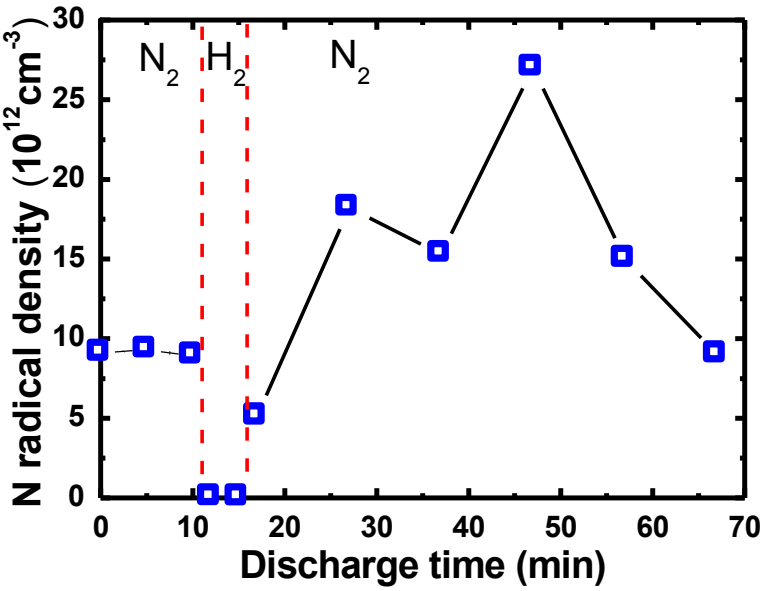

Figure 3.14 Time variation of N radical density before and after hydrogen discharge.

Notably, N radical density in pure N_2 plasma was strongly affected by surface conditions, that is, residues of H or NH_3 species on the surfaces influenced the production of N radicals. Namely, the author found out that surfaces of both the PBN for the discharge tube and the SS for the chamber would act as sites for generation of N atoms or the loss rate was suppressed. This fact means that without stabilizing surface conditions, the densities of species would considerably fluctuate temporarily. To analyze these phenomena, the author conducted N atom density measurement on a sequence of pure N_2 discharges after H_2-containing plasma discharges.

Thus, the author emphasized that the remote absolute density of N atoms was affected by the experimental history with respect to the remaining hydrogen base species for a long period of 10 min but not detectable in the OES of plasma discharge.

This instability in N atom density after applying H_2-containing plasmas indicates that a small amount of hydrogen-based species remaining at the surface of both PBN and SS possibly affected the dissociation of N_2 or nitrogen-based species. Gordiets *et al.* reported that a small admixture (less than 1%) of H_2 in N_2 greatly enhanced the dissociation of N_2 in the case of the direct-current (dc) plasma discharges [33]. The reason for the increase of N with a small admixture of H is an increase in the discharge maintaining field, thus in production rate of N atoms by electron impact dissociation of N_2. As in pure N_2, the main loss channel for N atoms is wall recombination, but, in the mixture, electron excitation of ground state atoms to $N(^2D)$, followed by the formation of NH_x also contribute to the losses. Similarly, if the surfaces were once passivated by the hydrogen atoms, there are chances for hydrogen to be desorbed and to enhance the dissociation of N_2 gas. The hydrogen from the hydrogen-passivated surface was desorbed following ion bombardment and

temperature increase. After that, all of the hydrogen were released from the surface, and the dissociation of nitrogen atoms was kept identical to that for pure N_2 gas, then reached the initial value.

Otherwise, the instability of the N atom density after applying H_2-containing plasmas indicates that the loss probability of N atoms at the surface of both the PBN and SS was possibly varied by the passivation of hydrogen on the surface. The discharge tube made of PBN has a large surface-to-volume ratio. Thus, the surface reactions were considered essential. Amorim reported that the N atom recombination probability for the BN surface is lowest from 0.0002 to 0.0009 compared with that for stainless steel from 0.0048 to 0.0075 [31]. These data were taken by measurement of the decay of atomic density during the afterglow of pulsed discharges at a relative low plasma density in a plasma reactor.

Furthermore, the chamber made of SS will enhance the surface reaction considerably with respect to the determination of remote density since the loss probability of species will be higher compared with that of dielectric materials. The atomic species and the ammonia generated in the discharge tube were introduced into the chamber while it was kept under a pressure of about 1 Pa. Under this situation, the species stayed in the chamber for a long while until pumping out. Therefore, the surface-loss mechanisms of the species affected substantially the determination of the densities. Moon and colleagues reported that the surface loss probabilities for N atoms on SS were 0.04 for pure N_2 discharges and 0.16 for 20% H_2 in N_2 [34, 35]. These results were taken by measurements of the decay of atomic density during the afterglow of pulsed discharges in a low-pressure high-density ICP reactor (300 × 200 × 200 mm^3). They also showed that the N atom density for a pure N_2 was conversely

lower than that for a mixture of H_2 and N_2 [34, 35]. Compared with our results obtained here, the tendency of the absolute density of N radicals for pure N_2 discharge was oppositely larger in the remote N_2 discharge than that for the H_2 and N_2 mixture discharges. Thus, in our radical source configuration, that is, a large surface ratio to volume ($430 \times 330 \times 330$ mm^3), the remote density of N atoms was strongly sensitive to the surface loss probability since N atoms were lost primarily on surfaces.

3.3.3 Concentration of ammonium in the N_2/H_2 mixture plasmas

The absolute density of ammonia (NH_3) generated by the plasma was measured by QMS. An orifice with a diameter of 0.1 mm for the entrance of the QMS device with differential pumping under 10^{-4} Pa was placed 180 mm from the exit of the radical source. In the mass spectra measurement of the N_2-H_2 mixture, the density of NH_4 is too small to detect. Hence, ionization of NH_3 and the prevention of NH_3 dissociation to NH_2 should be considered. By measuring the threshold energies for both ionization and dissociation of NH_3 caused by electron impact was experimentally determined to be 17 and 20 eV, respectively. In this study, only NH_3 was detected using the threshold energy of 18 eV without any dissociation. The signal intensity I of species X measured by QMS can be expressed as

$$I_X = A(X)\sigma_X(\varepsilon_b)I_b N_X \qquad (3.10)$$

where I_b and ε_b denote the current and energy of the electron beam for ionization, respectively, σ stands for the ionization cross section, N is the density, and A is the instrumental constant. As references, while pure NH_3 gas with a flow rate of 30 sccm was introduced, the QMS intensity I_{NH_3Gas} was obtained. N_{NH_3Gas} was obtained by solving the ideal gas law, and the absolute density of NH_3 generated by mixture plasmas is given by

$$N_{NH_3Plasma} = \frac{N_{NH_3Gas}}{I_{NH_3Gas}} I_{NH_3Plasma} \qquad (3.11)$$

In another aspect of a mixture of H_2 and N_2, the N atoms generated in plasmas were primarily lost at surfaces by reactions, resulting in the production of ammonia (NH_3) and related species. Figure 3. 15 shows absolute NH_3 density measured by using the QMS as a function of the mixture ratio of nitrogen and hydrogen. The NH_3

density was 2×10^{13} molecules cm^{-3} at the maximum ratio of 60% of H_2 to N_2 (measurement accuracy is approximately 20%). NH_3 could be supplied on the order of 10^{13} molecules cm^{-3} at the remote region of the radical source even at a low pressure of about 1 Pa. This indicated that NH_3 was mainly generated inside of the discharge tube. In general, it has been considered that the highest NH_3 density was obtained at a stoichiometric composition of 1:3, namely, 75% hydrogen. Most of NH_3 would be generated by surface reactions through intermediates originating from N atoms and H atoms; as follows: $N + H + surf \rightarrow NH_{surf}$, $NH_{surf} + H \rightarrow NH_2^{(surf)}$, $NH_{surf} + H_2 \rightarrow NH_3$, $NH_2^{(surf)} + H \rightarrow NH_3$ [32]. Considering the reaction rates of three-body recombination for NH_3 production, the relatively high NH_3 density of 10^{13} molecules cm^{-3} cannot be explained only by the gaseous production. Alternatively, since the proposed surface reactions have a higher rate, we preliminary believed that the major production path of NH_3 is surface reaction on the discharge tube wall. Therefore, the production of NH_3 in the surface phase is dominant rather than gaseous reactions. Thus, the surface reactions of N and H radicals on PBN generated most of NH_3. It is worth noting that the ICP radical source can introduce high-density NH_3 on the order of 10^{13} molecules cm^{-3} to the remote region even without employing any NH_3 gas, which is very important and useful for developing the N-based film growth processes in plasma-assisted MBE with H_2/N_2 gases.

In particular, the surface reactions on the PBN discharge tube greatly affected the determination of the remote densities of N, H, and NH_3. Therefore, further considerations about the surface loss probability of N and H radicals on the PBN surface are needed. These results will provide a new concept of the radical source to increase N radical density by making the most use of surface reactions.

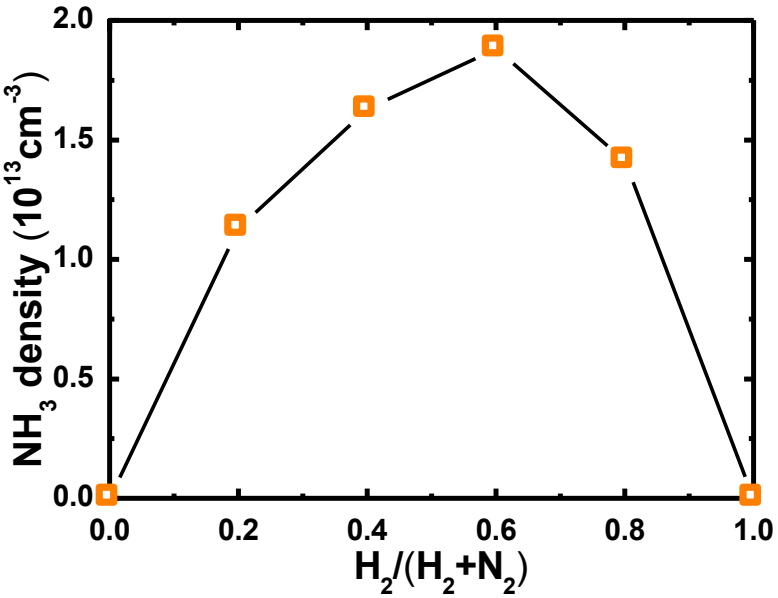

Figure 3.15 NH_3 absolute densities at remote region of 180 mm from the radical source as a function of a mixture ratio of N_2 and H_2.

3.4 Summary

The behavior of absolute density of N radical was investigated to optimized structure of source, when changing the structure of rf coil electrode and introducing the external magnetic. In the CRS mounted VUVAS chamber, the density for N radical was measured around 2.2×10^{11} atoms cm^{-3}. As described later, after optimizing the configuration of the in house source, the density of N radical from the HDRS was measured around 2.3×10^{12} atoms cm^{-3}.

The absolute densities of H and N radicals together with NH_3 molecules were measured in the remote region of the radical source by VUVAS and QMS. The absolute density of N atoms at the remote region was on the order of 10^{13} atoms cm^{-3}. The author found that N atom density was influenced considerably by the experimental history. After applying H_2-containing plasma discharges, N radical density was unstable since residual hydrogen possibly affected the dissociations of N_2. Additionally, the surface loss probability of the N radicals on PBN could influence N density at the remote region of the radical source under a pressure of about 1 Pa. The absolute density of NH_3 on the order of 10^{13} molecules cm^{-3} was evaluated at the remote region in the H_2 and N_2 mixture gas discharges, since the dominant mechanism for NH_3 generation is considered to be the surface reactions inside the PBN discharge tube owing to the large surface ratio over the volume. Noticeably, to determine the remote densities of N, H, and NH_3, the surface conditions on the PBN discharge tube and the configuration of surface to volume ratio is the crucially important parameters.

3.5 Reference

[1] M. Mesrine, N. Grandjean, and J. Massies: Appl. Phys. Lett. **72** (1998) 350.

[2] H. Amano, N. Sawaki, I. Akasaki, and Y. Toyoda: Appl. Phys. Lett. **48** (1986) 353.

[3] H. P. Maruska and J. J. Tietjen: Appl. Phys. Lett. **15** (1969) 327.

[4] M. Hori, K. Kano, T. Yamaguchi, Y. Saito, T. Araki, Y. Nanishi, N. Teraguchi, and A. Suzuki: Phys. Stat. Solid. B **234** (2002) 750.

[5] H. Komaki, R. Katayama, K. Onabe, M. Ozeki, and T. Ikari: J. Cryst. Growth **305** (2007) 12.

[6] K. Kushi, H. Sasamoto, D. Sugihara, S. Nakamura, A. Kikuchi, and K. Kishino: Mater. Sci. Eng. B **59** (1999) 65.

[7] W. C. Hughes, W. H. Rowland Jr., M. A. L. Johnson, S. Fujita, J. W. Cook Jr., J. Ren, and J. A. Edmond: J. Vac. Sci. Technol. B **13** (1995) 1571.

[8] M. Tabbal, M. Kazopoulo, T. Christidis, and S. Isber: Appl. Phys. Lett. **78** (2001) 2131.

[9] M. Nic, J. Jirat, and B. Kosata: *Bond dissociation energy*, online edition (IUPAC Compendium of Chemical Terminology, 2006).

[10] J. Osaka, M. S. Kumar, H. Toyoda, T. Ishijima, H. Sugai, and T. Mizutani: Appl. Phys. Lett. **90** (2007) 172114.

[11] T. Czerwiec, F. Greer, and D. B. Graves: J. Phys. D: Appl. Phys. **38** (2005) 4278.

[12] S. Meikle, and Y. Hatanaka: Appl. Phys. Lett. **54** (1989) 1648.

[13] S. Tada, S. Takashima, M. Ito, M. Hori, T. Goto, and Y. Sakamoto: J. Appl. Phys. **88** (2000) 1756.

[14] S. Takashima, S. Arai1, M. Hori, T. Goto, A. Kono, M. Ito, and K. Yoneda: J. Vac. Sci. Technol. A **19** (2001) 599.

[15] S. Chen, H. Kondo, K. Ishikawa, K. Takeda, M. Sekine, H. Kano, S. Den, and M. Hori: Jpn. J. Appl. Phys. **50** (2011) 01AE03.

[16] M. A. Lieberman and A. J. Lichtenberg: Principles of Plasma Discharges and Materials Processing (Wiley, New Jersey, 2005).

[17] G. P. Davis and R. A. Gottscho: J. Appl. Phys. 54 (1983) 3080.

[18] V. M. Donnelly and M. V. Malyshev: Appl. Phys. Lett. 77 (2000) 2467.

[19] K. P. Huber and G. Herzberg: *Molecular spectra and molecular structure 1: Constants of diatomic molecules* (New York: Van Nostrand Reinhold), p. 421.

[20] Y. Ono, Y. Hakamata, and T. Sato: J. Vac. Sci. Technol. A 7 (1989) 2784.

[21] H. Tang and J. B. Webb: Appl. Phys. Lett. 74 (1999) 2373.

[22] N.-E. Lee, R. C. Powell, Y.-W. Kim, and J. E. Greene: J. Vac. Sci. Technol. A 13 (1995) 2293.

[23] R. Held, D. E. Crawford, A. M. Johnson, A. M. Dabiran, and P. I. Cohen: J. Electron. Mater. 26 (1997) 272.

[24] Z. Yu, S. L. Buczkowski, N. C. Giles, T. H. Myers, and M. R. Richards-Babb: Appl. Phys. Lett. 69 (1996) 2731.

[25] T. H. Myers, L. S. Hirsch, L. T. Romano, and M. R. Richards-Babb: J. Vac. Sci. Technol. B 16 (1998) 2261.

[26] J. Amorim, G. Baravian, and A. Ricard: Plasma Chem. Plasma Process. 15 (1995) 721.

[27] A. Garscadden and R. Nagpal: Plasma Sources Sci. Technol. 4 (1995) 268.

[28] J. Loureiro and A. Ricard: J. Phys. D 26 (1993) 163.

[29] J. H. van Helden, W. Wagemans, G. Yagci, R.A. B. Zijlmans, D.C. Schram, R. Engeln, G. Lombardi, G. D. Stancu, and J. Ropcke: J. Appl. Phys. 101 (2007) 043305.

[30] S. F. Adams and T. A. Miller: Plasma Sources Sci. Technol. **9** (2000) 248.

[31] J. Amorim, G. Baravian, and G. Sultan: Appl. Phys. Lett. **68** (1996) 1915.

[32] S. Takashima, K. Takeda, S. Kato, M. Hiramatsu, and M. Hori: Jpn. J.Appl. Phys. **49** (2010) 076101.

[33] B. Gordiets, C. M. Ferreira, M. J. Pinheiro, and A. Ricard: Plasma SourcesSci. Technol. **7** (1998) 379.

[34] C. S. Moon, K. Takeda, S. Takashima, M. Sekine, Y. Setsuhara, M.Shiratani, and M. Hori: J. Vac. Sci. Technol. B **28** (2010) L17.

[35] C. S. Moon, K. Takeda, S. Takashima, M. Sekine, Y. Setsuhara, M.Shiratani, and M. Hori: J. Appl. Phys. **107** (2010) 103310.

Chapter 4

High Density Radical Source Assisted Molecular Beam Epitaxy

4.1 Purpose

The growth rate in GaN homoepitaxy by radio-frequency plasma-assisted molecular beam epitaxy layers (RF PA-MBE) is considered to be limited by supply of the nitrogen atomic radical. It is very difficult to break nitrogen molecular up into atoms to be incorporated in III-V nitrides compounds because of the high bond energy of the molecule of as large as 9.5 eV [1]. However, the absolute density of the radicals has not been well examined. In this study, a high-density radical source (HDRS) was developed as the nitrogen source for the PA-MBE system and the absolute density was measured by vacuum ultraviolet absorption spectroscopy (VUVAS) [2, 3]. A conventional radical source (CRS) and HDRS were set in the MBE chamber which is evacuated by a cryo pump and the distance between radical cells and substrates are almost the same for the both radical sources. N_2 flow rate dependence of absolute nitrogen radical density was shown in Fig. 4.1 for CRS and HDRS. To realize a high growth rate for GaN films, the homoepitaxial growth of GaN by PA-MBE with the HDRS was performed and confirmed to be faster than the growth of the GaN epitaxy layers with a conventional radical source (CRS) by almost a factor of three.

4.2 Homoepitaxial growth of GaN

A GaN template of 1μm thickness with a molybdenum back coating was prepared for the homoepitaxial growth of GaN by PA-MBE. To examine the maximum growth rate in GaN homoepitaxy using the CRS, growth conditions such as Ga flux (beam equivalent pressure: BEP) and substrate temperature were adjusted while observing the reflection high-energy electron diffraction (RHEED) pattern. A maximum growth rate of 0.5μm/h was obtained at a Ga flux of 2.0×10^{-4} Pa. The volume of the Ga flux was defined as the standard volume of the flux.

To study the effect of Ga flux on the growth rate, the flux was varied from 1.3×10^{-4} to 2.6×10^{-4} Pa for the CRS and from 2.6×10^{-4} to 1.2×10^{-3} Pa for the HDRS. These fluxes are 0.7 to 1.3 times and 1.3 to 4 times higher, respectively, than the standard volume of the flux. N_2 flow rates of 1 and 15 sccm were used for the CRS and the HDRS, respectively. The growth chamber pressure, during the growths was 1.3×10^{-3} P for the CRS and 2.6×10^{-2} Pa for the HDRS. Because of a requirement of higher flow rate of the nitrogen for HDRS, the growth chamber pressure was almost one order of magnitude higher than that of the pressure when using the CRS. The substrate temperature of 840 °C measured with a thermocouple and the growth time of 1 hour were fixed for all experiments. During the growth, RHEED patterns were observed to determine the growth modes of the epitaxy layers. After the growth, the thicknesses of the epitaxy layers were measured using a surface profiler (DekTak, Bruker AXS) and the surface morphology of the epitaxy layers was evaluated by Normarsky optical microscopy and atomic force microscopy (AFM) observation.

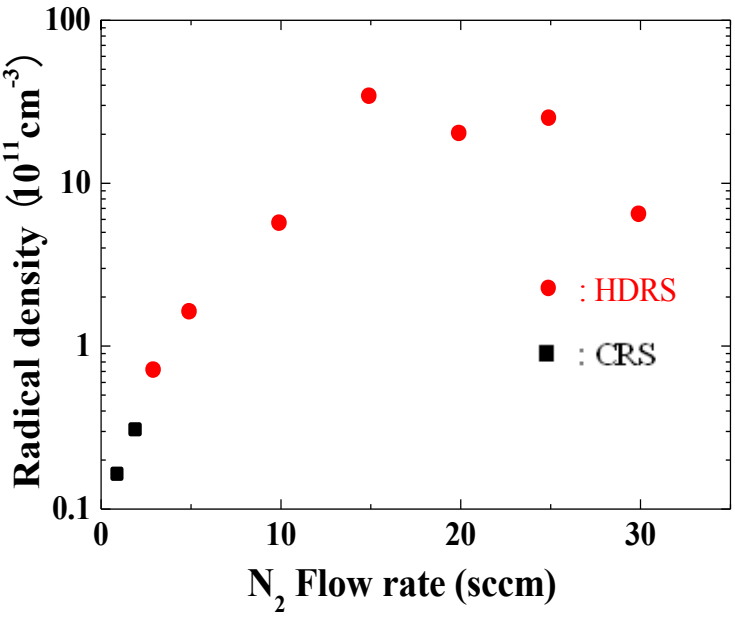

Figure 4.1 N_2 flow rate dependence of absolute nitrogen radical density measured by VUVAS.

Figure 4.2 shows the Ga flux dependence of the growth rates of the epitaxy layers obtained using the CRS and HDRS. Using the CRS, the maximum growth rate of epitaxy layers was confirmed when the Ga flux was set to 2.0×10^{-4} Pa. When the Ga flux was increased to 2.6×10^{-4} Pa, Ga droplets were observed on the epitaxial layers, indicating an insufficient supply of nitrogen radicals. Using the HDRS, a growth rate of 1400 nm/h, which is almost three times higher than that obtained with the CRS, was achieved when the Ga flux was set to 5.2×10^{-4} Pa. This result is clear evidence of the much large supply of nitrogen radicals using the HDRS. During the growth, a streak RHEED pattern was unchanged, indicating a step flow growth mode, as shown in Fig. 4.3.

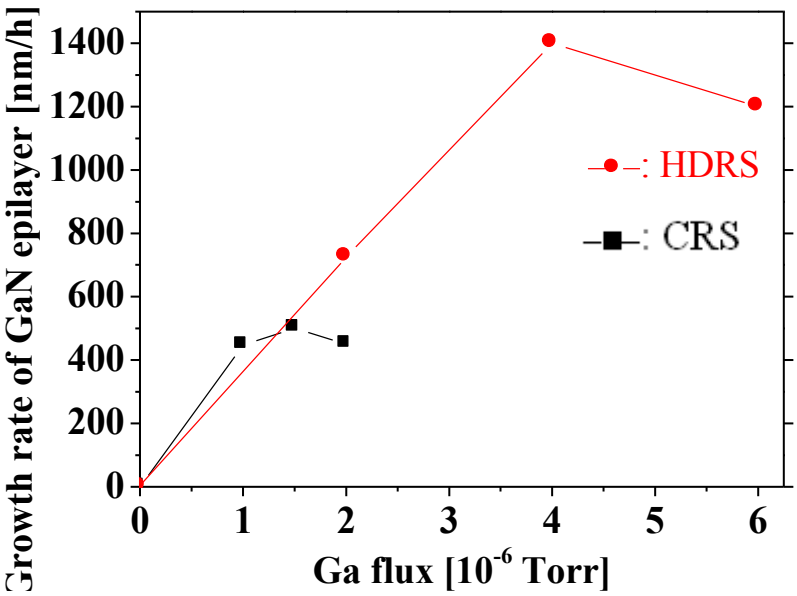

Figure 4.2 Ga flux dependence of growth rates of epilayers obtained using CRS and HDRS.

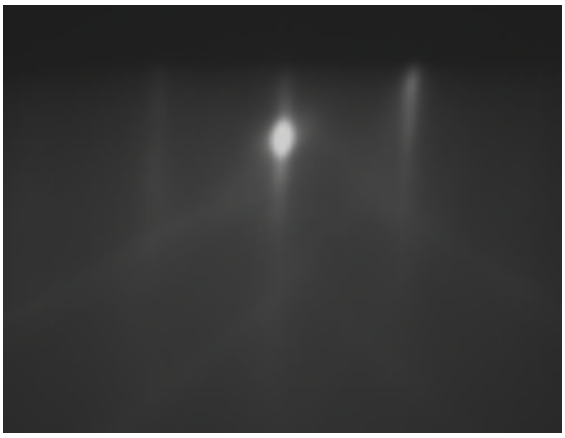

Figure 4.3 RHEED pattern of epilayer grown by PA-MBE with HDRS at maximum growth rate of epilayer. The incident angle of the electron beam was perpendicular to the <1120> direction. This image was taken 5 min after starting the growth.

Figure 4.4 shows the results of the Normarsky optical microscopy observation of epitaxial layers obtained using the (a) CRS and (b) HDRS at the maximum growth rate. A smooth surface of the epitaxial layers without Ga droplets was confirmed with both radical sources. On the basis of the observation of streak patterns of RHEED, it is considered that these growths occur under stoichiometric growth conditions. Fig. 4.5 shows the results of the AFM observations of epitaxial layers using the (a) CRS and (b) HDRS at the maximum growth rate of the epitaxial layers. Root-mean-square (RMS) roughness of 3.70 nm for the CRS and 1.25 nm for the HDRS were measured. Although an almost 3 time faster growth rate was realized by using the HDRS, the superior surface morphology of the epitaxy layers was confirmed. Faster growth may result in an improved surface morphology of the epitaxy layers.

In this study, almost 3 times faster growth rate of the GaN homoepitaxy by using HDRS was obtained with the confirmation of approximately 100 times higher radical density compared with that of the CRS. In a previous study, faster growth rate of GaN by the PA-MBE have been reported [5, 6]. One of the reasons why the maximum growth rate is not as high as it is expected from the radical density is thought to be the higher chamber pressure due to the limitation of the pumping speed of our cryo-pump. The chamber pressure during operation of HDRS is five times higher than that of CRS. The higher chamber pressure might not be preferable to the faster growth rate of the epitaxy.

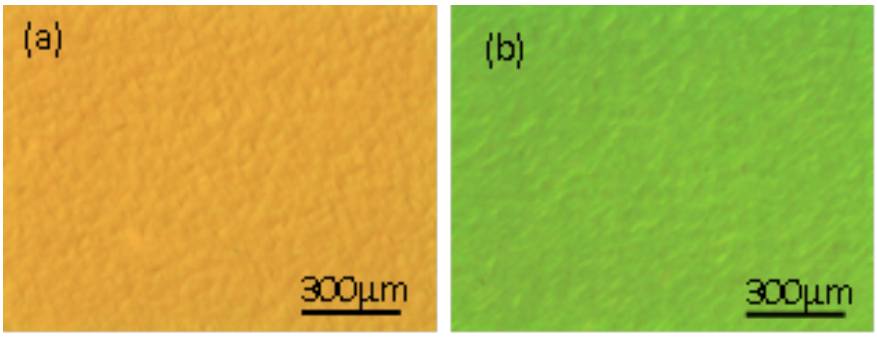

Figure 4.4 Images of Normarsky optical microscopy observation of epilayers using (a) CRS and (b) HDRS at each maximum growth rate of condition.

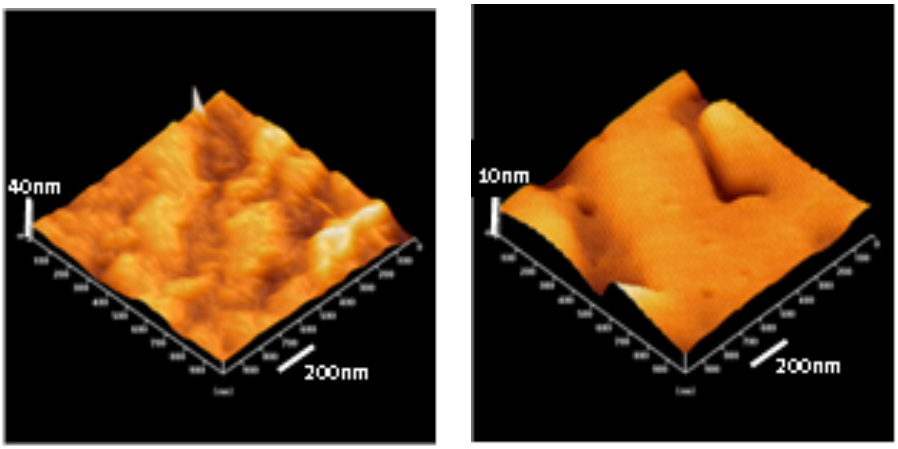

(a) (b)

Figure 4.5 Images of AFM observations of epitaxy layers using (a) CRS and (b) HDRS at maximum growth rate epitaxy layers. The RMS roughnesses were (a) 3.70 nm and (b) 1.25 nm. The observation area was 1 μm^2.

4.3 Heteroepitaxial growth of InGaN

The InGaN growth was also performed in MBE. A 3.5 μm-thick GaN film of on 2-inch sapphire substrate with a molybdenum back coating was prepared for the heteroepitaxial growth of InGaN. The details of structural property of InGaN films have been published [7]. N_2 flow rates of 1 and 15 sccm were used for the CRS and the HDRS, respectively. The work pressure, during the growths, was 1.0×10^{-3} Pa for the CRS and 2.0×10^{-2} Pa for the HDRS. The substrate temperature of 675^{o}C measured with a thermocouple and the growth time of 1 hour were fixed for all experiments. To vary InN molar fraction of the InGaN films, the III/III ratios of metal precursor, gallium (Ga) and indium (In), were varied from 0.30 to 0.41.After the growth, the thicknesses of the epitaxial layers are measured using a surface profiler (Dektak, Bruker AXS). InN molar fraction of the InGaN films was estimated by 2 theta-omega scan of XRD and the crystalline properties were analyzed by X-ray omega-rocking curve (XRC) measurement.

The growth rate of GaN homoepilayer using HDRS of 1.4μm/h, which is almost three times faster growth rate with atomically smooth surface was obtained. This result was a clear evidence of the large supply density of nitrogen radicals using the HDRS. In this study, we further examined the efficiency of the HDRS by growing the InGaN heteroepilayer on GaN substrates. Not only the growth rate, but also the crystalline property of heteroepitaxy InGaN films by using the HDRS and CRS were evaluated. Growth conditions such as Ga flux and substrate temperature were adjusted while observing the reflection high-energy electron diffraction pattern. The surface morphology was confirmed by atomic force microscopy to make sure the maximum Ga flux without droplet on the surface of films. In the case of CRS, the maximum growth rate of epitaxial layers is confirmed when the total amount of metal flux of Ga and In is

set to 3.0×10^{-2} Pa. In the case of growth using HDRS, a growth rate of 1.4 μm/h, which is almost three times higher than that obtained with the CRS, is achieved when the total amount of metal flux is set to 8.9×10^{-2} Pa. Approximately three times larger supply the total amount of metal flux is matched to almost three times faster growth rate in comparison of the HDRS and the CRS. The highest n_N in optimized is around 2.3×10^{12} atoms cm^{-3} (3.2×10^{-8} $mol \cdot cm^{-2} \cdot s^{-1}$) at nitrogen flow rate of 15 sccm. Even the actual n_N in MBE chamber is still unclear, it should be lower than the value, which was measured in VUVAS chamber since the work pressure are three orders higher than the MBE chamber.

The profiles of XRC for (0002) plane diffraction of CRS and HDRS with different InN molar fraction are shown in Fig. 4.6 (a) and (b), respectively. Much sharper curves can be confirmed in the case of growth using HDRS, suggesting that the crystalline property is improved in condition involving high density radical. The details of full width half maximum (FWHM) for two sources are plotted in Fig. 4.7. It clearly points out the HDRS can achieve higher quality InGaN films compare to CRS, especially in higher InN molar fraction. It has been reported the GaN film quality was correlated with nitrogen plasma, which could generate much larger fraction of atomic nitrogen and 1st-positive series excited molecular nitrogen [8]. However, the mechanism of highly crystalline achieved in the high density radical condition is even unknown. The super lattice structure may be one of the reasons [7], which need to be further investigated.

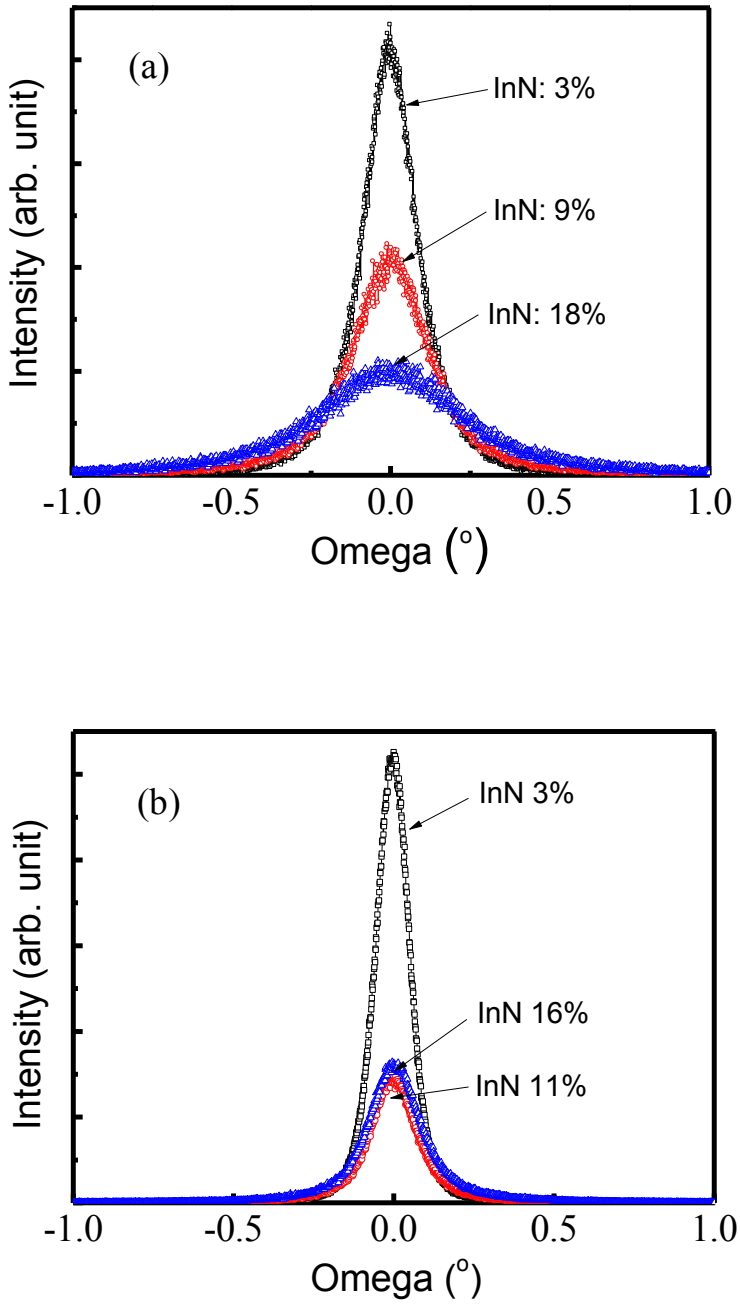

Figure 4.6 XRC profiles for (0002) plane diffraction of (a) CRS and (b) HDRS in different fraction of In.

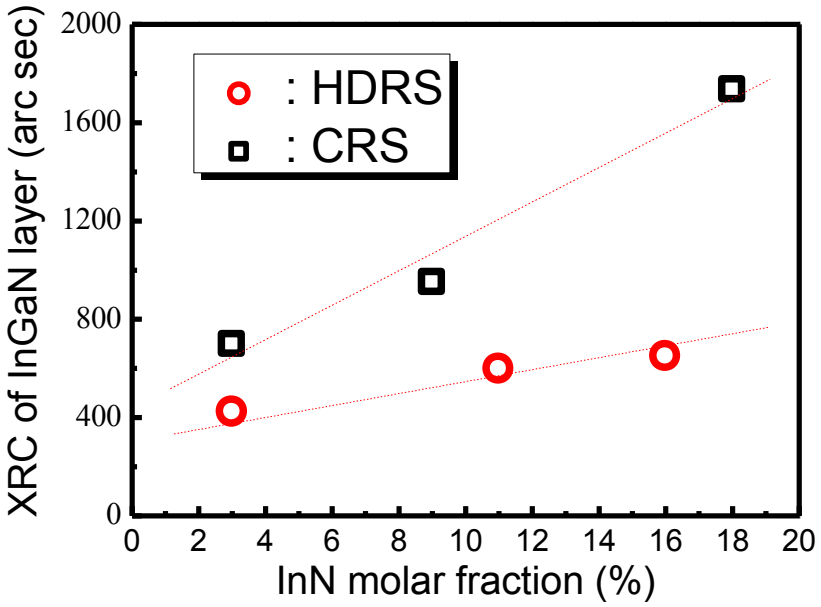

Figure 4.7 Full width height maximum of CRS and HDRS in different fraction of In.

4.4 Summary

A high-density radical source for an RF PA-MBE system was developed to realize a high growth rate for GaN film. A high growth rate of 1.4μm/h was achieved with an atomically smooth surface for the epitaxy layer grown by RF PA-MBE using the HDRS. The growth rate was almost a factor of three higher than that in the case of using the CRS. A high growth rate of 1.4μm/h was also achieved for the heteroepilayer of InGaN grown using the HDRS. The growth rate was almost three times higher than that in the case of using the CRS of 0.5μm/h. Notably, the crystalline property was greatly improved, which confirmed by XRC profile for (0002) plane diffraction in the films with InN molar fraction of 3 to 18 %. The FWHM of XRC was decreased from 1400 to 600 arc sec at InN molar fraction around 17 %.

4.5 Reference

[1] Z. Yang, L. K. Li, and W. I. Wan, Appl. Phys. Lett. **67**, 1686 (1995).

[2] S. Chen, H. Kano, S. Den, K. Takeda, S. Takashima, M. Sekine, and M. Hori, Extended Abstract of AVS 56th International Symposium and Exhibition (2009), p. 112.

[3] S. Takashima, S. Arai, M. Hori, T. Goto, A. Kono, M. Ito, and K. Yoneda, J. Vac. Sci. Technol. A **19**, 599 (2001).

[4] S. Chen, H. Kondo, K. Ishikawa, K. Takeda, M. Sekine, H. Kano, S. Den, and M. Hori, Jpn. J. Appl. Phys. **50**, 01AE03 (2011).

[5] D. Sugihara, A. Kikuchi, K. Kusakabe, S. Nakamura, Y. Toyoura, T. Yamada, and K. Kishino, Phys. Status Solidi A **176**, 323 (1999).

[6] K. Kushi, H. Sasamoto, D. Sugihara, S. Nakamura, A. Kikuchi, and K. Kishino, Mater. Sci. Eng. B **59** (1999) 65.

[7] Z. H. Wu, Y. Kawai, Y.-Y. Fang, C. Q. Chen, H. Kondo, M. Hori, Y. Honda, M. Yamaguchi, and H. Amano: Appl. Phys. Lett. **98** (2011) 141905.

[8] W.C.Hughes, W. H. Rowland, Jr., M. A. L. Johnson, Shizuo Fujita, J. W. Cook, Jr., J. Ren, and J. A. Edmond.: J. Vac. Sci. Technol. B **13**(4), Jul/Aug (1995).

Chapter 5

Hydrogen Radical Passivation of Plasma Etched GaN at Room Temperature

5.1 Purpose

Patterning of GaN by wet chemical etching is difficult because of the material's high mechanical strength, stability at high temperatures as well as chemical inertness. Thus, a wide range of GaN-based photonic and electronic devices have been fabricated by using dry etching, typically high-density plasmas are utilized to achieve a high etching rate and produce anisotropic features [1, 2]. However, the plasma-induced defects and surface residues that remain after such processes limit their use in the fabrication of highly reliable devices [3, 4] as they tend to degrade the optical [5] and electrical properties (e.g., as exhibited by an increase in leakage current and a decrease in break down voltage of diodes [6, 7]). Therefore, there is a strong demand to develop post-etching processes that eliminate such defects and residues.

Previously, post-etching processes such as thermal annealing or plasma treatment have been performed on plasma-damaged GaN. Cao *et al.* have found that rapid thermal annealing of plasma etched GaN recovers its electrical properties as demonstrated by the current voltage characteristics of Schottky diodes [8]. High-temperature annealing might, however, lead to the preferential removal of N atoms from the GaN surfaces. Lee *et al.* have reported that N_2 plasma treatment improves the PL characteristics of heavily damaged GaN surfaces [9]. However, the lattice defects

created by energetic nitrogen ion bombardment lead to unstable bonding states for the N atoms. Generally, usage of atomic species with high chemical activity can avoid the formation of defects induced by energetic ion [10]. Yoo *et al.* applied H_2 plasma to gallium arsenide after plasma etching and found that H_2 plasma treatment could passivate the defects [11]. In a previous study, the author has reported that exposure of GaN to atomic nitrogen after Cl_2 plasma etching removes chloride residues without generation of point defects in the GaN films while sufficiently passivating Cl_2 plasma-induced defects [12]. In the case of Si, the author has also reported that H radical exposure at room temperature passivates deep-level defects in plasma-damaged Si [13]. This passivation is considered to result from termination of plasma-induced dangling bonds by H radicals. In contrast, it has been widely recognized that surface oxidation can easily occur on plasma-damaged GaN [14]. Hence, in order to prevent contamination of damaged surfaces from exposure to air, it is essential to carry out post-etching processes *in-situ*.

5.2 Hydrogen radical passivation

Plasma-damaged GaN is exposure to *in-situ* H radical at room temperature. The optical, stoichiometric, and morphological properties of the GaN obtained after varying doses of H radicals were evaluated by PL, *in-situ* XPS, and atomic force microscopy (AFM), respectively.

5.2.1 Experiment

Figure 5.1 shows a schematic of the experimental system. The system has two chambers. The left chamber is used for plasma-beam etching and the right chamber is used for radical exposure. In the plasma-beam chamber, radio-frequency (rf) power at a frequency of 13.56 MHz is applied to a low-inductance antenna [13] to generate Cl_2 plasma. Ions are then extracted from the plasma using an ion optics system, where the each electrode has eight holes with 0.7 mm diameter. These fine beams are broadened toward the process region and relatively uniform beam profile is obtained for 10 mm diameter area on the sample. The ion energy and flux can be controlled by varying the voltages of the acceleration, extraction, and focusing lenses. Although the Cl radicals were able to diffuse through the hole at the lens into the process region, electrons were reflected by the acceleration lens, which has a negative potential. A Faraday cup was placed in the process region where the sample is set at a position 50 mm from the focusing lens to measure the incident ion current to the GaN. Typical pressures of the plasma and process regions were about 1 and 6×10^{-3} Pa, respectively. The radical exposure chamber was equipped with a high-density radical source, which has been developed by our group, with a radical density one order of magnitude higher than those of conventional sources [16]. The absolute density of ground state H radicals at the sample position was measured by vacuum ultraviolet absorption spectroscopy [17]. Although both ground- and excited-state H radicals irradiate the sample, the author

considers that the H radicals in the ground-state are the most effective species in the reaction due to their long lifetime. The H radical density (n_H) at the sample was measured to be 1×10^{12} atoms cm^{-3} at a work pressure of about 1 Pa. The H radical flux at the sample surface Γ_H was calculated using [18]

$$\Gamma_H = \frac{1}{4} n_H \sqrt{\frac{8kT}{\pi m}} \quad , \qquad (5.1)$$

where k is the Boltzmann constant, T is the radical temperature (assumed to be 300 K), and m is the atomic mass of H atom. The radical temperature may have a larger value than 300 K, since the energy transfer between PBN tube and hydrogen occurred at the hole of aperture. On the other hand, the surface recombination at stainless steel made recovery chamber may decrease the temperature of radical. However, from the eqs. 5.1, the radical flux is a function of the square root of gas temperature. It means the value of radical flux will not be sensitively changed by gas temperature. Overall, the error of radical flux estimated by eqs. 5.1 should be acceptable.

In order to eliminate the injection of charged species (ions and electrons) by diffusion from the plasma though the aperture to the sample, a parallel deflector was mounted at the exit of the source. With this deflector, the ion flux measured by a Faraday cup at the sample position was less than 10^{10} ions cm^{-2}, which were six orders of magnitude lower than that observed with inductively coupled hydrogen plasma (where the sample was directly placed into the plasma).

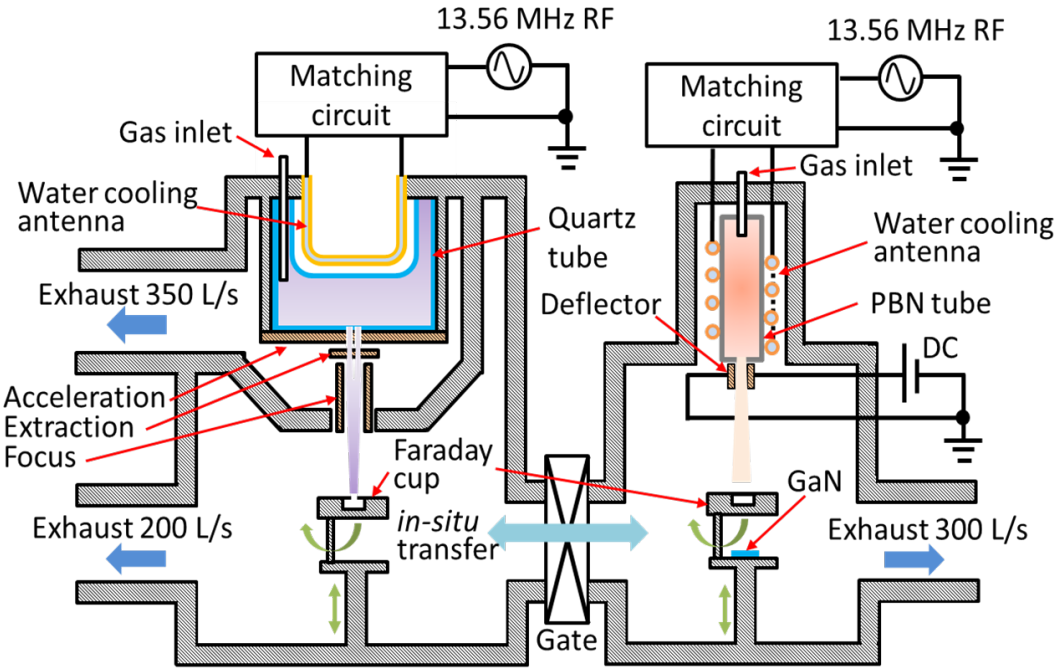

Figure.5.1 Experimental setup of plasma beam and radical passivation system.

In this study, the author used 10^{17} atoms cm^{-3} Si doped 2-μm-thick n-GaN films, which were grown by metal-organic chemical vapor deposition on a sapphire substrate with a pre-deposited 25-nm-thick non-doped buffer layer. Prior to etching, samples were cleaned by dipping into 2% hydrofluoric acid for 1 min and then immersed in 17.5% hydrochloric acid for 1 min to remove native oxides and metallic contaminants, respectively. All the samples were then irradiated by a chlorine plasma-beam with ion energy of 100 eV at a dose of 5×10^{16} ions cm^{-2}. After etching, the samples were transferred to the radical exposure chamber under ultrahigh vacuum and exposed to H radicals at room temperature with one of three doses: 0.4, 1.9, or 3.8×10^{17} atoms cm^{-2}.

The optical properties of the samples were evaluated by microscopic-PL (μ-PL) using 325 nm wavelength light from a He-Cd laser with an illumination area of 1 μm^2. A Mg Kα X-ray (1253.6 eV) source was used for XPS measurements (ULVAC-PHI, XPS 1600). The photoelectron take-off angle was 90°. Peaks were recorded at 19.9 eV for Ga 3d, 397.0 eV for N 1s, 201.0 eV for Cl 2p, and 531.0 eV for O 1s, and elemental compositions were calculated based on the inelastic mean free path and a relative sensitivity factor. The surface morphology was observed using AFM (Veeco, Nano Man VS-1N) with a SiN cantilever in tapping mode. It is well known that the PL intensity is not only affected by defects in the crystal but also surface roughness. Thus, we carefully prepared the samples by controlling the Cl ion dose and observed the morphology of the surface by AFM. The root mean-square roughness of the etched sample was approximately 0.6 nm in a 10×10 μm^2 image, which is the same as that for an as-grown sample. This indicates that the influence of roughness on the PL results could be ignored in comparing between the PL results of the as-grown and etched samples.

5.2.2 Intensity of band-edge emission

Figure 5.2 depicts the PL intensity of the band-edge emission (I_{BE}) (photon energy: 3.43 eV), which is normalized to the value of the as-grown sample, as a function of H radical dose. I_{BE} significantly decreased upon Cl_2 plasma-beam etching (zero point of the H radical dose axis) to 10% of as-grown's due to the non-stoichiometric surface, i.e., point and line defects induced by ion bombardment and deposition of etching residues on the surface. It is well known that low-energy ion bombardment can produce a high defect density. Defects such as V_N, interstitials, and antisites may act as deep-level traps and capture conduction electrons [19]. Some reseach groups have also reported the existence of plasma etching-induced deep-level traps which act as non-radiative recombination centers and reduce band-edge emission [20, 21].

With exposure of the plasma-damaged GaN to H radicals, the PL intensity increased with increasing dose of H radicals and recovered to approximately 90% of the initial value at a dose of 3.8×10^{17} atoms cm^{-2}. It is considered that both termination of the dangling bonds by H and vaporization of the surface residues occurred. It is difficult to quantify the contribution of each factor at this time. However, the increase in I_{BE} at a dose of 0.4×10^{17} atoms cm^{-2} was significantly higher than those observed at doses of 1.9 and 3.8×10^{17} atoms cm^{-2}, which mitght indicate that the optical properties were very sensitive to any residues that remain after plasma etching, which was also confirmed by XPS.

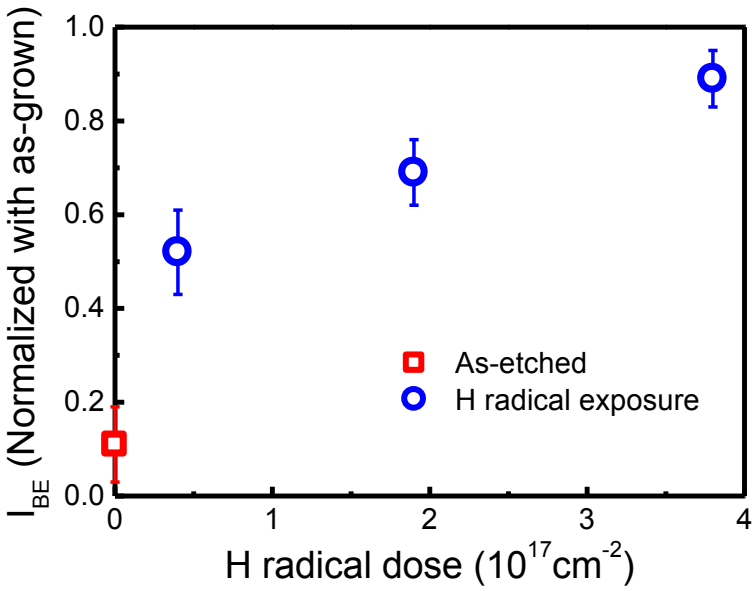

Figure 5.2 PL intensity of band-edge emission as a function of hydrogen radical dose (Intensity normalized by as-grown sample).

5.2.3 Surface stoichiometry

Figure 5.3 depicts the elemental composition of a GaN surface for as-grown, as-etched, and after H radical exposure at a dose of 0.4×10^{17} atoms cm^{-2} (no further changes could be observed for larger dose samples). After etching, the Ga content decreased from 50 to 42% and the N content decreased from 42 to 16%. The N/Ga ratio decreased from 84 to 38%, which suggested that the N atoms were preferentially removed probably through the formation of high vapor-pressure etching products such as N_2 and NCl_3 during the etching, leading to Ga-rich surfaces with an abundance of dangling bonds. Notably, the Cl content was significantly increased from 0 to 23 %, suggesting that etching residues might be deposited on the surface. After H radical annealing at a dose of 0.4×10^{17} cm^{-2}, the Ga content remained almost constant, but the N content increased from 16 to 32 %, leading to an increase in the N/Ga ratio from 38 to 71 %. This increase indicates that the surfaces of Ga or residues containing Ga were removed by exposure to the H radicals. The Cl content decreased to 0%, suggesting that the H radicals might also desorb chloride residues from the surface by chemical reaction to form a high vapor-pressure product. This could also explain why I_{BE} recovered to such a remarkable extent at H radical dose of 0.4×10^{17} atoms cm^{-2}. The increase in oxygen content from 8 to 20% after etching might be due to the quartz chamber, which may emit oxygen radicals under sputtering by the etching plasma. In the present experimental setup, this problem cannot be avoided. However, no further oxidation was observed after *in-situ* H radical exposure. Hence, oxidation at the etching step will not affect the results of H radical passivation.

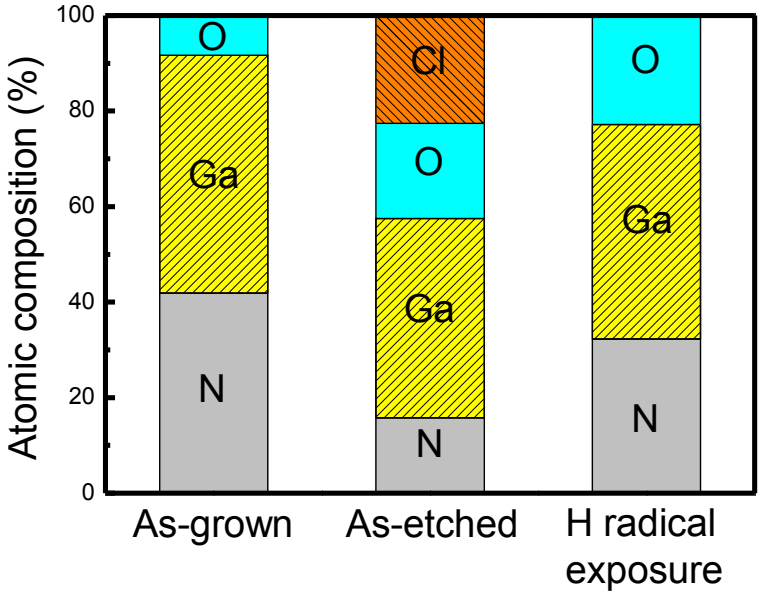

Figure 5.3 Atomic contents of N, Ga, and Cl for GaN samples, as-grown, as-etched and after H radical exposure, at a dose of 0.4×10^{17} atoms cm^{-2}.

To further explore the mechanism of H radical passivation, the narrow XPS spectra of Ga 3d were analyzed, and the results are shown in Fig. 5.4. In the spectra for the as-grown film, the peak at 19.9 eV was assigned to GaN bonds. No significant changes could be observed in the full width at half maximum (FWHM) of the peak or in the chemical shift between the as-grown and as-etched samples. This implies that the Ga-related complexes containing Ga-O and Ga-Cl bonds were not involved during etching. Notably, after *in-situ* H radical exposure, an additional peak at a lower binding energy of 18.3 eV, seen as a shoulder of the main peak, was found to increase with increasing H radical dose. It is difficult to assign this new peak to Ga-Ga, which has a binding energy at 18.2 eV. The author believes that this shoulder arises from Ga-H because hydrogen-related bonds often have relatively low formation energies. This energy is also consistent with the increment in band-edge emission expected for H radical termination of dangling bonds created by ion bombardment.

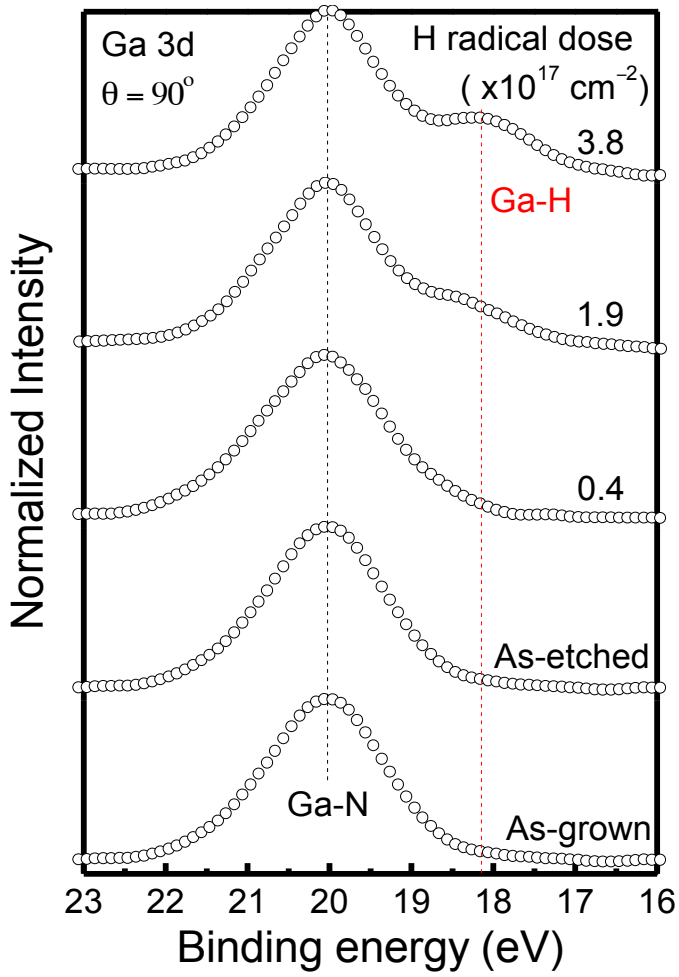

Figure 5.4 Ga 3d XPS spectra in a narrow region for GaN samples, as-grown, as-etched, and after H radical exposure, at doses of 0.4, 1.9, and 3.8 × 10^{17} atoms cm^{-2}.

The optical and stoichiometric properties of plasma-damaged n-GaN after exposure to H radicals at room temperature were investigated by PL and XPS. I_{BE} drastically decreased after Cl_2 plasma-beam etching due to point defects, mainly generated by ion bombardment at the surface as shown in Fig. 5.5 (a). After H radical exposure, I_{BE} increased with increasing radical dosage to almost reach the as-grown value. The H radicals terminate the dangling bonds of Ga on the GaN surface, as indicated by the Ga 3d XPS spectra, as well as desorption of surface residues as shown in Fig. 5.5 (b).

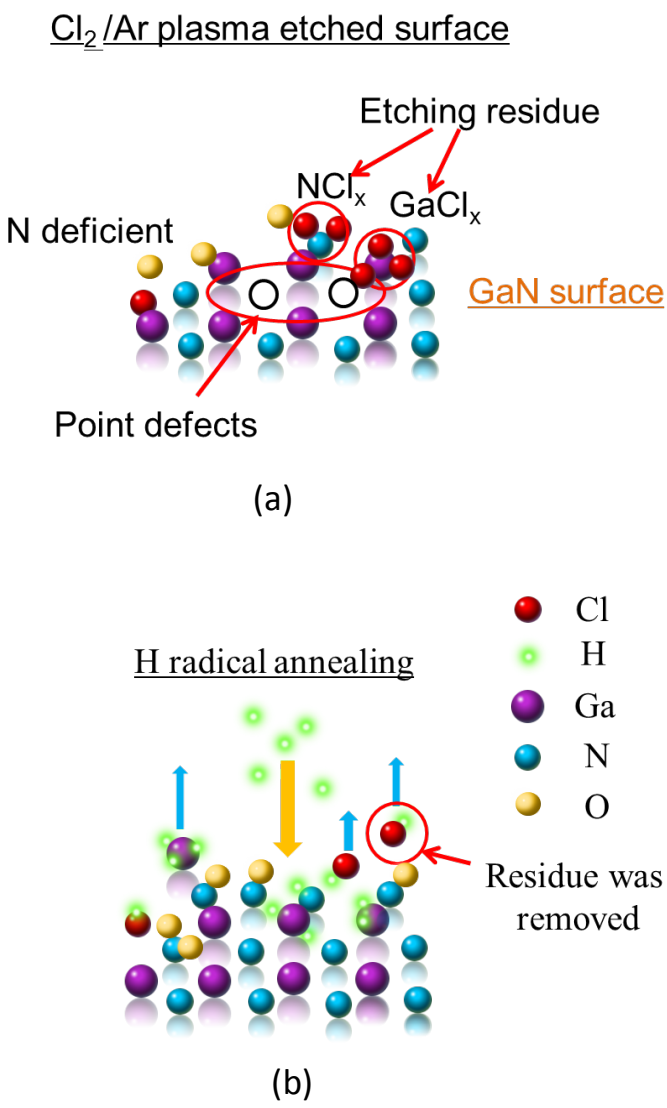

Figure 5.5 Interaction of (a) chlorine based etching plasma and (b) hydrogen radical to surface of GaN films.

5.3 Individual roles for atoms and ions during passivation

The exposure of atomic hydrogen (H) with a dosage of approximately 3.8×10^{17} atoms cm^{-2} s^{-1} at room temperature recovered the plasma-etched GaN surface was presented. However, in the aspect of the hydrogen (H_2) plasma exposure on the plasma-etched GaN, the individual roles for atoms and ions of hydrogen during the exposure have been still remained unclear.

In this section, individual roles of H and ions of hydrogen (H_n^+) in H_2 plasma for passivation of plasma-etching-damaged GaN will be explained. To control a ratio of fluxes for H and H_n^+ was carried out by deflecting the H_n^+ by applying an electric field. Photoluminescence property was evaluated, and surface stoichiometric composition was measured by the *in-situ* XPS. Through the experiments, the author discussed the individual roles of H and H_n^+ for passivation of the defects created by plasma etching.

5.3.1 Experiment

Samples were non-doped GaN films with a thickness of 5 μm grown on sapphire substrate by metal-organic chemical vapor deposition. Just after chemical cleaning, the samples were partially etched off by using inductively coupled plasma etcher (ULVAC CE-300IN) schematically shown in Fig. 5.6. A mixture gas of chlorine with a gas flow rate of 24 sccm and argon with that of 6 sccm was introduced, and a pressure was maintained at 1 Pa. A 13.56 MHz radio-frequency power of 200 W was applied to the antenna to sustain plasma discharges, and a 12.5 MHz power of 30 W was applied to the electro-statically-chucked stage as an electrically biasing to the substrate. Typically peak to peak bias voltage (V_{pp}) was approximate to 190 V. The roughly half voltage of the V_{pp} was regarded as ion bombardment energy [22], and GaN films were etched off

with an etching rate of around 75 nm/min. Etching periods was fixed for 1 min, and the GaN film with a thickness of 75 nm was partially etched off.

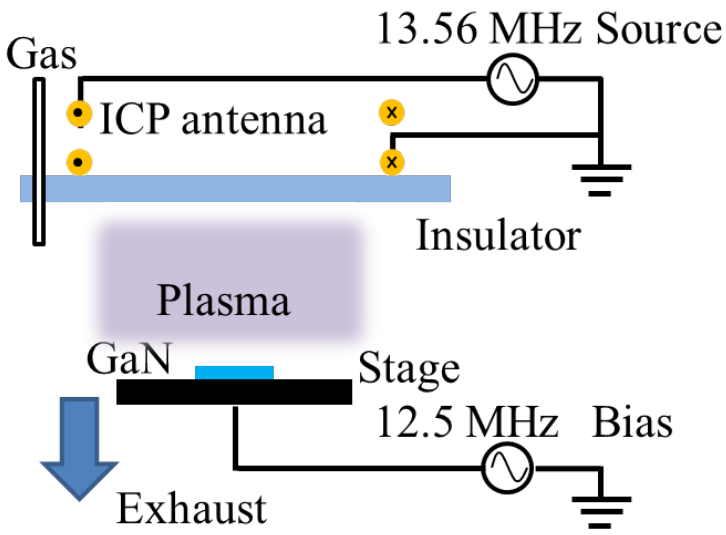

Figure 5.6 Schematic graph of ICP etching system.

After the plasma etching, the samples were subjected to passivation system and irradiated by both H and H_n^+ with individually controlled flux ratio. Figure 5.7 shows the schematic representation of passivation system. Both the H and H_n^+ were provided by high density hydrogen plasmas source. Hydrogen gas with a flow rate of 100 sccm and a pressure inside discharge tube was at 2 Pa. In front of exit aperture (with a diameter of 5 mm) of the source, a deflector for charged species was placed and applied direct current (dc) voltage oppositely to parallel-plate electrodes (a length of 10 mm) and a gap-distance between them was 10 mm. The sample position was distanced 200 mm from the aperture and ion currents at this position were measured by using a Faraday cup with a diameter of 5 mm and an ampere meter.

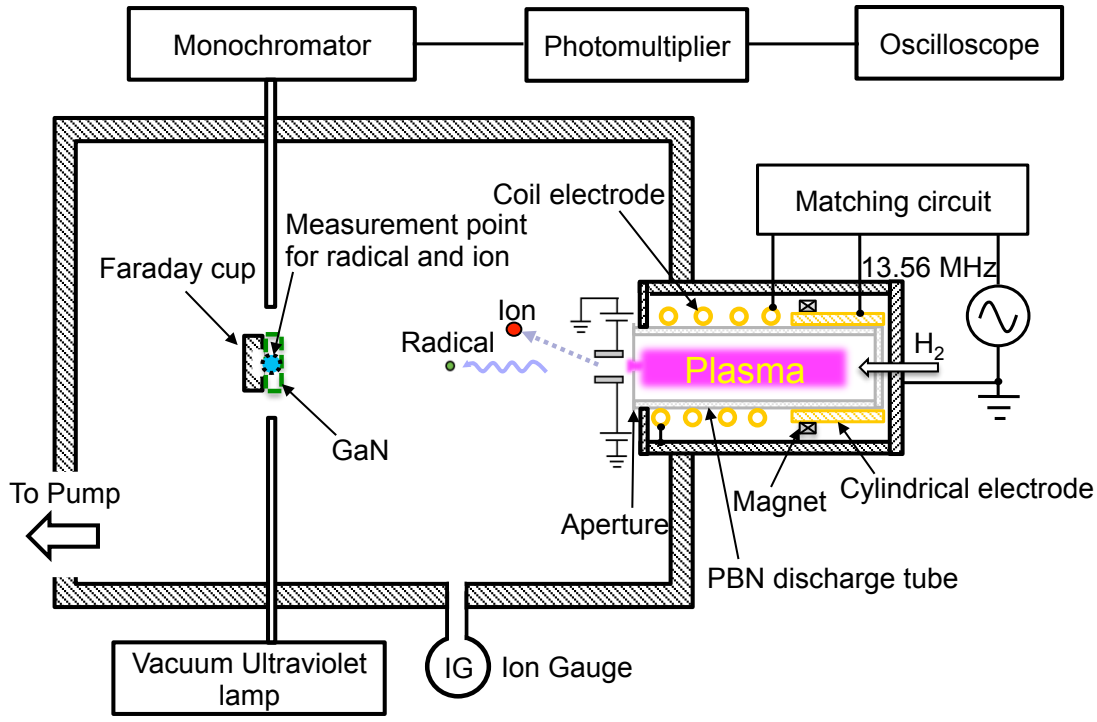

Figure 5.7 Schematic diagram of high density radical source and experimental setup.

The ion currents were exponentially decreased with increasing of the dc voltages of electrodes in the deflector. Figure 5.8 (a) shows the ion flux (Γ_i) calculated from the ion currents as a function of the deflecting voltages. Because of an ion-beam profile was regarded as Gaussian, the integrated ion flux over the areas for irradiation, ion currents as a function of deflecting voltages could be represented by the complementary error function as a fitting line shows in Fig. 5.8 (a). This agreed well with the experimental results.

Moreover, absolute densities of H, where at the sample position, were also measured by the vacuum ultraviolet absorption spectroscopy [23]. Nonetheless by changing the dc voltages, the density of H remained a constant of 2×10^{12} atoms cm^{-3}, which is shown in Fig. 5.8 (b). Therefore, radical fluxes (Γ_r) were almost kept a value of approximately 5×10^{14} atoms $cm^{-2}s^{-1}$. Consequently by changing the dc voltages, we could control the ratio of fluxes for H to H_n^+ (Γ_r/Γ_i), which was ranged from 300 for Γ_r/Γ_i at the dc voltage of 0 V to more than 17000 at that of 300 V.

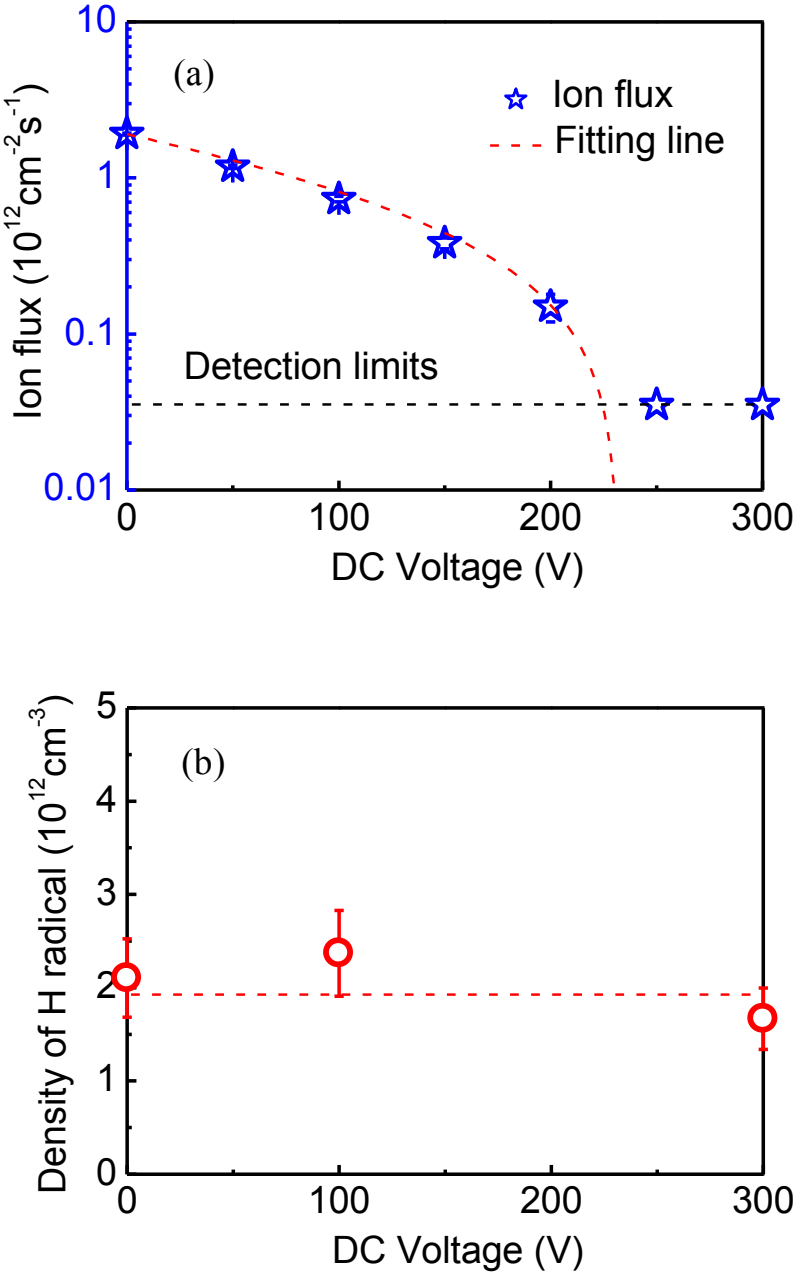

Figure 5.8 Ion fluxes (a) and H radical density (b) as a function of DC voltage at the position where GaN wafer was set for the hydrogen treatment with control individually a ratio of fluxes for ions and neutrals.

The samples were transported under ultra-high-vacuum ambient and the surface was analyzed by using *in-situ* XPS (ULVAC-PHI, XPS 1600) with an Mg-Kα X-ray source (1253.6 eV). Take-off angle of photoelectron was set to 15°. A narrow spectrum was recorded with a peak located at 19.9 eV for Ga 3d.

PL measurements using excitation of 325-nm-wavelength light from a He-Cd laser with an illuminating area of 1 μm^2 (a depth of roughly 100 nm for detection) were made at room temperature. Cathodoluminescence (CL) spectrometer, which is equipped on scanning electron microscope was used for taking spectra of luminescence from a square area of 8 × 8 μm^2 at low temperature around 100 K. This measurement provides detailed information about the defects and a depth profile when an energy for primary electrons changed by 2 and 5 keV (detection depths for 50 and 160 nm, respectively). For each sample, we compared intensities of band edge emission (I_{BE}) at around 3.47 eV from GaN films.

5.3.2 Intensity of band-edge emission

First, we reviewed the evaluation of properties for the damaged GaN film. In focus of the I_{BE}, values for the I_{BE} were normalized to be unity for that for as-grown GaN film. For as-etched GaN film, the I_{BE} decreased to a level of approximately 40% of as-grown film after the normalized representation as shown as dashed-line in Fig. 5.10. This indicated that high density of non-radiative defects or deep level defects were created by bombardments of argon and chlorine ions during plasma etching process [3]. Dominant cause of the I_{BE} decrease is the creation of defects of nitrogen vacancy V_N; other candidates are such as interstitials of Ga, and antisites replaced Ga by N and vice versa. Those defects act as both deep-level traps to capture electrons located at conduction bands act as a non-radiative recombination centers (NRR) and make the I_{BE} reduce [19-21]. Thus we believe that it is possible to explain a model for passivation by terminating defects such as V_N by H.

Previous experiments, for instance the condition of $\Gamma_r/\Gamma_i > 17000$ and a dosage for H of 3.8×10^{17} atoms cm^{-2}, revealed that plasma-beam damaged GaN films were passivated by H atoms and the I_{BE} was improved up to a level of around 90% for the as-grown GaN films [24]. We noted that no influence on the PL intensities was confirmed in those cases here because an amount of residues on the etched surface were to be small, however we knew that the residues should be usually taken into account for changes in the PL intensities since they influenced on optical property. In another aspect, we speculated that amounts of residues such as chlorides on etched surfaces affected to levels of recovery for the I_{BE}. We recognized a slight difference in recovery level of 85% for present case of plasma etching compared with that of 90% for the previous plasma-beams study. This difference might be resulted from large amount of surface residues. In other words, since the larger amount of surface residues was covered, so it

enhanced consumption of H reacting with the residues and then reduced in the recovery to enhance the required treatment period, that is not enough H dosage. Further study about effects of the surface residues is resent conducting.

Interestingly, the experimental results by controlling H_n^+ showed efficiency of recovery depended on values of the Γ_r/Γ_i as shown in Fig. 5.10. While keeping the Γ_r/Γ_i higher enough, the high value of I_{BE} was obtained. Especially, the improving of I_{BE} reached up to a level of 85% for the as-grown GaN films when the $\Gamma_r/\Gamma_i > 17000$ with a dosage for H of 3.8×10^{17} atoms cm^{-2}. The author noted that this dependence occurred even though identical expose to H. Thus the simultaneous irradiation of H_n^+ influenced clearly an efficiency of the passivation by H.

To discuss for individual for ions irradiation, the author speculated that this was caused by low (below 100 eV) energetic bombardments of H_n^+ from the plasmas. Since the bombardments could be broken the Ga−H bonds, since the several 10 eV was higher enough to break the Ga−H bonds (literal bond energy of Ga−H is 2.69 ~ 2.81 eV) [25]. During plasma exposure, both H and H_n^+ were irradiated; a balance between passivation by H and depassivation by H_n^+ should determine the net efficiency of passivation. In other words, under coexistence of the H_n^+, the Ga−H bonds were dissociated by H_n^+ bombardments even with relatively low energy below a few tens of eV. Therefore, higher of the Γ_r/Γ_i could provide higher passivation efficiency.

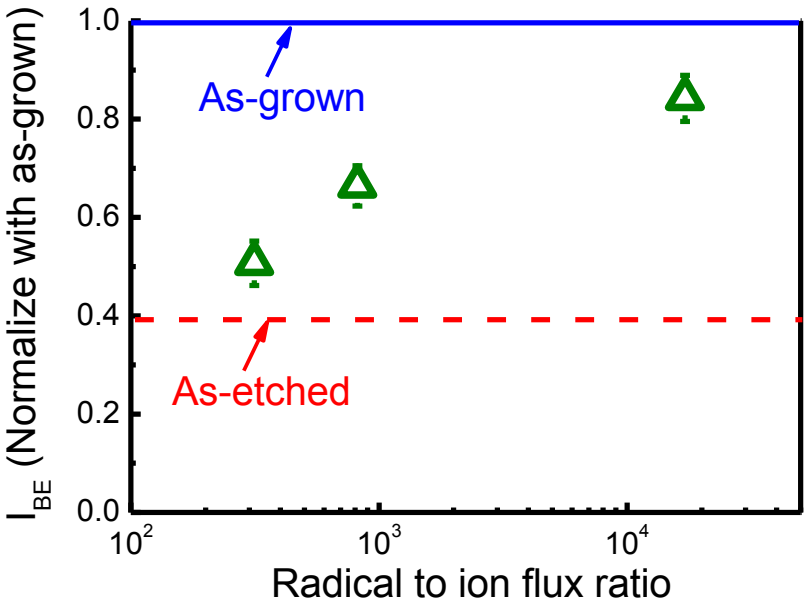

Figure 5.10 PL intensity of band-edge emission (I_{BE}) as a function of hydrogen radical to ion flux ratio together with the I_{BE} of as-grown and as-etched sample.

5.3.3 Spectra of cathodoluminescence at 100 K

Extensively to confirm the complicated nature of the band-edge emissions (BE), the measurements of cathodoluminescence (CL) with excitation electron energy of 2 keV at low temperature of 100 K was carried out. Figure 5.11 shows CL spectra normalized by intensities of the BE at 3.47 eV. Other emissions from near band edge (NBE) ranged between 3.40 and 3.46 eV, ultraviolet luminescence (UVL) ranged between 3.2 and 3.4 eV, and yellow luminescence (YL) ranged between 2.2 and 2.6 eV were also depicted.

For the YL, many researchers reported their assignment of the YL to the gallium-vacancy (V_{Ga}) and shallow donor complex [26]. Here we do not discuss in details about an origin of the YL peak since it was not significantly changed after H passivation. It was reported that the UVL was originated from shallow-donor-acceptor-pair (DAP) recombination, substitutes Si_{Ga} and O_N [27, 28], or shallow acceptor, substitutes of Si at N sites (Si_N) [26]. Summarized the experimental results here, both of the intensities for the UVL and the YL were not linked but those for the NBE and the UVL showed some linkage. According to identification of the UVL and the YL, the recovery of photoluminescence in this case was originated from transformation of the non-radiative N vacancy related acceptor to radiative N vacancy and H complex (V_N—H). From this point of view, the author speculated that the N vacancy related defects were created during the plasma etching, whereas the BE intensities decreased with increasing the ratio of intensities for the NBE and the UVL bands. At least, it is well known that the V_N is mainly generated during plasma etching by evaporating etching products favorable in case for nitrogen (i.e. $NCl_3 > GaCl_3$) [29]. By the H exposure, passivation of the N vacancy might be terminated by H, whereas the BE intensities were

recovered with transforming non-radiative V_N related centers to radiative V_N–H complex.

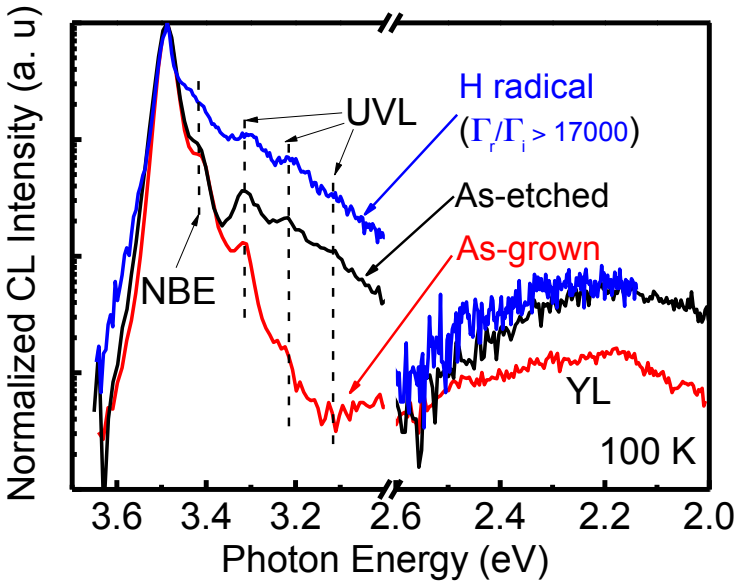

Figure 5.11 Cathodoluminescence (CL) of as grown, as-etched, and radical-passivated GaN (Γ_r/Γ_i > 17000) at 100 K. The spectra were measured under the electron energy of 2 keV.

The V_N—H complex has been studied by Van de Walle [23]. The researcher reported that N vacancy (V_N) related-complexes binding with hydrogen have low formation energy of 1.56 eV for $(V_NH)^{2+}$ [29], unstable forms of $(V_NH_3)^0$ [27]. They also reported that the V_N—H complex has an energy level close at above the valence band edge, that is, acting as acceptor-like defect [30]. This implied that the V_N—H complex coupled easily with the donor-like defect and played also with acting as a shallow-donor after passivation of hydrogen. This supports the as-described interpretation that the BE intensities were recovered with transforming non-radiative centers related V_N to radiative centers of V_N—H complex.

Moreover it should be discussed about depth profile for the defects. From the view point of that plasma etch reaction occurred in the shallow region beneath surface, we confirmed the depth profile by changing excitation electron energy of 5 keV instead of 2 keV. As shown in Fig. 5.12, the intensities for NBE, UVL and YL are seen almost remaining unchanged although the CL spectrum taken with 5 keV contained signals from deeper depths. Therefore the defects located within shallow region at close to the surface. Hence plasma etched damage layer existed within depths of 60 nm which corresponded with a detectable depth for 2 keV measurements. In the previous report, the defected depth was mentioned to be over 100 nm on the basis of depths for inducing the plasma emission (at wavelength shorter than 365 nm) [4]. This was in a good agreement with our result of the similar CL spectra obtained from 50 and 100 nm thickness of the damaged GaN films. It suggests that the thickness of damage layer was below 100 nm and enough thinner that the hydrogen atoms could sufficiently penetrate into defect sites by thermal diffusion.

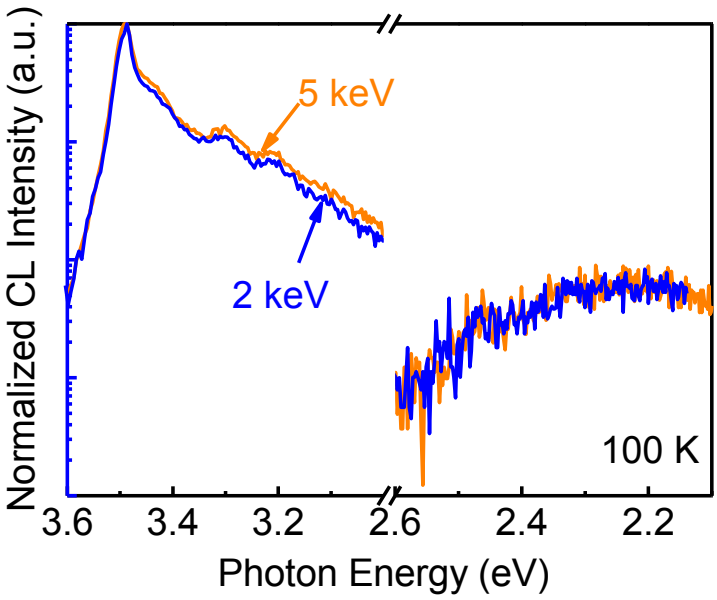

Figure 5.12 Comparison of the cathodoluminescence spectra for the radical-passivated GaN ($\Gamma_r/\Gamma_i > 17000$) taken at electron energy of 2 keV (as same shown in Fig. 5.11) with that of 5 keV.

5.3.4 Surface stoichiometry

To confirm the model described above, the author also studied surface stoichiometry changes after H radical exposure. For the as-grown sample, spectral components consisted mainly of the Ga－N bonds. For the as-etched sample, small amount of chlorides reside because plasma chemistry used was chlorine. Notably it is also seen to increase component for the Ga－O bonds. This indicated that the plasma-etched surface was oxidized during transport and store under atmospheric ambient after plasma etching process. The surface after the plasma etching processes was oxidized since a lot of dangling bonds was formed by desorption of nitrogen-containing products and the damaged lattice formation by ion bombardments. This was supported by the fact that a decrease to be less than unity in a ratio of nitrogen to gallium (N/Ga) after the plasma etching.

Figure 5.13 shows the XPS spectra for narrow region of Ga 3d. The intensities were normalized by intensity for the peak arisen from Ga－N bonds located at 19.9 eV. The spectral feature was decomposed into overlapping signals arisen from Ga−O bonds located at around 21.0 eV. This was supported by observation of some broadening of the peaks directed to higher binding energy and a full width half maximum (FWHM) increased slightly. An additional feature at a binding energy of 18.4 eV as a shoulder of the main peak was seen on the spectrum for sample at the value of the Γ_r/Γ_i more than 17000. This peak was commonly interpreted by formation of reduced states of Ga instead of Ga－N or Ga－O bonds. According to this, we believe that the peak was arisen from Ga－H bond. As a result that when the Γ_r/Γ_i increased, the intensities for the Ga－H features were increased, this supported that a large amount of dangling bonds on Ga capable to be passivated by H exposure.

On the other hand, the N/Ga was kept a constant before and after the H_2 plasma treatments so we believed that to increase values for the I_{BE} caused mainly by the passivation of V_N by H terminating. Combined with the CL results with respect to the depth profile, a damaged region was limited in the depth shallower than 50 nm, therefore, the author believed that the H may be able to penetrate for the passivation of the defects. This was supported reasonably by other damages in the plasma etching process.

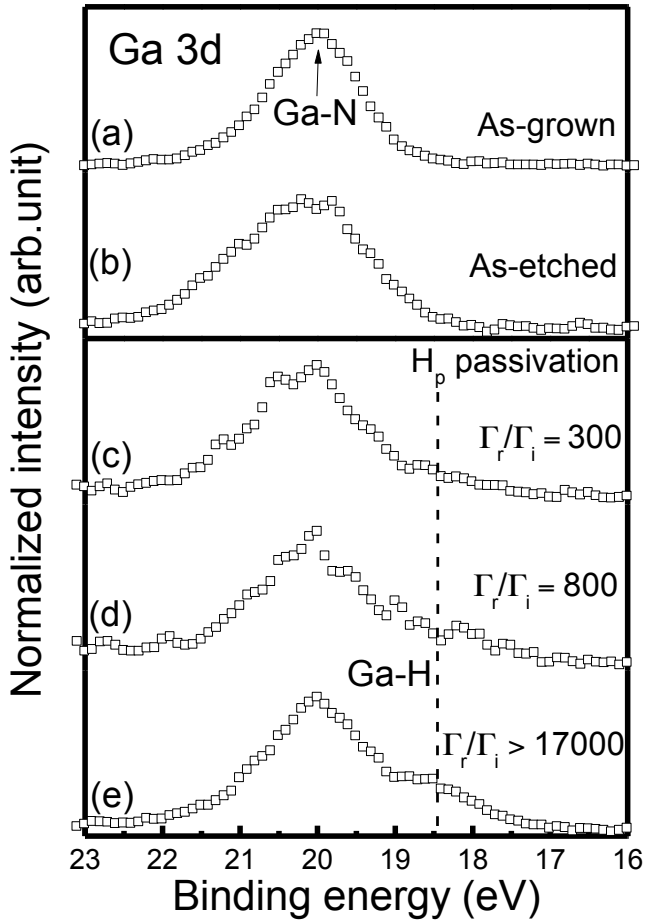

Figure 5.13 XPS spectra of narrow region for Ga 3d of samples for as grown (a), as etched (b), and H_2 plasma treated with Γ_r/Γ_i at 300 (c), 800 (d), and more than 17000 (e).

5.4 Model of hydrogen radical passivation

Lastly, interpretation about the passivation mechanism by the H exposure to the damaged GaN films was summarized. During the plasma etching, defect as nitrogen vacancy was created by selectively desorption of N on the basis of highly energetic bombardments of Ar and Cl_n ions (n = 1, 2) in GaN film,

$$\equiv Ga-N-Ga\equiv \rightarrow \equiv Ga-(V_N^0)-Ga\equiv + N\uparrow$$

The V_N^0 is a main cause of reduction of the BE intensities in photoluminescence spectra, that is, working as the NRR. Under a circumstance of exposing the etched GaN film to hydrogen plasmas including H and H_n^+, the passivation and the depassivation were simultaneously occurred; a role of the H is terminated to the V_N^0, and then created nitrogen vacancy hydrogen complex, V_N-H,

$$V_N^0 + H \rightarrow (V_N-H)$$

This complex site is captured favorably holes (h^+) to behave a shallow-acceptor [23] as radiative,

$$(V_N-H) + 2\,h^+ \rightarrow (V_N-H)^{2+}$$

Oppositely a role of the H_n^+ is dissociated to the Ga–N bonds at the V_N-H sites,

$$(V_N-H) + H_n^+ (> \text{several eV}) \rightarrow V_N^0 + H_2\uparrow$$

Thus, the balance of the passivation of H and depassivation of H_n^+ is determined the number of defective non-radiative centers, that is suggesting the individual roles of H and H_n^+ during the H plasma treatment. Consequently the author emphasize that a balance of fluxes for atoms and ions is important under consideration of efficiency of the photoluminescence recovery. For consideration of keeping the flux ratio of atoms high, the post process described in this study using the radical source-type instrument is a candidate.

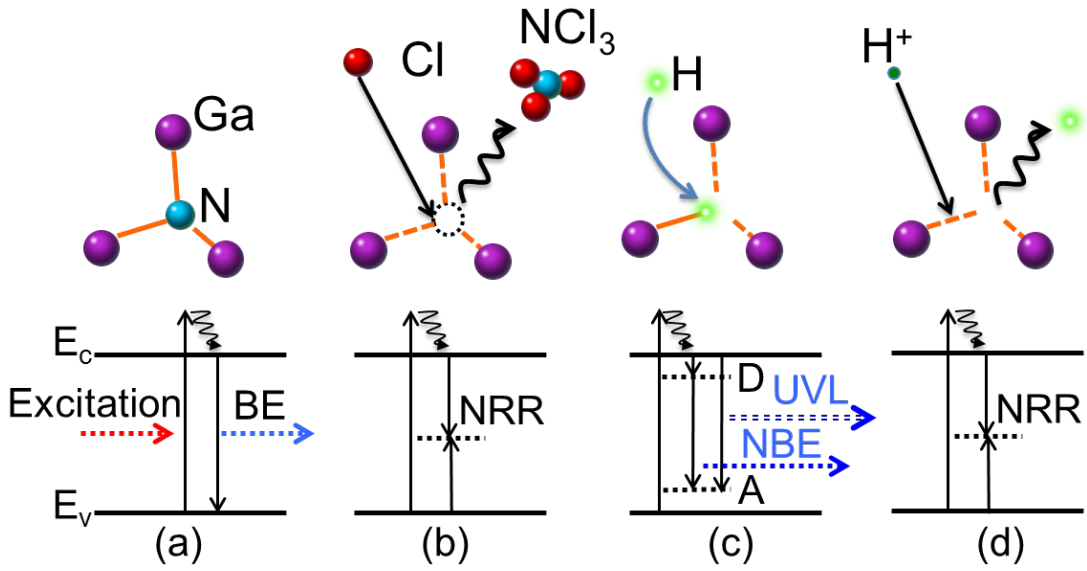

Figure 5.14 Schematic representations of dominant process related the defective centers in GaN crystal and their energy band diagram related the transitions with respect to photoluminescence. (a) For the as-grown GaN, the inter band transitions of band-edge (BE) luminescence are generated. (b) For the as-etched one, the nitrogen vacancy (V_N) related defects were created and acted as NRR. (c) By the H passivation, the V_N is passivated with form of the V_N—H complex, which may act as acceptor (A) and donor (D) sites to generate the UVL. (d) With simultaneous irradiation of energetic ionic species, this resulted depassivation of the V_N—H complex back to the V_N.

5.5 Summary

The optical and stoichiometric properties of plasma-damaged GaN after exposure to H radicals at room temperature were investigated by PL and XPS. I_{BE} drastically decreased after Cl_2 plasma-beam etching due to point defects, mainly generated by ion bombardment at the surface. After H radical exposure, I_{BE} increased with increasing radical dosage to almost reach the as-grown value. The H radicals terminate the dangling bonds of Ga on the GaN surface, as indicated by the Ga 3d XPS spectrum, as well as desorb surface residues.

For passivation of plasma-etching damaged GaN surface by exposure hydrogen plasmas, the individual roles for atoms and ions of hydrogen have been investigated. The experimental results showed that as increased Γ_r/Γ_i, the efficiency of passivation, which was observed by the emissions from the band-edge located at around 3.47 eV, significantly increased. This behavior could be interpreted by; (1) plasma etching damaged defects were mainly composed by nitrogen vacancy related complexes, acting as non-radiative recombination centers (NRR); (2) by exposing to atomic hydrogen, the V_N related complexes binding with hydrogen formed to be passivated the NRR and instead of working as shallow-donors, which were generated emissions at near-band edge (NBE) and ultraviolet luminescence (UVL); (3) besides irradiation of ions break the formed Ga－H bonds. Therefore the efficiency of passivation shifts to lower by balancing between passivation and dissociation of the V_N. This study revealed the individual roles for atoms and ions in hydrogen plasma passivation for plasma-etching damaged GaN. Consequently we suggest that the higher flux ratio (Γ_r/Γ_i) for atoms to ions (higher than 17000) is effective for the recovery process.

5.6 Reference

[1] S. J. Pearton: *GaN and related materials Vol. II* (Gordon and Breach, New York, 1999).

[2] I. Adesida, J. H. Edgar, S. Strite, I. Akasaki, H. Amano, C. Wetzel: *Properties, processing and applications of GaN and related semiconductors. EMIS Data ReviewsNo. 23* (INSPEC, London, 1999).

[3] H. Cho, C. B. Vartuli, C. R. Abernathy, S. M. Donovan, S. J. Pearton, R. J. Shul, and J. Han: Solid State Electron. **42** (1998) 2455.

[4] H. S. Kim, G. Y. Yeom, J. W. Lee, and T. I. Kim: Thin Solid Films, **341** (1999) 180.

[5]W. V. Schoenfeld, C. H. Chen, P. M. Petroff, and E. L. Hu: Appl. Phys. Lett. **73** (1998) 2935.

[6] P. Hacke, T. Detchprohm, K. Hiramatsu, and N. Sawaki: Appl. Phys. Lett. **63** (1993) 2676.

[7] J. D. Guo, M. S. Feng, R. J. Guo, F. M. Pan, and C. Y. Chang: Appl. Phys. Lett. **67** (1995) 2657.

[8] X. A. Cao, H. Cho, S. J. Pearton, G. T. Dang, A. P. Zhang, F. Ren, R. J. Shul, L. Zhang, R. Hickman, and J. M. Van Hove: Appl. Phys. Lett. **75** (1999) 232.

[9] J. M. Lee, K. M. Chang, S. W. Kim, C. Huh, I. H. Lee, and S. J. Park: J. Appl. Phys. **87** (2000) 7667.

[10] F. F. Chen, and J. P. Chang: *Lecture Notes on Principles of plasma processing*, (Plenum/Kluwer, New York, 2002).

[11] B. S. Yoo, S. J. Park, and K. H. Park: J. Vac. Sci. Technol. **A 13** (1995) 931.

[12] S. Chen, R. Kometani, K. Ishikawa, H. Kondo, K. Takeda, H. Kano, Y. Tokuda, M. Sekine, and M. Hori:63rd Gaseous Electric Conference and 7th International Conference on Reactive Plasma, 2010, BT1-005.

[13] S. Chen, Y. Nagae, M. Nakai, K. Ishikawa, H. Kondo, H. Kano, K.Takeda, T. Tokuda, M. Sekine and M. Hori: 2nd International Symposium on Advanced PlasmaScience and its Applications for Nitrides and Nanomaterials, 2010, PA031A.

[14] D. Buttari, A. Chini, M. Meneghesso, E. Zanoni, B. Moran, S. Heikman, N. Q. Zhang, L. Shen, R. Coffie, S. P. Denbaars, and U. K. Mishra: IEEE Trans. Electron. Device Lett. **23** (2002) 76.

[15] Y. Setsuhara, S. Miyake, Y. Sakawa, and T. Shoji: Jpn. J. Appl. Phys. **38** (1999) 4263.

[16] S. Chen, H. Kondo, K. Ishikawa, K. Takeda, M. Sekine, H. Kano, S. Den, and M. Hori: Jpn. J. Appl. Phys. **50** (2011) 01AE03.

[17] S. Takashima, M. Hori, T. Goto, A. Kono, M. Ito, and K. Yoneda: Appl. Phys. Lett. **75** (1999) 3929.

[18] B. Chapman: *Glow Discharge Processes: Sputtering and Plasma Etching* (Wiley, New York, 1980).

[19] C. G. Van de Walle: Phys. Rev. B **56** (1997) R10020.

[20] T. Mattila, and R. M. Nieminen: Phys. Rev. B **55** (1997) 9571.

[21]F. Ren, J. R. Lothian, S. J. Pearton, C. R. Abernathy, C. B. Vartuli, J. K. Mackenzie, R. G. Wilson, and R. F. Karlicek: J. Electron. Mater. **26** (1997) 1287.

[22] B. Chapman, *Glow Discharge Processes: Sputtering and Plasma Etching* (Wiley, New York, 1980).

[23] S. Takashima, S. Arai, M. Hori, T. Goto, A. Kono, M. Ito, and K. Yoneda: J. Vac. Sci. Technol. A **19** (2001) 599.

[24] S. Chen, Y. Lu, R. Kometani, K. Ishikawa, H. Kondo, Y. Tokuda, M. Sekine, and M. Hori: AIP Advances **2** (2012) 022149.

[25] K. Balasubramanian: Chem. Phys. Lett. **164** (1989) 231.

[26] M. A. Reshchikov and H. Morkoc: J. Appl. Phys. **97** (2005) 97.

[27] R. Dingle and M. Ilegems: Solid State Commun. **9** (1971) 175.

[28] J. A. Freitas, W. J. Moore, Jr., B. V. Shanabrook and G. C. B. Braga, S. K. Lee, S. S. Park, and J. Y. Han: Phys. Rev. B **66** (2002) 233311.

[29] N. Medelci, A. Tempez, D. Starikov, N. Badi, I. Berishev, and A. Bensaoula: J. Electron. Mater. **29** (2000) 1079.

[30] B. Szucs, A. Gali, Z. Hajnal, P. Deak, and C. G. Van de Walle: Phys. Rev. B **68** (2003) 085202.

Chapter 6

Conclusion

6.1 Present work

In chapter 3, the development of high-density source of atomic nitrogen (HDRS) for MBE growth of nitride films was presented. Absolute density of atomic nitrogen (n_N) was enabled to supply as high as 2.3×10^{12} atoms cm^{-3} at growth position (diffusion region of plasma) measured by VUVAS. I also measured the absolute densities of H and N radicals together with NH_3 molecules in the remote region of the radical source by VUVAS and QMS. The absolute density of N atoms at the remote region was on the order of 10^{13} atoms cm^{-3}. I found that N atom density was influenced considerably by the experimental history. After applying H_2-containing plasma discharges, N radical density was unstable since residual hydrogen possibly affected the dissociations of N_2. Additionally, the surface loss probability of the N radicals on PBN influenced N density at the remote region of the radical source under a pressure of about 1 Pa. The absolute density of NH_3 on the order of 10^{13} atoms cm^{-3} was evaluated at the remote region in the H_2 and N_2 mixture gas discharges, since the dominant mechanism for NH_3 generation is considered to be the surface reactions inside the PBN discharge tube owing to the large surface ratio over the volume. Noticeably, to determine the remote densities of N, H, and NH_3, the surface conditions on the PBN discharge tube and the configuration of surface to volume ratio is the crucial important parameters.

In chapter 4, a high-density radical source for an RF PA-MBE system was developed to realize a high growth rate for GaN film. A high growth rate of 1.4 μm/h

was achieved with an atomically smooth surface for the epitaxy layer grown by RF PA-MBE using the HDRS. The growth rate was almost three times higher than that in the case of using the CRS. A high growth rate of 1.4 μm/h was also achieved for the heteroepilayer of InGaN grown using the HDRS. The growth rate was almost three times higher than that in the case of using the CRS of 0.5 μm/h. Notably, the crystalline property was greatly improved, which confirmed by XRC profile for (0002) plane diffraction in the films with InN molar fraction of 3 to 18 %. The FWHM of XRC was decreased from 1400 to 600 arc sec at InN molar fraction around 17 %.

In chapter 5, the optical and stoichiometric properties of plasma-damaged n-GaN after exposure to H radicals at room temperature were investigated by PL and XPS. I_{BE} drastically decreased after Cl_2 plasma-beam etching due to point defects, mainly generated by ion bombardment at the surface. After H radical exposure, I_{BE} increased with increasing radical dosage to almost reach the as-grown value. The H radicals terminate the dangling bonds of Ga on the GaN surface, as indicated by the Ga 3d XPS spectrum, as well as desorb surface residues. For passivation of plasma etching damaged GaN surface by exposure hydrogen plasmas, we investigated the individual roles for atoms and ions of hydrogen. The experimental results showed that as increased Γ_r/Γ_i, the efficiency of passivation, which was observed by the emissions from the band-edge located at around 3.47 eV, significantly increased. This behavior could be interpreted by; (1) plasma etching damaged defects were mainly composed by nitrogen vacancy related complexes, acting as non-radiative recombination centers (NRR); (2) by exposing to atomic hydrogen, the V_N related complexes binding with hydrogen formed to be passivated the NRR and instead of working as shallow-donors, which were generated emissions at near-band edge (NBE) and ultraviolet luminescence (UVL); (3) besides irradiation of ions break the formed Ga−H bonds. Therefore the efficiency of passivation shifts to lower by balancing between passivation and dissociation of the V_N.

This study revealed the individual roles for atoms and ions in hydrogen plasma passivation for plasma etching damaged GaN. Consequently we suggest that the higher ratio of fluxes for atoms to ions (higher than 17000 of Γ_r/Γ_i) is effective for the recovery process.

6.2 Perspectives in future

For development of plasma source, aperture between the source chamber and main chamber (process chamber) is an essential factor. It can simply change the pressure difference between two chambers, and plasma parameter will be affected by the pressure significantly. The design of aperture structure including the diameter, number, arrangement of hole can decide the species content (ratio of radical to ion) and area of species irradiation.

For plasma assistant GaN growth, it is important to realize the interaction of active species from plasma with the surface of substrate by the absolute number for each species involving in surface process. However, this study does not monitor the absolute density in MBE chamber *in-situ*, but in a measurement chamber. So the measured value was not reflecting the true value injected to substrate which set in the MBE chamber. The mechanism of GaN growth should be understood based on absolute number of Ga and N species. Moreover, the real time monitoring of reactive species, which could reveal the phenomena of initial step of GaN growth, was also demand. On the other hand, MOCVD is a main trend technology for mass fabrication of GaN. It should be interesting that combining of the plasma source with MOCVD hopefully offers a low growth temperature and can cut down the cost of gas resource.

In damage less process, we have investigated the post-etching process; however, the low damage plasma etching should also be addressed. The plasma etching on compound semiconductor is key issue in the future. It is much more difficult than single element material as silicon. The differential vapor pressure of each product (i.e. $GaCl_n$ and NCl_n) leads preference desorption from the surface and cause a non-stoichiometric surface, which may degrade the performance of devices. Therefore, an innovated work to break though the plasma process may need.

Appendix

A. As-grown deep-level defects in n-GaN grown by metal–organic chemical vapor deposition on freestanding GaN

In the chapter 5, I have investigated the optical property of GaN. However, the variance of electrical property during the plasma etching and recover process should also clarified. Here, I represent an attempt on further investigating of the electrical property to understand the details of defects (depth profile, concentration, and energy level) in GaN films using deep level transient spectroscopy (DLTS). As a first step, the as-grown defects in freestanding GaN substrate were investigated.

Abstract

Traps of energy levels $E_c-0.26$ and $E_c-0.61$ eV have been identified as as-grown traps in n-GaN grown by metal–organic chemical vapor deposition (MOCVD) by using deep level transient spectroscopy (DLTS) of the Schottky contacts fabricated by resistive evaporation. The additional traps of $E_c-0.13$ and $E_c-0.65$ eV have been observed in samples whose contacts are deposited by electron-beam evaporation. An increase in concentration of the $E_c-0.13$ and $E_c-0.65$ eV traps when approaching the interface between the contact and the GaN film supports our argument that these traps are induced by electron-beam irradiation. Conversely, the depth profiles of as-grown traps show different profiles between several samples with increased or uniform distribution in the near surface below 50 nm. Similar profiles are observed in GaN grown on a sapphire substrate. The author conclude that the growth process causes these large concentrations of as-grown traps in the near-surface region. It is speculated that

the finishing step in the growth process should be an essential issue in the investigation of the surface state of GaN.

I. Introduction:

Gallium nitride (GaN) has emerged as the most promising material for a great number of potential applications in optical and high-power electronic devices [1-4]. However, GaN-based devices have suffered from poor performance caused by the lack of native substrates; thus, resulting in a high density of dislocations in epitaxial GaN [5-7]. In the last decade, methods for growing GaN have developed rapidly, allowing much lower background donor and acceptor concentrations, and sharper or more intense photoluminescence [8-10]. In particular, there have been several studies on the fabrication of GaN-based devices grown homoepitaxially on freestanding GaN substrates since a decrease in dislocation density has been achieved. Consequently, improvements in the performance of pin rectifiers, light-emitting diodes, and high electron mobility transistors have been reported [11-13]. However, in recent years, the prevalence of deep-level defects in GaN has begun to affect device performance; thus, attracting much attention of the researchers. So far, much of the research has concentrated on identifying defects in GaN that may act as donors, acceptors, traps, or recombination centers [14]. A number of deep-level defects in n-GaN have been evaluated by deep-level transient spectroscopy (DLTS), which has revealed activation energies in the range of 0.15–0.80 eV and trap densities in the range of $10^{13} \sim 10^{15}$ cm^{-3} [15-17]. Tokuda *et al*. have studied the vertical-type Schottky diodes and the p–n junction on freestanding GaN substrate and found no dislocation-related traps of the type previously observed in GaN on sapphire. This indicates that a reduction in dislocation density is correlated to homoepitaxial growth [18-20]. However, aspect of as-grown traps is still remaining a contradiction since the different DLTS spectra have

been reported by several groups. One of the reasons is contact deposition process that affects the electrical properties of GaN as did sputter deposition, which induced defects similar to radiation-induced defects [21]. DeLucca *et al*. studied magnetron-sputtered and electron-beam-evaporated Pt contacts on n-GaN and found that the electrical properties are strongly influenced by the presence of electrically active defects introduced during metal deposition [22]. To the best of our knowledge, there are few reports on as-grown defects in GaN grown homoepitaxially on bulk GaN substrate that consider the profile of traps in different contact deposition processes.

The objective of this study is to distinguish the truly as-grown traps in freestanding n-GaN films from those traps induced by the contact deposition process. Resistive evaporation (RE) and electron-beam evaporation (EB) are used to fabricate Schottky contacts, while ohmic contacts are formed by EB only. Finally, the results of an analysis of GaN films on sapphire substrates are also used to support our argument.

II. Experiment

Metal–organic chemical vapor deposition (MOCVD) grown n-GaN films with thicknesses of 1.2 and 5 μm on hydride vapor phase epitaxy (HVPE) grown n^+-GaN are used in this study. The carrier density is $6 \times 10^{16}\,cm^{-3}$ at room temperature. Prior to depositing the metal contact, samples are cleaned by dipping in 2% hydrofluoric acid (HF) for 1 min and 50% hydrochloride acid (HCl) for 5 min to remove native oxides and metallic contaminants, respectively. Ohmic contacts of Ti/Al/Ni/Au are deposited by EB underneath the GaN substrate. Schottky contacts with 300-μm-diameter Pt/Au are deposited by RE or EB on the GaN films to form a vertical-structure Schottky diode. In the case of GaN films grown on a sapphire substrate, a planar-structure Schottky diode is used. The RE-deposited circle hollow structured Ohmic contacts surround Schottky contacts with a distance of 10 μm.

Current–voltage (I–V) and capacitance–voltage (C–V) are first used to assess the quality of the Schottky diode at room temperature. A Keithley series 2400 source meter and a Boonton 72B capacitance meter are employed to evaluate the current and capacitance, respectively. DLTS measurements for deep-level electron traps are performed in the temperature range from 80 to 400 K. To perform a surface sensitive analysis of GaN, the author apply bias pulsed from + 0.3 to 0 V with a width of 10 ms to fill the trap at the near-surface region. The isothermal DLTS is applied for the inconspicuous traps, which is difficult to assign the energy level and the cross section. Isothermal double correlation DLTS (DDLTS) is applied to analyze the depth profiles of multi-overlapping peaks since DDLTS can resolve the deep-level profile to exclude the field dependence of the emission rate and contact effects [23].

III. Results and Discussion

In both the EB- and RE-deposited Schottky contacts on freestanding GaN films, the leakage currents are lower than 0.1 $\mu A/mm^2$ at a 10 V reverse bias. This value shows a favorable contact identity and allows the DLTS evaluation to be performed. The depth profiles of carrier concentration show a flat distribution in GaN films at depths of 80 to 450 nm from the surface.

A. DLTS spectra

Figure A.1 depicts typical DLTS spectra for Schottky contacts deposited by RE (solid line) and EB (dotted line) with scan temperatures ranging from 80 to 400 K. Two traps at energy levels of $E_c-0.24$ and $E_c-0.61$ eV in RE-deposited contact are labeled E2 and E3, respectively. Additional electron traps, $E_c-0.13$ and $E_c-0.65$~0.70 eV, in EB-deposited contact are labeled E1 and E4, respectively (E4 has a broad peak that is

difficult to define accurately). The energy levels and capture cross sections of the traps are summarized in Table A.1 along with the trap concentrations.

E2 and E3 are usually observed in both freestanding GaN and sapphire-based GaN, which I defined in my previous study as B1 and B2, respectively [18]. They are also similar to D and B, which were reported by Fang *et al*. [24-26], as well as to EO2 and EO5 by DeLucca *et al*. [22]. Those traps are mostly designated as as-grown traps in GaN films because they arise even in the RE case, which is considered the lowest-damage process in metal deposition [27]. E2 might be assigned to the V_N–V_{Ga} pair, while E3 is an N_{Ga}-related trap [6, 25]. The significant difference on intensity of E3 between RE and EB should be caused by spatial distribution [18]. The details of these two traps are described later.

Table A.1 The energy levels, capture cross sections, and origin of the traps.

	Energy level (eV)	Cross section (cm^2)	Origin
E1	Ec −0.13	9.6×10^{-17}	EB
E2	Ec −0.24	1.4×10^{-14}	Native
E3	Ec −0.61	6.8×10^{-15}	Native
E4	Ec −0.65~0.70	$\sim 5 \times 10^{-17}$	EB

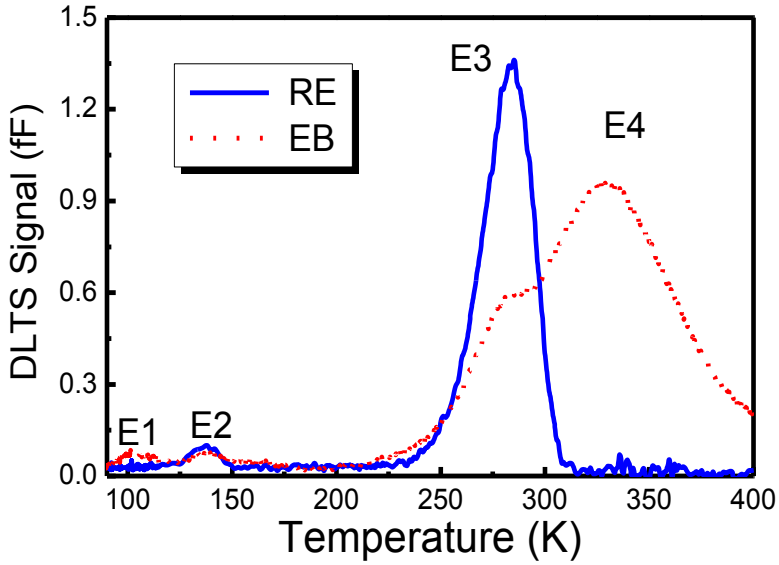

Figure A.1. DLTS spectra for a Schottky diode deposited by RE and EB on freestanding n-GaN.

Conversely, E1 and E4 arise only in the EB case, which reveals the possibility that these traps are induced by high-energy electrons. These traps are similar, with E, A, and the peak of A overlapping with A_1 [24-26]. DeLucca *et al*. have observed Ee1 and EO6, which show similar behaviors to E1 and E4. Ee1 and EO6 also appear in the sputtering deposition case, which may involve energetic ion bombardment [22]. Fang *et al*. have reported that a trap, which has the same kinetic to the E1, is a nitrogen-vacancy-related defect that can be induced by electron beam irradiation [24]. E1, which also arises in plasma-etched samples, may be induced by collision of charged species since nitrogen vacancies can be observed in such surfaces of GaN films. The E1 peak is suspiciously similar to a contact-deposition-induced deep-level defect; therefore, it should be investigated at its low detection level. Hence, isothermal DLTS is performed at a reverse voltage of + 2 to 0 V and a pulse width of 10 ms. The measurement temperature is 90 K. The results depicted in Fig. A.2 shows that E1 exhibits a sufficient intensity only in the EB case. E4 has an overlapped structure, making it difficult to define the trap kinetics, but its behavior is suggestive of a line defect of the type typically associated with threading dislocations [26].

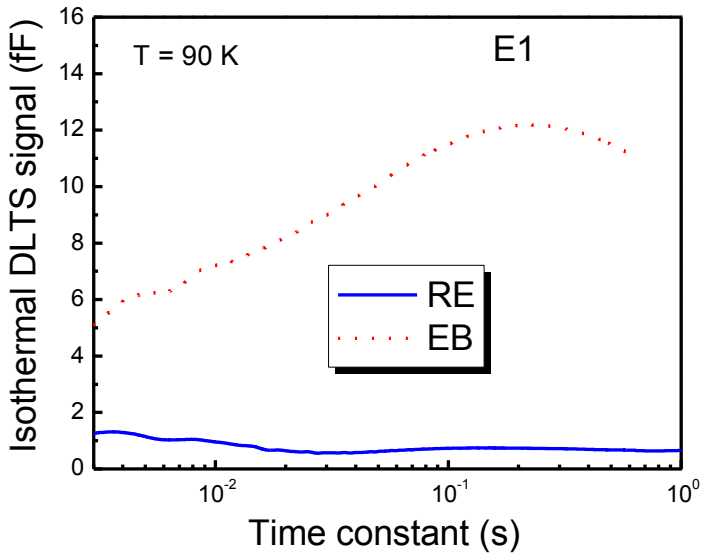

Figure A.2. Isothermal DLTS spectra of E1 trap in RE- and EB-deposited Schottky diode.

B. Depth profiles of traps

Figure A.3 shows a peculiar depth profile of the E1 peak, in which it increases in concentration as the depth approaches 50 nm from the surface. Such a defect might be introduced by a metal deposition process such as EB. DeLucca *et al*. have found that an EB-induced deep-level defect at E_c−0.25 eV [22], exhibits a similar property even though EB does not produce evaporative particles of high kinetic energy incident to the GaN surface. The impact of the electron beam with the evaporative metal produces X-rays possibly energetic enough to create surface defects [22].

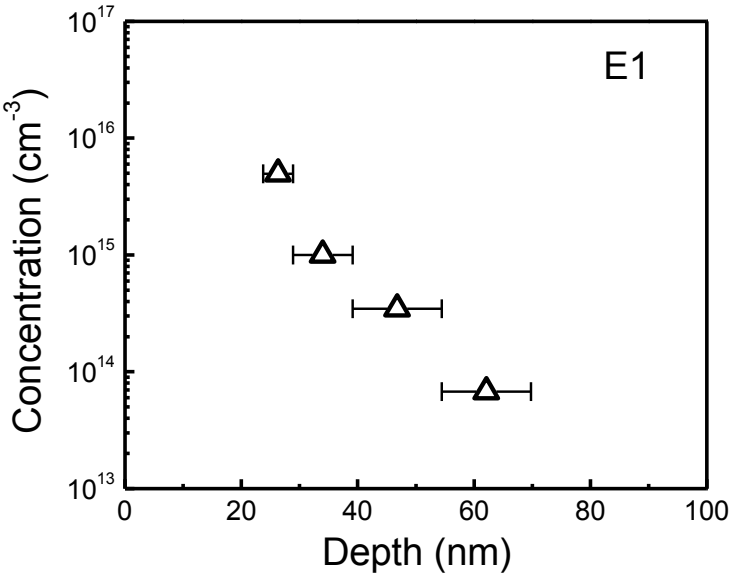

Figure A.3. Depth profile of E1 trap from 25 to 60 nm below the interface of the contact and the GaN films

The E4 trap has a broad peak, probably because of multiple overlapping peaks. It is difficult to separate a peak of this type because the capture rate is uncharted. The depth profile of the E4 trap measured by isothermal DDLTS is performed at 390 K is shown in Fig. A.4. The concentration of the E4 trap decreased with increasing depth, which might indicate that E4 could also be a process-related trap. In this study, contact deposition should be considered since E4 does not appear in the RE case. Its presence could also be related to the use of EB to fabricate the Schottky diode [22].

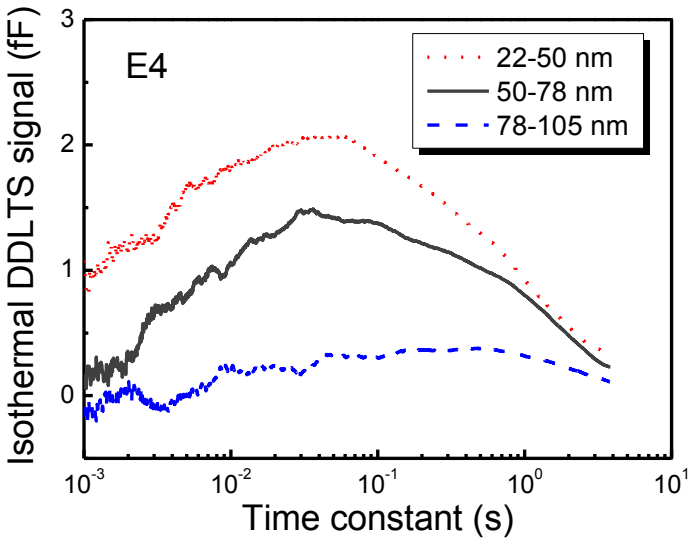

Figure A.4. Isothermal DDLTS spectra of E4 traps at depth ranges from 22 to 50 nm, 50 to 78 nm, and 78 to 105 nm.

For E2 and E3, which are suggested as being as-grown traps, the depth profiles are investigated to clarify their origins. I also compare them to the GaN films grown on a sapphire substrate. The depth profiles of E2 in two freestanding GaN samples labeled 1# (1.2 μm) and 2# (5 μm) are compared with sapphire-based GaN in Fig. A.5. These two samples differ only in their thickness. In all samples, an increase in the concentration of E2 traps is obtained when the depth approaches the interface between the contact and the GaN films. The depth profiles of E3 are shown in Fig. A.6. The sapphire-based GaN and the freestanding GaN 1# have a similar E3 profile, which shows increased concentration when approaching the surface. In particular, 2# shows a flat trap distribution, suggesting that the surface state might be controlled by growth conditions. In the finishing step of the growth process with both MBE and MOCVD, the procedure is usually to turn off the heater and maintain the flow rate of the nitrogen source (usually nitrogen for MBE, ammonia for MOCVD). Then, the mass flow controller is closed when the temperature of the substrate has decreased to room temperature. This procedure may induce surface decomposition since insufficient active species, which mainly produced by thermal dissociation are supplied during the ramp-down in temperature.

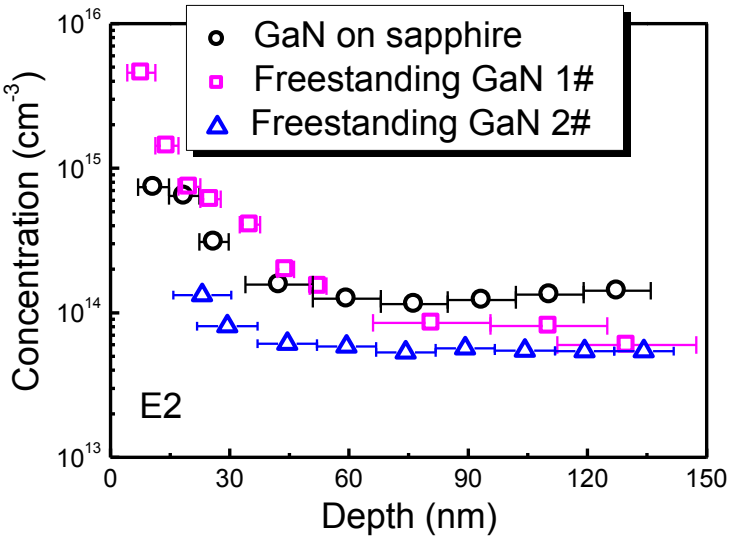

Figure A.5. Depth profile of E2 trap in two freestanding GaN films and a sapphire-substrate-based GaN film.

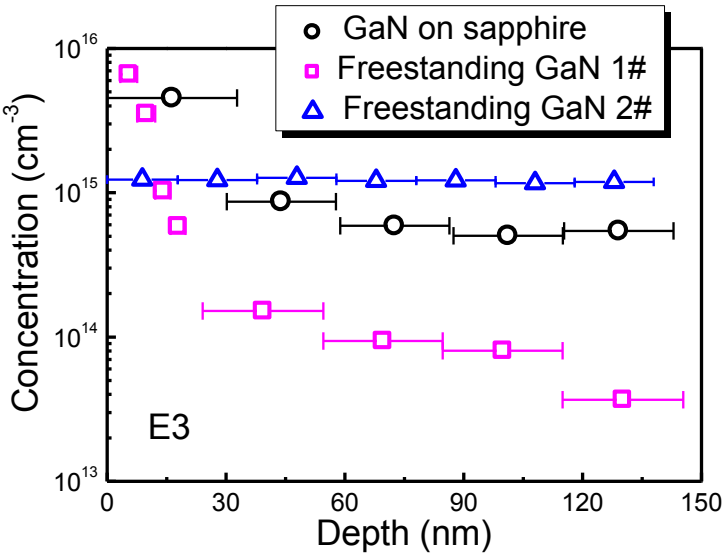

Figure A.6. Depth profile of E3 trap in two freestanding GaN films and a sapphire-substrate-based GaN film.

IV. Conclusion

The deep-level traps in freestanding GaN films have been investigated by DLTS. Two traps, $E_c-0.24$ and $E_c-0.61$ eV, are detected in RE-deposited Schottky diode. Most such traps are as-grown, but the depth profile shows an increase in concentration when approaching the interface between the contact and the GaN films. However, in some samples the concentration has a flat profile, which indicates that the increase of traps concentration would be affected by condition of growth process. For comparison, two additional traps, $E_c-0.13$ and $E_c-0.65$ eV, are prominent in EB-deposited samples. The depth profile clearly shows that $E_c-0.13$ and $E_c-0.65$ eV are more highly concentrated at the surface region, which may suggest that these traps originated from the introduction of electron beam irradiation. Overall, a high trap concentration in the near-surface region greatly affects device performance (e.g., metal-semiconductor field effect transistors). Therefore, it is important to optimize growth conditions and electrode deposition process to avoid such issue.

References

[1] H. Morkoc, S. Strite, G. B. Gao, M. E. Lin, B. Sverdlov, and M. Burns: J. Appl. Phys. **76** (1994) 1363.

[2] S. D. Lester, F. A. Ponce, M. G. Craford, and D. A. Steigerwald: Appl. Phys. Lett. **66** (1995) 12449.

[3] R. F. Davis: Physics B **185** (1993) 1.

[4] S. Nakamura, M. Senoh, S. I. Nagahama, N. Iwasa, T. Yamada, T. Matsushaita, H. Kiyoku, and Y. Sugimoto: Appl. Phys. Lett. **68** (1996) 2105.

[5] L. Chernyak, A. Osinsky, G. Nootz, A. Schulte, J. Jasinski, M. Benamara, Z. Liliental–Weber, D. C. Look, and R. J. Nolnar: Appl. Phys. Lett. **77** (2000) 2695.

[6] Z. –Q. Fang, D. C. Look, J. Jasinski, M. Benamara, Z. Liliental–Weber, and R. J. Molnar: Appl. Phys. Lett. **78** (2001) 332.

[7] D. C. Look and R. J. Molnar: Appl. Phys. Lett. **70** (1997) 3377.

[8] S. S. Park, I. –W. Park, and S. H. Choh: Jpn. J. Appl. Phys., Part 2 **39** (2000) L1141.

[9] D. C. Look and J. R. Sizelove: Appl. Phys. Lett. **79** (2001) 1133.

[10] D. C. Look, J. R. Sizelove, J. Jasinski, Z. Liliental-Weber, K. Saarinen, S. S. Park, and J. H. Han: Mater. Res. Soc. Symp. Proc. **743** (2003) 575.

[11] X. A. Cao, S. F. LeBoeuf, M. P. D'Evelyn, S. D. Arthur, J. Kretchmer, C. H. Yan and Z. H. Yang: Appl. Phys. Lett. **84** (2004) 4313.

[12] Y. Irokawa, B. Luo, J. Kim, J. R. LaRoche, E. Ren, K. H. Baik, S. J. Pearton, C.-C. Pan, G.-T. Chen, J.-I. Chyi, S. S. Park and Y. J. Park: Appl. Phys. Lett **83** (2003) 2271.

[13] X. A. Cao and S. D. Arthur: Appl. Phys. Lett. **85** (2004) 3971.

[14] D. C. Look: Phys. Status Solid B **228** (2001) 293.

[15] P. Hacke, T. Detchprohm, K. Hiramatsu, N. Sawaki, K. Tadatomo, and K. Miyake: J. Appl. Phys. **76** (1994) 304.

[16] D. Haase, M. Schmid, W. Kurner, A. Dornen, V. Harle, F. Scholz, M. Burkard, and H. Scheizer: Appl. Phys. Lett. 69 (1996) 2525.

[17] W. K. Gotz, J. Walker, L. T. Romano, N. M. Johnson, and R. J. Molnar: Mater. Res. Soc. Symp. Proc. **449** (1997) 525.

[18] Y. Tokuda, Y. Matsuoka, H. Ueda, O. Ishiguro, N. Soejima, and T. Kachi: Superlattices and Microstructures **40** (2006) 268.

[19] Y. Tokuda, Y. Matsuoka, K. Yoshida, H. Ueda, O. Ishiguro, N. Soejima, and T. Kachi: Phys. Stat. Sol. (c) **4** (2007) 2568.

[20] Y. Tokuda, Y. Matsuoka, H. Ueda, O. Ishiguro, N. Soejima, and T. Kachi: Materials Science Forum **600-603** (2009) 1297.

[21] F. D. Auret, S. A. Goodman, F. K. Koschnick, J.-M. Spaeth, B. Beaumont, and P. Gibart: Appl. Phys. Lett. **74** (1999) 2173.

[22] J. M. DeLucca, S. E. Mohney, F. D. Auret, and S. A. Goodman: J. Appl. Phys. **88** (2000) 2593.

[23] H. Lefevre and M. Schulz: Appl. Phys. A **12** (1977) 45.

[24] Z.-Q. Fang, J. W. Hemsky, D. C. Look, and M. P. Mack: Appl. Phys. Lett. **72** (1998) 448.

[25] Z.-Q. Fang, D. C. Look, W. Kim, Z. Fan, A. Botchkarev, and H. Morkoc: Appl. Phys. Lett. **72** (1998) 2277.

[26] Z.-Q. Fang, D. C. Look, P. Visconti, D.-F. Wang, C.-Z. Lu, F. Yun, H. Morkoc, S. S. Park, and K. Y. Lee: Appl. Phys. Lett. **78** (2001) 2178.

[27] M. Ohring: *The Materials Science of Thin Films* (Academic, San Diego, CA, 1992), pp. 115-116.

Acknowledgements

During my five years of apprenticeship with Prof. Masaru Hori, you have taught me some things that go beyond the details of magnetism. Simply by watching you, I have learned the usefulness of the following attitudes. First, work hard and keep a positive attitude. Second, thinking macro and micro. Third, be tender.

I also would like to express my deep gratitude to all those who have generously helped me during my doctoral candidate.

Prof. Makoto Sekine: I appreciate your guidance, advice, and encouragement in these years. I have learned more than knowledge from you.

Prof. Hiroshi Amano: I appreciate your support on growth of nitrides and comments on radical passivation of plasma damaged GaN. I have learned much knowledge from you and your group.

Prof. Hirotaka Toyoda: I appreciate your precious comments on analysis of kinetic of radical. I also appreciate your kindness for giving me a chance to participate international training program in Germany and United states. These experiences will great affect my career life in future.

Prof. Keiji Nakamura (Chubu University): I appreciate your helpful discussion on kinetics of atomic radical in development of high density radical source.

Prof. Kenji Ishikawa: I appreciate your valuable advices during my graduate study. Your help, support, and understanding throughout my graduate career has been exceeded by your kindness.

Prof. Hiroki Kondo: I appreciate your constructive comments on theory and experiment of development of high density radical source.

Prof. Yuichi Setsuhara (University of Osaka): I appreciate you designing of the plasma-beam etching system.

Dr. Hiroyuki Kano (NU Eco engineering Co., LTD.): I appreciate your surport in the project of the radical source development. You have always been so helpful to me, nearly in every aspect of my life, since the first day I arrived in lab.

Prof. Yutaka Tokuda (Aichi Institute of Technology): I appreciate your generous help from especially in providing the experience of deep-level transient spectroscopy (DLTS) on the GaN. Many thanks for all members in Tokuda's Lab: Dr. Unhi Honda, Mr. Tatsunari Shibata, Mr. Toshiya Matumura *et al.*, for advice and comments on DLTS experiment.

Prof. Takashi Egawa (Nagoya institute of technology): I appreciate your supply of high-quality GaN substrate and comments when reviewing proceeding for international conference.

Prof. Masafumi Ito (Meijo University): I appreciate your help on optical emission measurement.

Prof. Takayuki Ohta (Meijo University): I appreciate your kindly help in staff work of ICPLANT 2012.

Prof. Mineo Hiramatsu (Meijo University): I appreciate your support on development of high density radical source.

Dr. Yohjiro Kawai: I appreciate your grateful help on performance the growth of nitride in MBE, tutor work on PL measurement, and constructive comments in the field of nitride semiconductor. It is an honor and privilege to be able to work with you.

Prof. Satomi Tajima: I appreciate your valuable advices on reviewing of my CV. Without your help I cannot even pass one job interview.

Prof. Keigo Takeda: who is a very cool assistant as well as a wonderful researcher. We worked together with project of development of high density radical source.

I would like to acknowledge Dr. Shoji Den, Dr. Koji Yamakawa, and Dr. Shunji Takahashi (Katagiri Engineering Co., Ltd), from one of the most active vacuum equipment makers in the world, for production of radical source and planetary system.

I appreciate Professor Achim Von Keudell, Prof. Jan Benedikt, and all members in Research Group Reactive Plasmas, Ruhr-University Bochum, Bochum, Germany, for giving me the opportunity to study in your group. Your guidance and valuable advices allowed me to progress in my understanding on plasma chemistry.

Dr. Dirk Hegemann (Swiss Federal Laboratories for Materials Science and Technology): it is very glad to work with you.

I appreciate Professor Jane P. Chang and all members in Electronic Materials Synthesis and plasma processing Lab, University of California, Los Angeles, Untied States of America, for giving me the opportunity to study atomic layer deposition (ALD) technology in your group. Your guidance and valuable advices allowed me to progress in my understanding on technology of advance plasma assisted ALD.

Dr. Tetsuya Tatsumi, and Dr. Masaki Minami (Sony Corporation), Dr. Shigetaka Tomiya (Sony Shiroishi Semiconductor Inc.): I appreciate your suggestions in the project of investigation the plasma induced damage in GaN.

Dr. Masakazu Kanechika and Dr. Tetsu Kachi (Toyota central R&D Labs., Inc.): I appreciate you for wonderful corporation in investigating of electrical property of plasma damaged p-GaN and effect of radical recover.

Dr. Seigo Takashima, (Plasma Center for Industrial Applications): I appreciate you for kindly help on entrance application of Nagoya University.

Dr. Fengdong Jia, Dr. Noboru Ebizuka, Dr. Jagath Kularatne, Dr. Jerome Jolibois, and Dr. Hiromasa Tanaka, thank you all for many advices and comments in daily life in Lab.

Many thanks to my current and former colleges in Hori & Sekine Lab, for their fruitful discussion and valuable comments:

Dr. Saburo Uchida, Dr. Masahiro Iwasaki, Dr. Wakana Takeuchi, Dr. Chang Soon Moon, Dr. Shingo Kondo, Dr. Tsuyoshi Yamaguchi, Dr. Hirotoshi Inui, Mr. Eiji Takahashi, Mr. Hajime Sasaki, Mr. Lee Myung Ryong, Mr. Satoshi Kono, Mr. Shigetoshi Maruyama, Mr. Takuma Machino, Mr. Tomomi Obayashi, Ms. Emi Shibata, Mr. Masayoshi Kashihara, Mr. Kenichi Ando, Mr. Tetsuya Kimura, Mr. Hiroyuki Mikuni, Mr. Kota Mase, Mr. Yuto Matsudaira, Mr. Sho Kawashima, Mr. Tokushige Kino, Mr. Yoshihiro Itani, Dr. Arkadiusz Malinowski, Dr. Hiroshi Yamamoto, Ms. Sachiko Iseki, Mr. Hyung Jun Cho, Mr. Hitoshi Watanabe, Mr. Takuya Takeuchi, Mr. Yuske Abe, Mr. Hironao Shimoeda, Mr. Koji Yasuda, Mr. Leyong Yu, Mr. Masanori Kato, Mr. Naoya Sumi, Mr. Tatsuya Hagino, Mr. Shinpei Amasaki, Mr. Takayuki Kanda, Mr. Yusuke Kondo, Ms. Lu Ya, Mr. Minyoung Ahn, Mr. Jun Kuki, Mr. Atsushi Fukushima, Mr. Takeyoshi Horibe, Mr. Tomohiro Takahashi, Mr. Kuangda Sun, Mr. Haoran Wang, Mr. Isobe, Mr. Kako, Mr. Gonda, Mr. Nakamura, Mr. Nagano, Mr. Miwa.

Special thanks to GaN group member: Dr. Younjoon Kim, Mr. Yi Lu, Mr. Park, Mr. Ryosuke Kometani, Mr. Jiadong Cao, Mr. Zecheng Liu, for giving the big pleasure in life and creating a most enjoyable work atmosphere.

Many thanks to young ladies: Ms. Mitsuko Era, Mrs. Moriyama, Mrs. Oda, Ms. Oshigane, Mrs. Taniya, Mrs. Kataoka, Mrs. Takahashi, and Ms. Yokoi for letting Lab more colorful. You are such noble and loving women who are always ready to help others. Your friendship and generous help have meant so much to me all these years.

A great appreciation to the institutes, which support my research: Nagoya University Venture Business Laboratory (VBL), Akasaki Research Center (ARC), and Center for Cooperative Research in Advanced Science & Technology (CRAST).

The last but not the least, I am deeply indebted to my family. Without their love and support, I can never have reached this far.

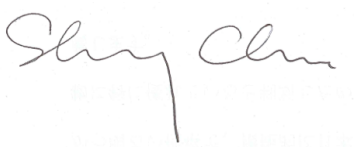

Shang Chen
June 2012

Awards

2011 Plasma Science & Technology Division travel Award, American Vacuum Society 58th International Symposium & Exhibition

2011 Japan Society of Applied Physics (JSAP) Young Scientist Oral Presentation Award

2010 Nagoya University Scholarship for Outstanding Graduate Students

International Research Project

2010 Oct.-Dec.

International Training Program (For training young researchers on plasma nanotechnology materials and device processing, conducted by Japan Society for the Promotion of Science) at Prof. Keudell's group in Ruhr University Bochum, Germany.p

2012 June.-July.

International Training Program (For training young researchers on plasma nanotechnology materials and device processing, conducted by Japan Society for the Promotion of Science) at Prof. Chang's group in University of California, Los Angeles, United States of America.

Journal publications (or Peer reviewed journals)

Title	Journal	Authors Related Chapter
1. Behaviors of Absolute Densities of N, H, and NH_3 at Remote Region of High-Density Radical Source Employing N_2/H_2 Mixture Plasmas	Jpn. J. Appl. Phys. **50**, 01AE03 (2011)	Shang Chen, Hiroki Kondo, Kenji Ishikawa, Keigo Takeda, Makoto Sekine, Hiroyuki Kano, Shoji Den, and Masaru Hori (Chapter 3)
2. Achieving high-growth-rate in GaN homoepitaxy using high-density nitrogen radical source	Phys. Status Solidi C **8**, 2089 (2011)	Yohjiro Kawai, Shang Chen, Yoshio Honda, Masahito Yamaguchi, Hiroshi Amano, Hiroki Kondo, Mineo Hiramatsu, Hiroyuki Kano, Koji Yamakawa, Shoji Den, and Masaru Hori (Chapter 4)
3. Photoluminescence recovery by in-situ exposure of plasma-damaged n-GaN to atomic hydrogen at room temperature	AIP Advances **2**, 022149 (2012)	Shang Chen, Yi Lu, Ryousuke Kometani, Kenji Ishikawa, Hiroki Kondo, Yutaka Tokuda, Makoto Sekine, and Masaru Hori (Chapter 5)
4. As-grown deep-level defects in n-GaN grown by metal–organic chemical vapor deposition on freestanding GaN	(Submitted)	Shang Chen, Unhi Honda, Tatsunari Shibata, Toshiya Matumura, Yutaka Tokuda, Kenji Ishikawa, Masaru Hori, Hiroyuki Ueda, Tsutomu Uesugi, and Tetsu Kachi (Appendix)
5. Low Mosaicity and High Growth-Rate of InGaN films with Supply of High-Density Nitrogen Atoms in Molecular Beam Epitaxy	(Submitted)	Shang Chen, Yohjiro Kawai, Hiroki Kondo, Kenji Ishikawa, Keigo Takeda, Hiroyuki Kano, Makoto Sekine, Hiroshi Amano, and Masaru Hori (Chapter 3, Chapter 4)

6. Individual roles for atoms and ions during hydrogen plasma passivation of surface-defects on GaN created by plasma etching	(Submitted)	Shang Chen, Kenji Ishikawa, Yi Lu, Ryosuke Kometani, Hiroki Kondo, Yutaka Tokuda, Takashi Egawa, Hiroshi Amano, Makoto Sekine, and Masaru Hori (Chapter 5)

International conferences

Title	Conference	Authors
1. Development of high density nitrogen radical source and behaviors of atomic radicals	1st International Symposium on Advanced Plasma Science and its Applications (ISPlasma 2009), Mo-3 (p.134), Nagoya University, Nagoya, Japan, Mar. 8-11, 2009	S. Chen, H. Kano, S. Den, S. Takashima, K. Takeda, and M. Hori
2. Development of high density radical source and the behaviors of radicals in N_2-H_2 mixture plasma (Oral)	AVS 56th International Symposium and Exhibition, PS1-WeM11, p.112, San Jose McEnery Convention Center, Nov. 8-13, San Jose, CA, 2009	S. Chen, H. Kano, S. Den, K. Takeda, S. Takashima, M. Sekine, and M. Hori
3. Development of radical source and its application to GaN growth for LED (Oral)	The 10th International Workshop of Advanced Plasma Processing and Diagnostics Joint Workshop, Nagasaki Univ., Nagasaki, Japan, Jan. 8-10, 2010	S. Chen, H. Kondo, M. Sekine, M. Hori, and H. Kano
4. Radical kinetics in N_2-H_2 plasma generated by novel high density radical source (Oral)	2nd International Symposium on Advance Plasma Science and its Application for Nitrides and Nanomaterials (ISPlasma 2010), 9a-B03OB, Meijo University, Nagoya Japan, Mar. 7-10, 2010	S. Chen, H. Kano, S. Den, K. Takeda, K. Ishikawa, H. Kondo, M.sekine, and M. Hori
5. Deep-level defect passivation by high density hydrogen radical exposure on ion irradiated Si	2nd International Symposium on Advance Plasma Science and its Application for Nitrides and Nanomaterials (ISPlasma 2010), PA031A, Meijo University, Nagoya Japan, Mar. 7-10, 2010	S. Chen, Y. Nagoe, M. Nakai, K. Ishikawa, H. Kondo, H. Kano, K.Takeda, T. Tokuda, M. Sekine, and M. Hori
6. Analysis of gallium nitride (GaN) surface interacted with chlorine etching plasma beams (Oral)	63rd Annual Gaseous Electronics Conference and 7th International Conference on Reactive Plasmas, Paris, France, October 4-8, 2010	S. Chen, R. Kometani, K. Ishikawa, H. Kondo, K. Takeda, H. Kano, Y. Tokuda, M. Sekine, and M. Hori

7. Deep level defect in GaN after plasma beam etching	3rd International Symposium on Advance Plasma Science and its Application for Nitrides and Nanomaterials (ISPlasma 2011), P3-003A, Nagoya Institute of Technology, Nagoya, Japan, Mar. 6-9, 2011	S. Chen, R. Kometani, Y. Lu, K. Ishikawa, H. Kondo, K. Takeda, H. Kano, Y. Tokuda, M. Sekine, and M. Hori
8. Passivation of plasma damaged GaN with hydrogen radical anneal	The 4th International Conference on PLAsma-Nano Technology & Science (IC-PLANTS 2011), P-51, Takayama Public Cultural Hall, Gifu, Japan, Mar. 10-12, 2011	S. Chen, Y. Lu, R. Kometani, K. Takeda, K. Ishikawa, H. Kondo, H. Kano, Y. Tokuda, M. Sekine, Y. Setsuhara, T. Egawa, H. Amano, and M. Hori
9. Recovery of plasma-damaged GaN by atomic nitrogen and hydrogen (Oral)	The 13th international workshop on Advanced Plasma Processing and Diagnostics Daejeon Convention Center, p-25, Deajeon, Korea July 21~22 2011	S. Chen, Y. Lu, R. Kometani, K. Ishikawa, H. Kondo, K. Takeda, H. Kano, M. Sekine, and M. Hori
10. Room temperature radical annealing of plasma damaged gallium nitride (Oral)	AVS 58th International Symposium & Exhibition, Oct 30～Nov 4, 2011, Nashville Convention Center, Nashville, Tennessee, USA, PS-ThM11.	S.Chen, Y. Lu, R. Kometani, K. Ishikawa, H. Kondo, H. Kano, H. Amano, K. Takeda, Y. Tokuda, T. Egawa, M. Sekine, and M. Hori
11. The role of hydrogen radical on plasma damaged gallium nitride (Oral)	4th International Symposium on Advance Plasma Science and its Application for Nitrides and Nanomaterials (ISPlasma 2012), Chubu University, Aichi, Japan, Mar. 4-8, 2012	S. Chen, Y. Lu, R. Kometani, K. Ishikawa, M. Sekine, and M. Hori
12. Photoluminescence recovery of plasma damaged GaN by hydrogen radical annealing	The 5th International Conference on PLAsma-Nano Technology & Science (IC-PLANTS 2012), Inuyama International Sightseeing Center, Aichi, Japan, Mar. 9-10, 2012	S. Chen, Y. Lu, R. Kometani, K. Ishikawa, M. Sekine, and M. Hori

Dominant conferences

Title	Conference	Authors
1. 高密度ラジカルソースにおける窒素ラジカルの挙動（口頭発表）	2008 年秋季 第 69 回応用物理学会学術講演会、2p-ZC-9、中部大学、愛知県、2008 年 9 月 2-5 日	陳尚、加納浩之、田昭治、高島成剛、竹田圭吾、堀勝
2. 高密度ラジカルソースにおける窒素および水素ラジカルの挙動（口頭発表）	2009 年春季 第 56 回応用物理学関係連合講演会、1p-T-8、筑波大学、茨城県、2009 年 3 月 30 日-4 月 2 日	陳尚、加納浩之、田昭治、高島成剛、竹田圭吾、堀勝
3. 高密度水素ラジカル注入によるn型シリコン中の深い準位欠陥の不活性化（口頭発表）	2009 年秋季 第 70 回応用物理学関係連合講演会、10p-TG-7、 富山大学、富山県、2009 年 9 月 8-11 日	陳尚、永江陽一、竹内和歌奈、中井雅文、加納浩之、竹田圭吾、徳田豊、関根誠、堀勝
4. 高密度ラジカルソースの開発と窒素ラジカルの挙動（ポスター発表）	プラズマ科学シンポジウム 2009/第 26 回プラズマプロセシング研究会、P2-55、名古屋大学豊田講堂・シンポジオン、名古屋、2009 年 2 月 2 日-4 日	陳尚、加納浩之、竹田圭吾、田昭治、高島成剛、堀勝
5. イオン照射誘起深い準位欠陥の水素ラジカルによる不活性化（口頭発表）	2010 年春季 第 57 回応用物理学関係連合講演会、17p-D-7、東海大学、神奈川県、2010 年 3 月 17 日-3 月 20 日	陳尚、永江陽一、石川健治、中井雅文、加納浩之、竹田圭吾、近藤博基、徳田豊、関根誠、堀勝
6. プラズマによる GaN エッチング損傷と反応機構の解析（口頭発表）	2010 年秋季 第 71 回応用物理学会学術講演会、17a-ZA-3、長崎大学、長崎県、2010 年 9 月 14 日-17 日	陳尚、米谷亮祐、竹田圭吾、石川健治、近藤博基、加納浩之、徳田豊、関根誠、節原裕一、江川孝志、天野浩、堀勝

7. 水素ラジカルによる GaN 中プラズマ誘導欠陥の不活性化（ポスター発表）	応用物理学会プラズマエレクトロニクス分科会 20 周年記念特別シンポジウム、名古屋大学、2011 年 10 月 22 日、P-42	陳尚、盧翌、米谷亮祐、竹田圭吾、石川健治、近藤博基、関根誠、堀勝
8. 真空一貫プロセスによる GaN プラズマビームエッチング及び水素ラジカルダメージ層除去とその表界面反応機構の解明（口頭発表）	2011 年春季 第 58 回応用物理学関係連合講演会、神奈川工科大学、神奈川県、2011 年 3 月 24 日-27 日	陳尚、盧翌、米谷亮祐、江川孝志、石川健治、近藤博基、加納浩之、徳田豊、関根誠、節原裕一、竹田圭吾、天野浩、堀勝
9. GaN におけるプラズマダメージの水素ラジカル修復（口頭発表）	2011 年秋季 第 72 回応用物理学会学術講演会、山形大学、小白川キャンパス、2011 年 8 月 29 日-9 月 2 日	陳尚、盧翌、米谷亮祐、竹田圭吾、石川健治、近藤博基、加納浩之、徳田豊、関根誠、江川孝志、天野浩、堀勝
10. GaN におけるプラズマダメージの水素ラジカル修復 (2)（口頭発表）	2012 年春季第 59 回応用物理学関係連合講演会、早稲田大学、 東京都、2012 年 3 月 15 日-18 日	陳尚、盧翌、米谷亮祐、石川健治、竹田圭吾、近藤博基、加納浩之、徳田豊、関根誠、江川孝志、天野浩、堀勝